UNIVERSITÀ DEGLI STUDI DI PADOVA

Dipartimento di ingegneria industriale

Corso di Laurea Magistrale in Ingegneria Aerospaziale

Tesi di Laurea

Ice accretion simulation over 2D airfoils by means of a methodology embedded in a CFD solver

Stefano Fornasier

Relatore:
Prof. Ernesto Benini
Correlatore:
Ing. Elisabetta Borghi

Anno Accademico 2015 - 2016

Abstract

The analytical investigation of ice accretion is a complementary part of flight and wind tunnel tests needed for certification and ice protection system design. Because the computational fluid dynamics is usually limited to the flow solutions over iced surfaces the actual icing simulations generally relies on potential flow solution.

In this thesis the ice accretion over bi dimensional aerodynamic surfaces is performed for a wide variety of conditions. A dedicated tool, IceMAP 2D, has been developed to integrate the ice accretion simulation process in the CFD software Fluent, used to solve the compressible Navier-Stokes equations.

The tool developed has been validated with experimental data and icing software in demanding conditions; also the effects of varying different parameters, like velocity or temperature, on the ice shape has been investigated. Finally the aerodynamic characteristics of iced airfoil have been studied and compared with experimental data.

Contents

List of Figures

Nomenclature

α	Angle	$[rad]$
β	Collection efficiency	
δs	Infinitesimal surface length	$[m]$
δy	Forward projection of surface length	$[m]$
$\dot{m}$	Mass flow rate	$[\frac{kg}{s}]$
γ	Ratio of specific heat	
μ	Dynamic viscosity	$[Pa \cdot s]$
ρ	Density	$[\frac{kg}{m^3}]$
τ	Droplet relaxation time	
Θ	Angle	$[rad]$
A	Area	$[m^2]$
b	Thickness	$[m]$
C_D	Coefficient of drag	
$chord$	Chord length	$[m]$
cp	Specific heat	$[\frac{J}{kg \cdot K}]$
d	Diameter	$[\mu \cdot m]$
D_v	Diffusivity of water vapour in air	$[\frac{m^2}{s}]$
ds	Surface area	$[m^2]$
E	Total collection efficiency	
F	Force	$[N]$
Fr	Frossling number	

g	Gravity acceleration	$[\frac{m}{s^2}]$
H	Forward projection of the airfoil height	$[m]$
Hc	Heat transfer coefficient	$[\frac{W}{m^2 \cdot K}]$
Hg	Mass transfer coefficient	$[\frac{kg \cdot K}{J}]$
k	Thermal conductivity	$[\frac{W}{m \cdot K}]$
ks	Equivalent sand grain roughness	$[m]$
L	Latent heat	$[\frac{J}{kg}]$
LWC	Liquid Water Content	$[\frac{g}{m^3}]$
M	Mach number	
m	Mass	$[kg]$
MVD	Mean Volumetric diameter	$[\mu m]$
n	Freezing fraction	
Nu	Nusselt number	
p	Pressure	$[Pa]$
p_{wi}	Vapour pressure of water over ice	$[Pa]$
p_{ww}	Vapour pressure of water at the surface	$[Pa]$
p_w	Vapour pressure of water in the atmosphere	$[Pa]$
Pr	Prandtl number	
q	Power	$[W]$
R	Gas constant	
Re	Reynolds number	
S	Effective temperature (Sutherland constant)	$[K]$
Sc	Schmidt number	
T	Temperature	$[K]$
t	Time	$[s]$

V	Velocity	$[\frac{m}{s}]$
x	Position	$[m]$
y	Surface length, position	$[m]$
CFD	Computational Fluid Dynamics	
CMI	Continuous Maximum Icing	
DERA	Defence Evaluation and Research Agency	
FAR	Federal Aviation Regulations	
FIPS	Full Ice Protection System	
IMI	Intermittent Maximum Icing	
JAR	Joint Aviation Requirements	
LEWICE	LEWis ICE accretion program	
ONERA	Office National d'Etudes et de Recherches Aérospatiales	
RANS	Reynolds Averaged Navier Stokes equations	
SLD	Super-cooled Large Droplets	
UDF	User Defined Functions	

Subscripts

$_{(i)}$	Control volume
$_{(i+1)}$	Next control volume
$_{(i-1)}$	Preceding control volume
$_{(t)}$	Current time step
$_{(t+1)}$	Next time step
$_{0}$	Initial condition
$_{\infty}$	Freestream condition
$_{impact}$	Impact condition
$_{a}$	Aerodynamic
$_{c}$	Convection
$_{d}$	Droplet
$_{edge}$	Edge of the boundary layer

$_e$	Evaporation
$_f$	Freezing
$_{ice}$	Ice
$_{imp}$	Impinging
$_i$	Local
$_k$	Kinetic
$_{max}$	Maximum value
$_{min}$	Minimum value
$_{node}$	Node value
$_p$	Particle
$_{rb\,in}$	Runback in
$_{rb\,out}$	Runback out
$_{ref}$	Reference condition
$_{surf}$	Surface
$_s$	Sublimation
$_v$	Vaporization, vapour
$_w$	Water

Chapter 1

Introduction

Ice accretion on aerodynamic surfaces, rotors and other components poses a significant issue to the safety of flight; indeed, large areas are exposed to icing, and the risks associated vary depending on where the ice forms. Issues are mainly due to the altered characteristics of wings and other aerodynamic surfaces, and the increase in weight due to the mass of ice.

The performance of wings suffers degradation, with increased drag combined with a decrease in lift, and their combined effect may result in premature stall; rotor blades also suffer from the weight increase, which may cause abnormal vibrations. Icing on air intakes can severely disturb the incoming air flow and cause malfunctioning or shutdowns; air intakes are also subject to ice ingestion, with similar consequences. Accretion of ice on the fuselage increases the overall drag, but also impacts the functionality of the instrumentation, e.g. pitot tubes, and pilots visibility, which may be impeded by icing growing on windshields. Additionally, control surfaces may get stuck or experience limitations in their movements.

Icing occurs in flight when liquid water droplets present in the air impact on rotorcraft or aircraft and freeze, remaining attached to the surface. This is possible during encounters with clouds and fog, which are composed by small particles of liquid water, snow flakes or ice crystals; indeed, it has been observed that liquid water can be found in normal environmental conditions at temperature up to -40 $°C$. Unlike water droplets, snow and ice crystal do not pose a threat for icing, because after impacting they do not remain attached to the surface but return in the air.

Depending on ambient conditions, the ice accretion can be divided in two main typologies, rime and glaze. Rime ice grows when water droplets freeze completely on impact, and assumes a white opaque color (because of the presence of air in the frozen water) and is relatively streamlined. Surface roughness is increased compared with the clean surface and aerodynamic properties are reduced. Rime ice forms at a combination of low temperature, low speed and low liquid water content, and is visible on the left of figure 1.1.

At a combination of high temperature, high speed and liquid water content water does not freeze completely on impact and flows over the body; the water film flowing on the surface may eventually freeze further aft and result in localized ice accretion, producing shapes similar to horns. This type of ice accretion is termed glaze ice (figure 1.1, right), and appears translucent and has a significant surface roughness.

Figure 1.1: Rime ice accretion, left, and glaze ice, right.

At intermediate conditions ice presents characteristic of both type of ice, with a glaze like accretion limited in area near the leading edge of the airfoil.

To cope with the risks associated with icing two categories of systems are commonly used, which aim at reducing, in the case of de-icing, or preventing, for anti-icing, the accretion of ice. In the case of de-icing a limited amount of ice is allowed to grow before being removed, using for example pneumatic systems to break the ice or electrical heater. Anti-icing is necessary for surface that must be kept completely clean from ice, like windshields and pitot tubes, and is often obtained using electrical heater.

Figure 1.2: Ice accumulation on aircraft wing.

Because of the breadth of issues described, icing has been long recognized as a severe hazard to safe flight, as has been highlighted by many accidents. A great effort has been placed on identifying the underlying causes of icing, in order to better determine the ice accretion characteristics and the effects on aircraft and helicopters, as well as to optimize the functionality of ice protection systems. As a result, many tools have been developed to simulate ice accretion, and this has allowed not to rely solely on flight and wind tunnel testing in the design and certification process of aircraft and helicopters.

The aim of this thesis is to develop a code to simulate ice accretion on bidimensional bodies, including helicopter blade airfoils. The ice accretion code is embedded in a CFD software, Fluent®[1], in order to take full advantage of the flow field solution computed solving Navier-Stokes equations. Indeed, the variables required to perform the ice accretion simulation have been derived from the flow field solution and the particle tracking model. Also a routine to update the geometry and adapt the mesh based on ice accretion has been developed and integrated within Fluent.

In the following sections a more thorough examination of the effects of icing in helicopter operations is presented, in order to provide additional insight on the conditions that lead to ice formation and the effect of icing peculiar to helicopters. A review of previous work and the implementation in icing codes follows.

In the second chapter the mathematical model, used to simulate ice accretion, is described; this includes the description of the parameters that governs ice accretion, the importance of the aerodynamic solution, the determination of particle trajectories and the thermodynamic solution. The third chapter describes the code developed, IceMAP 2D and how the model previously described has been implemented. The following chapters presents the results obtained, in particular the simulated ice shapes, which are compared with experimental shapes and other icing software, and the aerodynamic properties of iced airfoil. Conclusions and possible improvements to the model and the tool are then discussed.

1.1 Icing in helicopter operations

Rotorcraft are more and more required to fly in all weather conditions, in order to meet customer needs. A specific type certificate is required for a rotorcraft to fly in icing conditions, otherwise it is forced on ground whenever ice conditions are forecasted. The accretion of ice on helicopter surfaces can compromise the success of mission, affecting the efficiency or worse the safety of the flight. The mass of ice growing on helicopter fuselage causes a weight and drag increase, which translates in greater fuel consumption and consequently reduced maximum range. The ice mass can also introduce additional loads and vibrations, causing structural problems.

Helicopter performances are restricted mainly by the accretion of ice on the leading edge of the main rotor blades, which modify the lift, drag and moment characteristics of the airfoil. Because of the altered aerodynamic characteristics, an increase in power may be required to maintain the same flight condition, and may also be accompanied by vibrations and different handling characteristics, that is also the result of the weight of

[1]ANSYS, ANSYS Workbench, AUTODYN, CFX, FLUENT and any and all ANSYS, Inc. brand, product, service and feature names, logos and slogans are registered trademarks or trademarks of ANSYS, Inc. or its subsidiaries in the United States or other countries. All other brand, product, service and feature names or trademarks are the property of their respective owners.

Figure 1.3: Icing on an external probe.

the ice formation on the blades. Consequently, the loads on the airframe and transmission increase, and require monitoring, at least in the certification process, to ensure that they remain acceptable.

Because of the high loads (aerodynamics and dynamic) experienced during the blades motion, ice may break and its pieces be projected in the air; after shedding the surface generally return clean from ice, but it can also result in asymmetric distribution of the ice mass, which further increase the level of vibrations. Centrifugal and dynamic forces, aerodynamic pressure distribution, blade deformations and vibrations, ice structural strength and local non uniformities and cohesion between ice and blade surface: all these factors contribute to determine the ice shedding process, and make the modelling of the phenomenon extremely difficult. Additionally, ice shedding from blades may impact the fuselage or other system and cause damage to the airframe.

Beside the overall increase in drag, fuselage icing has additional consequence on helicopter operations. Pilot's visibility may be impeded by icing on windshiels, and icing on external sensors and instrumentation can cause impaired data acquisition. Icing on engine intakes and nacelles can result in engine failure, because of ice ingestion or blockage of the airflow.

The ability to fly in known icing conditions could dramatically increase the envelope of rotorcraft, but requires accurate knowledge of where ice will form, so that adequate ice protection systems can be fitted. Because of the large costs involved in the design, build and certification process, only some helicopter are certified for flight onto known icing conditions, having a Full Ice Protection System installed. Ice protection systems provide the pilots with information regarding the icing conditions, with reliable values of liquid water content, temperature, and visual clues on particle size, and protect the areas of the helicopter more exposed to icing. Ice protection system is activated when external temperature is near or below freezing and liquid water is detected in the air.

De icing or anti icing is employed depending on the surface to be protected. Windshields and instrumentation probes (e.g. pitot tubes) must be kept clear from ice under all conditions, and are continuously protected using electrical heaters. On the main rotor blades a limited ice accretion is acceptable, and different systems can be employed.

Figure 1.4: Top left: Ice detector, used to detect the presence of liquid water in the air. Bottom right: SLD marker, provides visual information on particle size; if ice grows in the red or yellow area particle size is above certification limits, and flight is not permitted.

Electrical heaters, located underneath the leading edge of the blades, can be cyclically turned on to prevent excessive ice accretion, or parasite currents may be used to create an electromagnetic field able to inflate boots that break the ice accretion. Because of the small dimension of the tail rotor the energy requirement to maintain it clear from ice is limited, and an anti icing system can be fitted, generally using electrical heaters. Air intakes are protected by heating the areas where ice may grow, either using hot air bled from the engines or electrical heater, or by using passive systems, like bypass for air. Stabilizer may in some case retain sufficient control when iced and may not require specific protection, otherwise bleed air, pneumatic boots or electrical heating systems may be fitted.

Certification requirements are fixed in the FAR/JAR 29 appendix C for continuous maximum icing and intermittent maximum icing. Droplet size considered is between 15 and 50 μm, which is the range most frequently encountered, but in some cases larger particles may be encountered (up to 500 μm); these droplets are called super-cooled large droplets. In this case flight is forbidden, because ice quickly grows on large areas of helicopter.

To meet certification requirements the capability of the helicopter to safely operate in the conditions prescribed must be proved. In the certification process flight and icing wind tunnel test activities and analytical studies are used to assess the effects of ice on the helicopter surfaces, the efficiency of the ice protection system and the performance degradation. Relying solely on icing tunnel and flight can be time consuming and expensive; moreover, it is not granted that all the icing conditions required can be find in nature during icing trials. As a consequence, the flight test activities may take several years to complete. Reliable icing tools can be greatly helpful in minimizing and focusing icing tunnel and flight tests, by determining the most critical icing conditions that need to be tested, thus cutting time and costs involved in the certification process. Additionally,

Figure 1.5: AW139 during icing trials; a CH-47 sprays liquid water which reproduce icing conditions, while the tested helicopter follows.

icing tools can provide helpful information in the design and optimization of ice protection systems, by minimizing their energy and weight requirement.

1.2 Literature review

Efforts to understand the effects of in-flight icing began in the early '40s, mainly with flight testing and experiments, which eventually lead to the development of ice protection system. Analytical studies began shortly after, in order to optimize the usage of anti icing systems. In 1946 Langmuir and Blodgett[5] started studying the trajectory of droplets, developing a set of equations to predict particle motion.

In 1953 Messinger[7] developed an analytical model to predict the formation of ice on an unheated surface: an energy and a mass balance are solved on the surface of the body in order to determine the growth of ice. A number of improvements to the Messinger model have been proposed, but it remains the foundation of most of the ice accretion prediction codes in use.

Although early efforts laid the analytical foundation for subsequent researches and simulations, they were hampered by the lack of computing power; therefore, until the advent of digital computer studies were limited to simple geometries for which an analytical solution could be derived.

Computational fluid dynamics codes have been used more recently to predict the collection efficiency on bidimensional and three-dimensional bodies as well as to determine the aerodynamic characteristic of iced airfoils.

1.3 Icing codes

Over the years various icing software have been developed in order to provide tools to analytically determine the extent of icing. LEWICE[18], developed by the Icing Branch at NASA Glenn Research Center, ONERA[19] and TRAJICE[4], developed by DERA in the United Kingdom, have been widely used.

The codes are structured in a similar fashion, comprising three main modules with only minor differences:

1. A potential flow panel method to calculate the flow field around the airfoil.

2. A bi dimensional water droplet trajectories module.

3. A thermodynamic module.

In LEWICE[18] a Hess-Smith 2D panel flow method calculates the flow field around the generic airfoil, then the trajectories of particles are computed; finally a thermodynamic balance, based on Messinger work, is solved on the surface, starting from the stagnation point. The heat transfer coefficient is computed using an integral boundary layer analysis. Ice is then allowed to grow orthogonally with respect to the original surface. LEWICE has a time stepping capability used to grow ice. Therefore ice grows on the surface for a given time, and then the geometry is modified by the ice accretion. The flow field is computed again on the modified geometry, and the process is repeated until the full icing exposure has been reached.

ONERA[19] solves the flow field using a finite element method; it takes into account compressibility effect, but not viscosity. Further, it can not determine any boundary layer separation. Particle trajectories are computed considering only drag forces acting on droplets, resulting from a difference in veloctity between a given particle and the flow field around it. The heat transfer coefficient is computed using a relation developed by Makkonen[6]. The solution of the thermodynamic balance, based on the Messinger analysis, starts at the stagnation point, then the ice thickness at each surface location is computed.

In TRAJICE2[19] the flow field is solved using a two dimensional code developed by DERA, and it is coupled with a bi dimensional trajectory computation module to determine the mass of water impacting on the surface of the airfoil. The thermodynamic balance is based on the Messinger approach also used in LEWICE, but considering the effect of compressibility in the energy terms. Ice growth is assumed to be orthogonal to the surface in case of glaze ice, while is parallel to the freestream velocity in case of rime accretion. A time stepping capability is also available; if used, the heat transfer coefficient on the airfoil is computed using an integral boundary layer approach, similar to LEWICE, while for a single time step the heat transfer coefficient is computed using an empirical correlation derived for cylinders.

Chapter 2

Physics of ice accretion

This chapter describes the mathematical model used for the ice accretion simulation. In section 2.1 the most significant parameters are discussed, showing their influence on the ice accretion. In the following sections the equations governing the problem are described; first the effects of the flow field on the ice accretion are highlighted, then the model used to compute the trajectory of particles is derived. Finally the equations governing the energy and mass balance are presented. The thermodynamic balance is the core of the problem, since thermal exchanges determine the amount of water that freezes on the body. This model has been developed starting from Messinger[7], and subsequently has been modified by Myers[9].

2.1 Icing parameters

The amount of ice that accrues on a surface basically depends on two aspects: the rate of water impingement and the amount of water that freezes after the impact.

The rate of impingement is determined by the droplet trajectories when they approach the body, and thus it is influenced by the body size and shape, droplet dimension, airspeed and the content of water in the air (liquid water content).

As said, the thermodynamic balance is the core of the problem, because it determines the amount and the rate at which water freezes. Water freezes if its latent heat of fusion can be dissipated, generally through convection and evaporation, while other energy terms have the opposite effect. The parameters that have the largest influence on the thermodynamic balance are the outside air temperature, the speed of the object and its surface roughness.

2.1.1 Temperature

Outside air temperature is by far the most critical parameter in ice accretion. While temperature is relatively easy to measure, it is the surface temperature that dictates whether icing is possible and at what rate ice will grow.

In the ice accretion process the outside temperature controls the convective cooling of incoming droplets and therefore the dissipation of their latent heat of fusion. At high temperature (close to freezing) the convective cooling is limited, and the rate of ice accretion is small. Generally, temperature close to freezing results in glaze icing, because

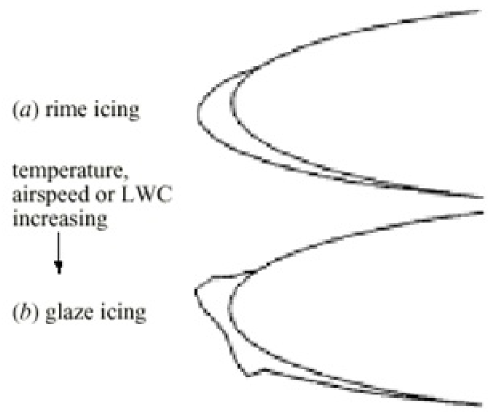

Figure 2.1: Influence of ambient conditions on ice shapes.

water can not fully dissipate its latent heat of fusion, so it does not freeze and flows over the surface forming a liquid film. Low temperature results in rime ice, because convection and evaporation can dissipate fast enough the latent heat of droplets. Icing may also occur if total temperature is above 0 $°C$, because evaporation of droplets will decrease the surface temperature and under appropriate conditions lead to ice accretion.

A secondary effect of air temperature is related to water loading: as temperature is reduced the probability of encountering large amount of droplet, that is high liquid water content, is reduced.

2.1.2 Liquid water content

Liquid water content represents the amount of liquid water encountered in the cloud.

Liquid water content affects both the type of ice forming and the rate of accretion. In case of high water content also the latent heat to be removed is high, and therefore the tendency for glaze ice to grow. Lowering the ambient temperature, which also decrease the liquid water content, will increase the heat that can be dissipated through evaporation, and all droplets may freeze on impact.

If the liquid water content is doubled in a rime accretion also the rate of ice growth on the surface can be expected to double, if rime conditions still exist at the higher LWC. For glaze icing increasing the liquid water content can still result in increasing mass of ice.

Liquid water content is generally between 0.1 and 0.5 g/m^3, but in some cases may also reach extremely high values, up to 2 g/m^3 at high temperature.

2.1.3 Droplet size

Large droplets are less influenced by the airflow near the airfoil, because droplet mass is proportional to the cube of the diameter while aerodynamic forces are proportional to the square of the diameter. Larger droplets thus follows a straighter trajectory and are more likely to impact on airfoils and other surfaces, while smaller droplets follows more closely the air streamlines and may not strike on exposed surfaces. The size of the airfoil also influence whether droplets will impact, as larger object have a larger influence on the nearby airflow; therefore, for a given droplet size a large airfoil or fuselage is less exposed to icing, while small airfoil like helicopter blade collects more water.

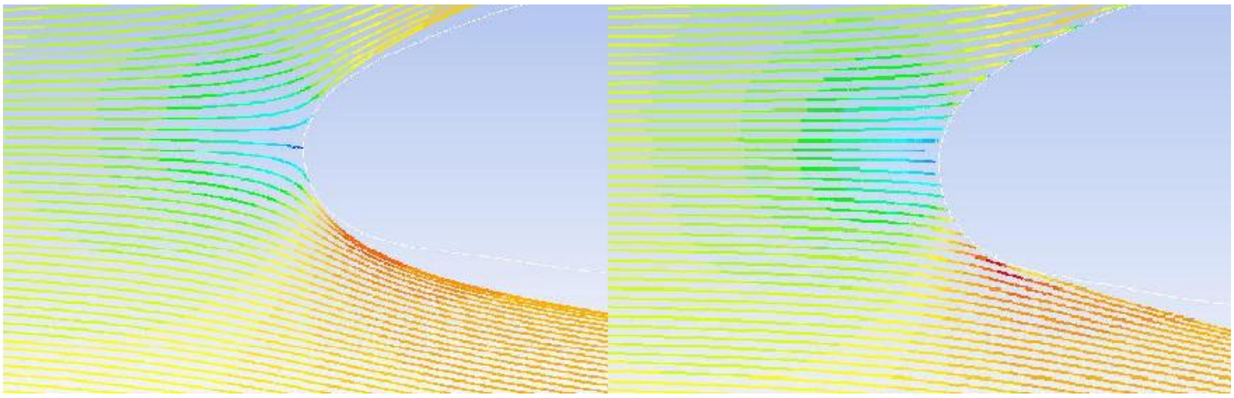

Figure 2.2: Differences in particle trajectories, diameter 10 μm (left) and 40 μm (right).

In a cloud the diameter of particles is variable; a single value, the median volumetric (volume) diameter, is used to characterise an icing condition. The median volumetric diameter is defined as the droplet diameter for which half the total liquid water content is contained in droplets larger than the median and half in droplets smaller than the median. Droplets larger than the median are present but relatively few in number, while smaller droplets, even if present in great quantity, only have a small mass associated.

Typical values for median volume diameter for icing conditions are between 15 μm and 50 μm, but in some rare icing conditions MVD can reach 500 μm, referred to as Super-cooled Large Droplets.

2.1.4 Airspeed

The main influence of the airspeed on icing resides in the mass of water collected by the body: at increasing airspeed the amount of water collected by the body in a given time also rises. The mass of impinging water is indeed the product of collection efficiency, liquid water content and airspeed, and consequently also the rate of ice accretion may increase with airspeed. Aerodynamic heating is also augmented by the raise in airspeed, and will partially compensate for the increased rate of icing.

2.2 Aerodynamic solution

The ice accretion process is influenced by the flow field around the airfoil in many different ways. The forces acting on the liquid droplets are mainly caused by the velocity difference between the particles and the local flow, thus the trajectory followed by each particle is dictated by the flow field and the particle size. As a result, the distribution of impinging water on the surface is dependant on the flow solution.

Moreover the thermodynamic balance, that governs the accretion process, strongly depends on the local flow field. Aerodynamic heating of the airfoil and convective heat transfer, for example, depend on the local air velocity and temperature. This is also true for the convective heat transfer coefficient, which is influenced by the boundary layer near the surface and it is used to compute many terms in the thermodynamic balance.

For these reasons, the accuracy of flow field solution can significantly alter the final ice shape; many software are commercially available, which can use simple panel method or a solution of Navier-Stokes equations. The usage of Navier-Stokes equations is preferred, because they do not suffer from the limitations intrinsic in the panel method solution. Therefore, a greater range of conditions can be simulated accurately, including high Mach number, flow separation and viscosity effects.

2.3 Droplets trajectories computation

The particle trajectories determine where and at what rate the water impinges the body. Two different approaches are used to compute the particle trajectories; the first approach relies on the Eulerian formulation, in which the liquid volume fraction is modelled as a continuum. Therefore, no individual particle is tracked, and collection efficiency is computed directly from flow solution. This approach has been successfully used for complex three-dimensional problems. The second, and the most used for icing simulation, is the Lagrangian formulation, in which a large number of particles are tracked as they flow through the domain. The particles are released from a location upstream of the airfoil, and tracked until they impact the body. Also in the tool developed in this thesis work the Lagrangian approach has been used. The water particle are assumed to be perfectly spherical, and may exchange momentum and energy with the surrounding air. The Lagrangian approach is simplified neglecting particle-particle interactions; this is acceptable, because water droplets occupy a low volume of air, and collision between droplets are unlikely. Additionally, the deformations of droplets is not included, nor is the possibility of breakup. Breakup is caused by the increase of the aerodynamic forces with respect to the water surface tension which is experienced in large droplets, like SLD. For the small droplet size (below 50 μm) considered this effect can be disregarded.

To compute the trajectory of each particle a force balance, derived from Newton's second law, is considered; here, the aerodynamic and gravitational forces are equated to the particle inertia, but other forces may be included.

$$\frac{d\vec{V}_p}{dt} = \frac{\vec{F}_a + \vec{F}_g + \vec{F}}{m_p} \tag{2.1}$$

Using the following expressions for the forces acting and particle mass and surface:

$$\vec{F}_a = \frac{1}{2}\rho C_D A_p \left(\vec{V} - \vec{V}_p\right)^2 \tag{2.2}$$

$$\vec{F}_g = m_p \vec{g} \left(1 - \frac{\rho}{\rho_p}\right) \tag{2.3}$$

$$m_p = \frac{4}{3}\rho_p \pi \frac{d_p^3}{8} \tag{2.4}$$

$$A_p = \frac{1}{4}\pi d_p^2 \tag{2.5}$$

Substituting in equation (2.1), considering only the effect of gravitational and aerodynamic forces and simplifying:

$$\frac{d\vec{V}_p}{dt} = \frac{18}{24}\frac{\rho d_p^2 C_D \left(\vec{V} - \vec{V}_p\right)^2}{\rho_p d_p^3} + \vec{g}\left(1 - \frac{\rho}{\rho_p}\right) \tag{2.6}$$

Using the Reynolds droplet number and the particle relaxation time, defined as follow:

$$Re_p = \frac{\rho d_p |\vec{V}_p - \vec{V}|}{\mu} \tag{2.7}$$

$$\tau_r = \frac{\rho_p d_p^2}{18\mu}\frac{24}{C_D Re_p} \tag{2.8}$$

The force balance in equation (2.6) can be further simplified to yield equation (2.10).

$$\frac{d\vec{V}_p}{dt} = \frac{18}{24}\frac{Re_p \mu C_D \left(\vec{V} - \vec{V}_p\right)}{\rho_p d_p^2} + \vec{g}\left(1 - \frac{\rho}{\rho_p}\right) \tag{2.9}$$

$$\frac{d\vec{V}_p}{dt} = \frac{\vec{V} - \vec{V}_p}{\tau_r} + \vec{g}\left(1 - \frac{\rho}{\rho_p}\right) \tag{2.10}$$

The drag coefficient of particles, C_D, is computed considering the droplets spherical, and is given in equation (2.11).

$$C_D = a_1 + \frac{a_2}{Re_p} + \frac{a_3}{Re_p^2} \tag{2.11}$$

a_1, a_2, a_3, are constants derived by Morsi and Alexander[8] that apply over several ranges of Reynolds. These are:

$$a_1, a_2, a_3 = \begin{cases} 0, 24, 0 & 0 < Re < 0.1 \\ 3.690, 22.73, 0.0903 & 0.1 < Re < 1 \\ 1.222, 26.1667, -3.8889 & 1 < Re < 10 \\ 0.6167, 46.50, -116.67 & 10 < Re < 100 \\ 0.3644, 98.33, -2778 & 100 < Re < 1000 \\ 0.357, 148.62, -47500 & 1000 < Re < 5000 \\ 0.46, -490.56, 578700 & 5000 < Re < 10000 \\ 0.5191, -1662.5, 54167000 & Re \geq 10000 \end{cases} \tag{2.12}$$

In equation (2.1) $\vec{F}$ represents other forces that can be important under some circumstances, for example interactions with other particles forces in the case of large particles. For the range of particles considered these may be neglected. Additionally, also gravity force may be neglected, because the particle size is small enough that gravity has a minimal influence on their trajectory.

Finally, also heating and cooling is computed for droplets. This is obtained using a heat balance, and relates particle temperature and convective heat transfer at the particle surface.

$$m_p\, cp_p \frac{dT_p}{dt} = Hc\, A_p(T_\infty - T_p) \tag{2.13}$$

The particle heat transfer coefficient is evaluated using the correlation developed by Ranz and Marshall[13]:

$$Nu = \frac{hd_p}{k_\infty} = 2.0 + 0.6Re_d^{\frac{1}{2}}Pr^{\frac{1}{3}} \tag{2.14}$$

The trajectory equations (2.10) and the equations (2.13) describing heat transfer to/from the particle are solved by stepwise integration over discrete time steps. Equation (2.10) yields the particle velocity at each point along the trajectory, and the trajectory itself is then computed with equation (2.15).

$$\frac{d\vec{x}}{dt} = \vec{V}_p \tag{2.15}$$

2.3.1 Collection efficiency

Starting from the determination of particle trajectories also the positions of particles impacts on the airfoil can be computed, thus yielding the distribution of impinging water on the surface. This is referred to as collection efficiency, which represents the fraction of the freestream water flux that impacts at a given body location. The distribution usually has a peak near the stagnation point and approaches zero at some point aft on the upper and lower airfoil surfaces.

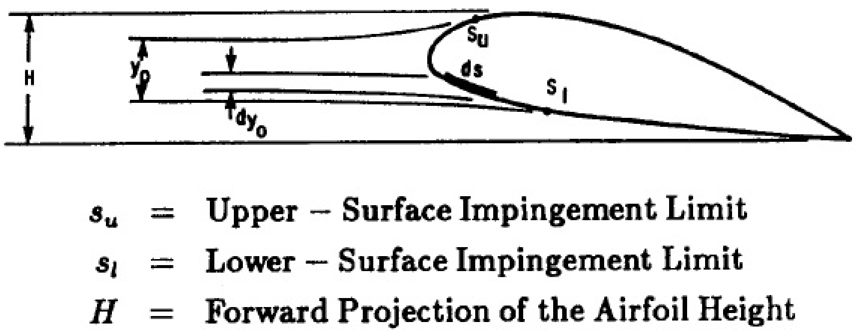

Figure 2.3: Definition of total and local collection efficiency.

The local collection efficiency is defined as the ratio between the surface a given mass of water passes through in the free stream and the surface it covers on the surface. Referring to figure 2.3 the local collection efficiency is therefore given by equation (2.16), where β is the local collection efficiency.

$$\beta = \frac{\delta y_0}{\delta s} \tag{2.16}$$

An additional parameter that can be computed is the total collection efficiency, which represents a measure of the total water collected by the body. Total collection efficiency is, using the same terminology as in figure2.3, given as:

$$E = \frac{y_0}{H} \tag{2.17}$$

2.4 Energy and mass balance

The amount of freezing water is computed solving a thermodynamic balance on the surface of the airfoil. For water to freeze the latent heat of fusion of the droplet must be dissipated, through a combination of convective cooling, evaporation and other energy terms that have to be computed. The modelling of icing requires the computation of a mass and a thermal balance for each control volume, figure 2.5, located on the surface of the body. Initially, the airfoil is divided in a number of segment (figure 2.4), and the lower boundary of the control volume is located on each segment. Therefore, the lower boundary is initially in contact with the clean surface, and then moves outward with the surface as ice accretes. The control volume is therefore always either on the clean surface or on the iced surface.

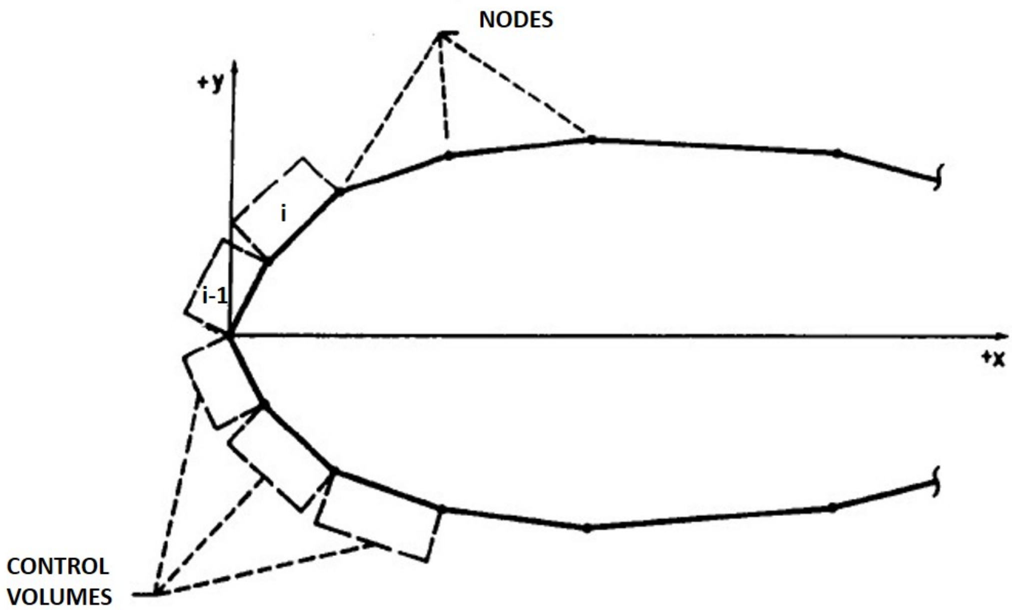

Figure 2.4: Identification of the control volumes over each segment defining the body.

From the solution of the thermodynamic balance the freezing fraction can be computed, which represent the fraction of liquid water that freezes at each location. If not all of the water freezes, it is assumed that the remaining water (runback water) flows along the surface of the body, and it is included in the thermal and mass balance of the successive control volume. The freezing fraction is then used to compute the rate of accretion and the iced geometry at a given time can be determined.

When writing the thermal and mass balance some assumptions have been made:

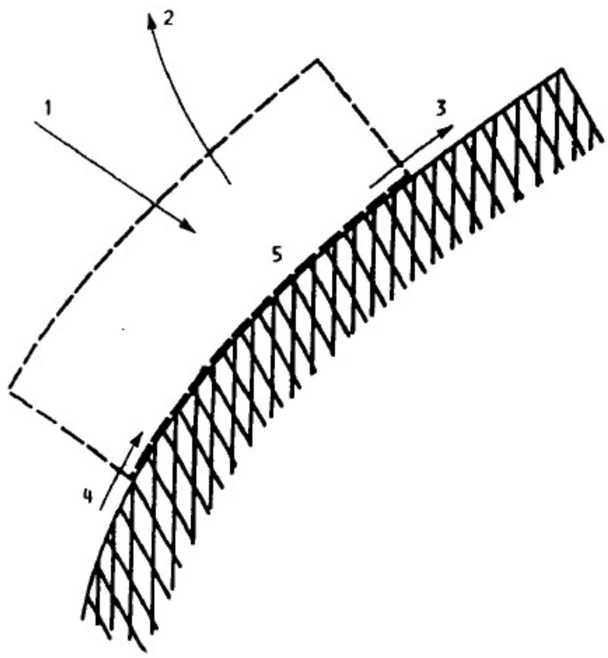

Figure 2.5: Mass balance for each control volume. 1: impinging water; 2: water leaving the airfoil through evaporation or sublimation; 3: runback water leaving the control volume; 4: runback water entering the control volume; 5: water leaving the control volume through icing.

- Unfrozen water is only allowed to run back, thus water may not remain on a control volume nor be shed.
- Run back is at the freezing temperature of water.
- Radiation is neglected, as it only has limited influence given the low temperatures involved.
- Conduction toward the airfoil is neglected. Heat conduction depends on material property and thickness, and can be accepted considering that it only has limited influence on the ace accretion.

Referring to figure 2.5, the water flux entering the control volume is the sum of impinging water and runback water; water can leave the control volume by evaporation/sublimation, runback and icing. The mass balance can be written for each control volume on the airfoil as:

$$\boldsymbol{\dot{m}_{imp\,(i)} + \dot{m}_{rb\,in\,(i)} = \dot{m}_{e\,(i)} + \dot{m}_{s\,(i)} + \dot{m}_{rb\,out\,(i)} + \dot{m}_{ice\,(i)}} \tag{2.18}$$

Where the mass fluxes terms considered are:

- impinging: sum of the mass flow rate of impinging water on the panel.

$$\dot{m}_{imp\,(i)} = \sum \dot{m}_p \tag{2.19}$$

- runback in: mass flow rate of water flowing into the panel.

$$\dot{m}_{rb\,in\,(i)} = \dot{m}_{rb\,out\,(i-1)} \tag{2.20}$$

- evaporation: mass flow rate of water which evaporates.

$$\dot{m}_{e\,(i)} = ds\ Hg\ \frac{\dfrac{p_{ww}}{T_{surf}} - r\dfrac{p_{edge}p_w}{T_{edge}p_{surf}}}{\dfrac{p_{edge}}{0.622T_{edge}} - \dfrac{p_{ww}}{T_{surf}}} \tag{2.21}$$

- sublimation: mass flow rate of ice which sublimates.

$$\dot{m}_{s\,(i)} = ds\ Hg\ \frac{\dfrac{p_{wi}}{T_{surf}} - r\dfrac{p_{edge}p_w}{T_{edge}p_{surf}}}{\dfrac{p_{edge}}{0.622T_{edge}} - \dfrac{p_{wi}}{T_{surf}}} \tag{2.22}$$

- runback out: mass flow rate of water flowing out of the panel.

$$\dot{m}_{rb\,out\,(i)} = \dot{m}_{imp\,(i)} + \dot{m}_{rb\,in\,(i)} - \dot{m}_{e\,(i)} - \dot{m}_{s\,(i)} - \dot{m}_{ice\,(i)} \tag{2.23}$$

- icing: mass flow rate of water freezing.

$$\dot{m}_{ice\,(i)} = (\dot{m}_{imp} + \dot{m}_{rb\,in} - \dot{m}_e - \dot{m}_s)\, n_{(i)} \tag{2.24}$$

The mass transfer coefficient in equation (2.21) and (2.22) is defined as:

$$Hg = \frac{Hc}{c_p}\left(\frac{Pr}{Sc}\right)^{\frac{2}{3}} \tag{2.25}$$

$$Pr = \frac{c_p\, \mu}{k} \tag{2.26}$$

$$Sc = \frac{\mu}{\rho\, D_v} \tag{2.27}$$

Beside the energy terms related to mass flow indicated before, other energy transfer modes need to be considered; these are the kinetic energy of impacting particles, convection and aerodynamic heating. Using the same control volume concept to formulate the energy balance on the icing surface:

$$\boldsymbol{q_{w\,(i)} + q_{k\,(i)} + q_{rb\,in\,(i)} + q_{a\,(i)} = q_{e\,(i)} + q_{s\,(i)} + q_{rb\,out\,(i)} + q_{ice\,(i)} + q_{c\,(i)}} \tag{2.28}$$

Where the energy terms considered, computed considering ice at 0 K as the reference condition for zero internal energy, are:

- water: energy of impinging water.

$$q_{w\,(i)} = \dot{m}_{imp\,(i)}\,[cp_{ice}\, T_f + L_f + cp_w\,(T_{impact} - T_f)] \tag{2.29}$$

- kinetic: kinetic energy of water striking the surface.

$$q_{k\,(i)} = \frac{1}{2}\dot{m}_{imp\,(i)} V_{impact}^2 \tag{2.30}$$

- runback in: energy of water flowing into the panel.

$$q_{rb\,in\,(i)} = \dot{m}_{rb\,in\,(i)}\,[cp_{ice}\, T_f + L_f] \tag{2.31}$$

- aerodynamic: aerodynamic heating of the surface.

$$q_{a\,(i)} = \frac{ds\; Hc\; {V_{edge}}^2}{2\, c_p} \tag{2.32}$$

- evaporation: energy of water which evaporates.

$$q_{e\,(i)} = \dot{m}_{e\,(i)}\,[cp_{ice}\, T_f + L_f + cp_w\,(T_v - T_f) + L_v + cp_v\,(T_f - T_v)] \tag{2.33}$$

- sublimation: energy of ice which sublimates.

$$q_{s\,(i)} = \dot{m}_{s\,(i)}\,[cp_{ice}\, T_f + L_s + cp_v\,(T_{surf} - T_f)] \tag{2.34}$$

- runback out: energy of water flowing out of the panel.

$$q_{rb\,out\,(i)} = \dot{m}_{rb\,out\,(i)}\left[cp_{ice}T_f + L_f\right] \tag{2.35}$$

- icing: energy of ice accumulation.

$$q_{ice\,(i)} = \dot{m}_{ice\,(i)}\left[cp_{ice}\,T_{surf}\right[\tag{2.36}$$

- convection: energy lost/gained by convection.

$$q_{c\,(i)} = ds_{(i)}\,Hc\,(T_{surf} - T_{edge}) \tag{2.37}$$

The conditions at the edge of the boundary layer are needed to compute some of the terms. These are obtained from the flow solution considering the Mach number constant through the boundary layer. Hence:

$$M_{edge} = M_{surf} \tag{2.38}$$

$$T_{edge} = T_\infty \frac{1 + \dfrac{\gamma - 1}{\gamma} M_\infty^2}{1 + \dfrac{\gamma - 1}{\gamma} M_{edge}^2} \tag{2.39}$$

$$p_{edge} = p_\infty \left(\frac{T_{edge}}{T_\infty}\right)^{\dfrac{\gamma}{\gamma - 1}} \tag{2.40}$$

$$V_{edge} = M_{edge}\sqrt{\gamma R T_{edge}} \tag{2.41}$$

The energy and mass balance equations are combined to find the local freezing fraction (2.42), that is the ratio of water freezing to water entering the panel.

$$\begin{aligned} n_{(i)} = &\frac{-q_{w\,(i)} - q_{k\,(i)} - q_{a\,(i)} - q_{rb\,in\,(i)} + q_{c\,(i)} + q_{e\,(i)} + q_{s\,(i)}}{(\dot{m}_{imp\,(i)} + \dot{m}_{rb\,in\,(i)} - \dot{m}_{e\,(i)} - \dot{m}_{s\,(i)})(-cp_{ice}T_{surf} + L_f + cp_{ice}T_f)} \\ &+ \frac{(\dot{m}_{imp\,(i)} + \dot{m}_{rb\,in\,(i)} - \dot{m}_{e\,(i)} - \dot{m}_{s\,(i)})(cp_{ice}T_f + L_f)}{(\dot{m}_{imp\,(i)} + \dot{m}_{rb\,in\,(i)} - \dot{m}_{e\,(i)} - \dot{m}_{s\,(i)})(-cp_{ice}T_{surf} + L_f + cp_{ice}T_f)} \end{aligned} \tag{2.42}$$

Because of its definition, the freezing fraction can not be greater than 1. If the value computed using equation (2.42) is larger it is assumed that $n = 1$. Again, the freezing fraction can not be negative, therefore if the value computed with (2.42) is non positive it is set $n = 0$.

One of the variables in equation (2.42) is still unknown, namely the terms associated with runback water. Thus the thermodynamic balance is first solved at stagnation point, where water only enter the control volume through impingement; the mass flux of ice is then computed using (2.24) and the mass flux of runback leaving the control volume is computed using (2.23).

The runback water leaving the stagnation point is then used as an input for panel immediately downstream; here the mass flux of runback water entering is set equal to the value computed with (2.23) for the previous panel. The ice thickness at a given location is then given by equation (2.43), where the density of ice(2.44) is a function of velocity, temperature and particle diameter. Indeed, depending on icing condition the density of ice changes because of the presence of air bubble inside the ice structure.

$$b_{(i)} = \frac{\dot{m}_{ice\,(i)}\,\Delta t}{ds\,\rho_{ice}} \tag{2.43}$$

$$If\ 1 \leq \frac{-d_p\,V_\infty}{2\,T_\infty} \leq 17\ and\ T < -5°C \qquad \rho_{ice} = 110\left(\frac{-d_p\,V_\infty}{2\,T_\infty}\right)^{0.76} \tag{2.44}$$

$$Else \qquad \rho_{ice} = 917\ kg/m^3 \tag{2.45}$$

The density of ice in equation (2.44) and (2.45) is based on an empirical relation which relates density with external temperature, velocity and particle diameter, and has been derived in [14].

2.4.1 Ice temperature

When the thickness of ice to be added at each location and its properties are known the temperature on iced surface is computed. This is temperature used for the next time step as a condition on the airfoil. Depending on the freezing fraction, the value of the surface temperature is computed as follows. If the freezing fraction is less than 1, that is not all of the water freezes, the surface temperature is set equal to 273.15 K, that is the temperature of the water film. In case of a rime accretion, that is freezing fraction equal to 1, the surface temperature is computed considering the conduction through the iced layer, using equation (2.46), assuming the temperature varies linearly in the ice.

$$T_{surf(t+1)} = T_{surf(t)} + b\,\frac{q_{a\,(i)} + q_{k\,(i)} + q_{rb\,in\,(i)} + q_{water\,(i)} - q_{ice\,(i)} - q_{c\,(i)} - q_{s\,(i)} - q_{e\,(i)}}{k_{ice}\,ds} \tag{2.46}$$

Energy term associated with water freezing is computed with:

$$q_{ice\,(i)} = n\left(\dot{m}_{imp\,(i)} + \dot{m}_{rb\,in\,(i)} - \dot{m}_{e\,(i)} - \dot{m}_{s\,(i)}\right)\left(cp_{ice}T_{surf}\right) \tag{2.47}$$

Beside the temperature on the iced surface, also the initial temperature of the airfoil have to be computed. This is computed at the beginning of the process, solving the thermodynamics balance previously described. It is first assumed that the surface temperature is equal to 273.15 K, that is not all water freeze. The terms in equations (2.28) and (2.18) are evaluated using this temperature and a value for the freezing fraction is computed. Three cases are then possible:

1. Freezing fraction less than 0.
2. Freezing fraction between 0 and 1.
3. Freezing fraction greater than 1.

If the freezing fraction is between 0 and 1 than water is indeed flowing on the surface, and the guessed value for surface temperature is retained. If the freezing fraction is greater than 1 than all impinging water is freezing, therefore the surface temperature must be lower than the freezing temperature. The surface temperature is computed by solving equations (2.28) and (2.18) by imposing n = 1. This is done by applying an iterative procedure, because many terms depend on the surface temperature. In case of freezing fraction below 0 than the surface temperature is greater than 273.15 K; similarly, equations (2.28) and (2.18) are solved imposing n = 0.

Chapter 3

Numerical tool: IceMAP 2D

The numerical model presented in the previous chapter has been implemented in the tool IceMAP 2D (Module for Accretion Prediction). With this tool it is possible to simulate the ice accretion over bi dimensional bodies by means of a CFD software. The Reynolds Averaged Navier-Stokes (RANS) equations and the boundary layer are solved at predefined grid points locations. Thus, compared with panel method, it provides a more accurate flow field solution, without the limitation of a potential flow solver; indeed, with a CFD software simulations at high Mach number and high angle of attack, as well as flow separation can properly be solved.

IceMAP 2D has been initially developed so that the simulation of ice accretion could be embedded in Fluent, that is the CFD software used within the aerodynamic department of Agusta Westland. Although Fluent is used to determine particle trajectories and compute collection efficiency, it has not the capability to perform ice accretion simulation This module has been completely developed; the tool is written in the C language and integrated using the user-defined functions, which are part of Fluent and designed to interact with the solution process. Thus, also the solution of the thermodynamic balance has been integrated within Fluent. This allows to use all the capabilities of the CFD; the flow field and particle tracking are computed by Fluent, but also the variables used in the solution of thermodynamic balance on the surface are derived directly from the flow field solution, as is the case for the heat transfer coefficient. The need for empirical relations, necessary to provide a solution of the boundary layer and a value of heat transfer coefficient, is thus eliminated.

ANSYS® Workbench™ has been used to integrate in a single application the whole process, creating a loop that includes also the mesh generation and modification (time stepping capabilities). An algorithm has been implemented to manage the process in Workbench, and eventually it has been fully automated.

IceMAP 2D requires as input flight and icing conditions, together with the airfoil geometry, while the rest of the process does not require any user intervention, and gives as a result the final ice shape and the aerodynamic coefficients on the iced body.

3.1 Procedure for ice accretion computation

As ice grows on the airfoil, the flow field and the impinged area on the surface changes. Therefore, the total accretion time is divided in a discrete number of smaller time step, and at each step the solution process is repeated. At each time step the ice accretion simulation is composed of different blocks, that have to be executed sequentially in order to obtain the final results.

The blocks composing the accretion process are visible in the flow diagram 3.1. It is first necessary to define all of the input required for the icing simulation, which can be divided in definition of the geometry of the body and the external conditions; these include the free stream conditions of the flow, like velocity and temperature, and the icing conditions, like particle diameter and number of time steps.

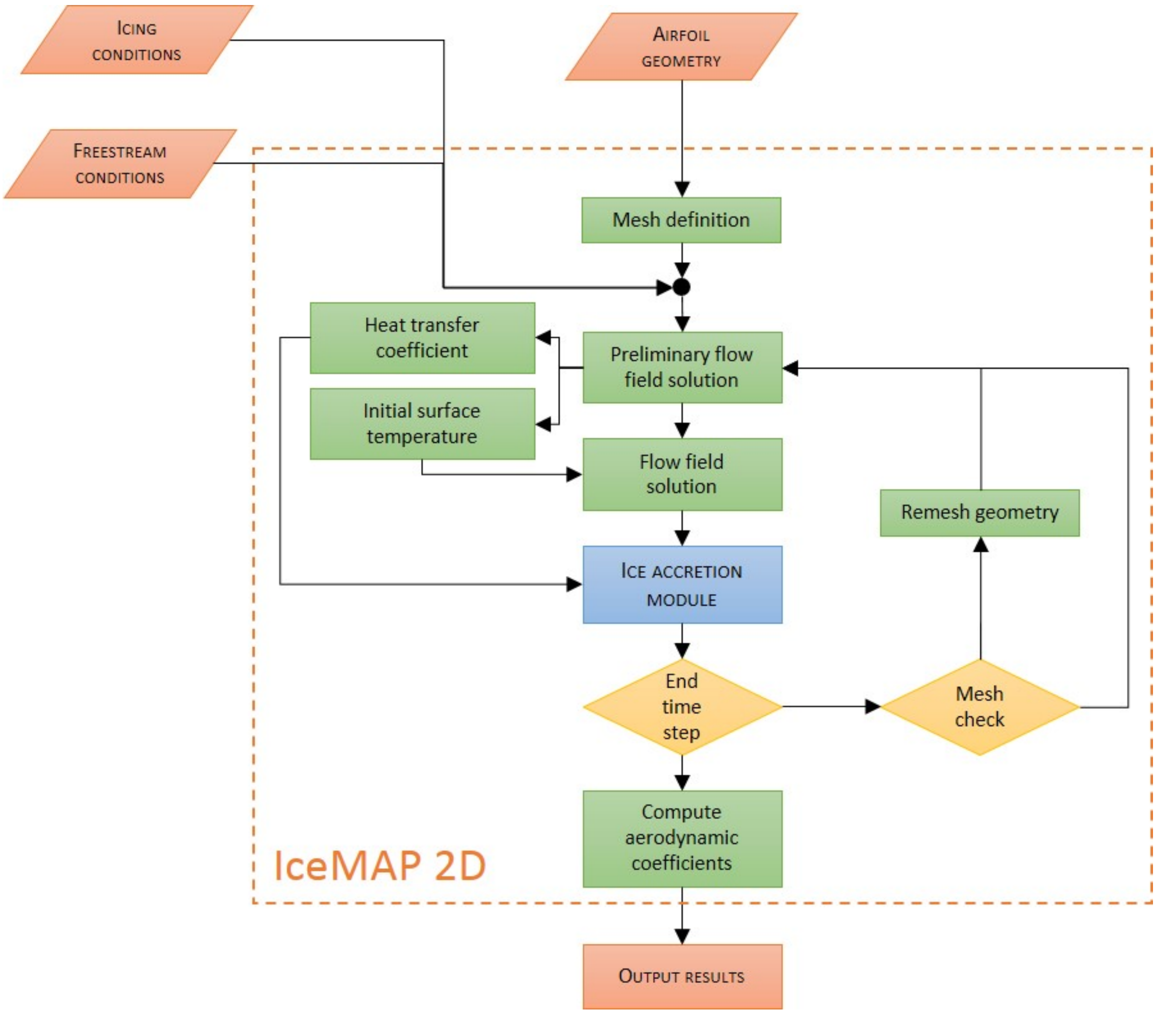

Figure 3.1: Illustration of the solution process with IceMAP 2D.

The geometry of the surface is then used to define the computational domain and the creation of the proper mesh. Using the input free stream condition the flow field solution is then computed solving the Navier-Stokes equation by means of Fluent; the initial temperature of the surface and the heat transfer coefficient between the body and the air can thus be determined. With the correct surface temperature the flow field is solved again, so that the forces acting on the droplets and local aerodynamic field around the body can be computed.

At this point the ice accretion module can be launched, which can be divided in three major blocks: particle tracking, solution of the thermodynamic balance and geometry and mesh update. The blocks are visible in 3.2, and have been implemented in Fluent mainly through the usage of user defined function. Initially a discrete number of particles are tracked through the fluid domain to determine where and what rate they impact they body, so that the collection efficiency and impinging mass at each surface location can be computed.

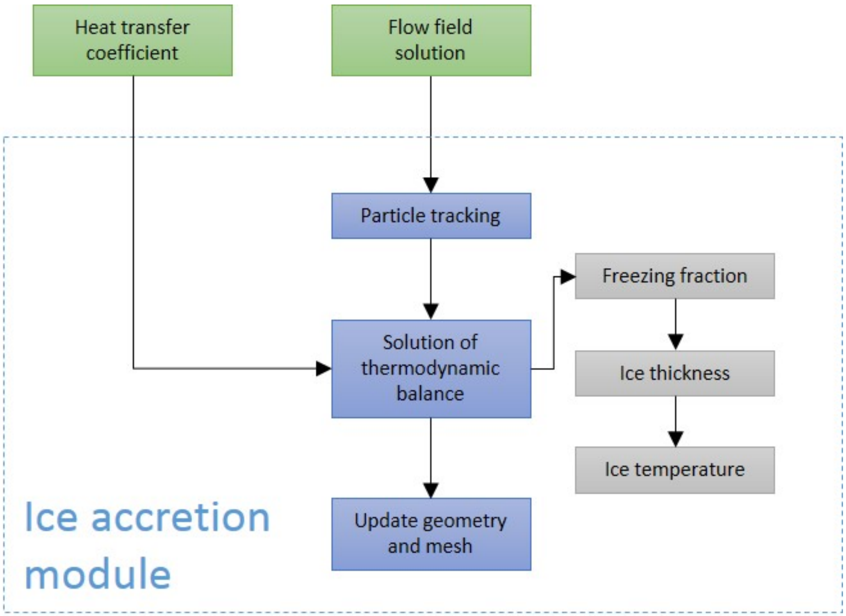

Figure 3.2: Ice accretion module, implemented in Fluent using user defined functions.

With the data from the particle tracking and the flow solution the thermodynamic balance is solved on the surface; this allows to determine the fraction of water that freezes on the surface and using the time increment specified by the user also the ice thickness to be added. The temperature on the iced surface is then computed and used as a boundary condition for the subsequent flow and thermodynamic solution. The last step of the ice accretion module is the geometry and mesh modification to take into account the deformation due to the ice accumulation.

At the end of each ice accretion module IceMAP 2D checks whether the requested number of time steps has been reached; if other time steps are required, the quality of the mesh is controlled and recreated if necessary to ensure that it meets certain quality requirements before repeating the process. If the required number of time steps has been reached the aerodynamic coefficients on the iced airfoil are computed.

This iterative process thus can be divided in:

1. Mesh definition.

2. Heat transfer coefficient determination.

3. Flow field simulation.

4. Discrete phase simulation.

5. Thermodynamic balance solution.

6. Ice accretion.

7. Mesh check.

3.1.1 Workbench

ANSYS Workbench combines access to all of ANSYS applications and manages the workflow among them. Applications that are integrated and can be accessed include ANSYS DesignModeler™, for the creation of geometries, ANSYS Meshing™, as the default mesher, and ANSYS Fluent for flow solutions. The applications available combine to create a single project, driven by a schematic workflow that manages the connections between the systems. The applications necessary for the ice accretion simulation, DesingModeler, Meshing and Fluent, are all integrated in Workbench and this simplifies the creation and implementation of a suitable solution process.

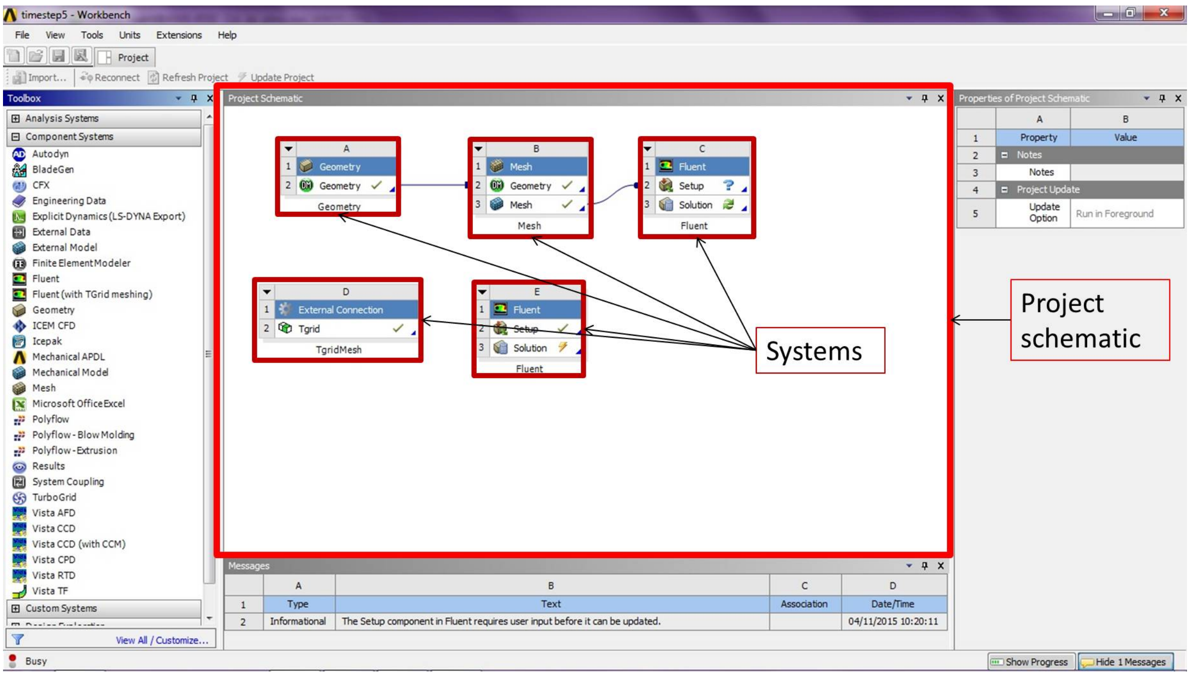

Figure 3.3: ANSYS Workbench project schematic.

Interaction with applications and other utilities native to Workbench is possible through the schematic; applications are also data integrated, that is even if they have different interface their generated data is part of the Workbench project and automatically saved and shared with other applications. This greatly streamlines the process of creating a CFD simulation, especially when more interactions between systems are required.

A single project may be composed of different systems, which can be updated sequentially based on a predefined workflow defined in the project schematic; for instance, when geometry component is modified with the new geometry, the mesh component can be updated directly from the Workbench schematic without opening the ANSYS Meshing application. Additionally, also external application can be integrated in the Workbench, and their data can used by other system.

As stated, the process developed for ice accretion simulation involves different steps, which also need to be repeated: geometry and mesh creation, flow solution and ice accretion with Fluent, mesh update. The whole process can be included in a single Workbench project, which greatly simplify the management of different components required. An additional advantage of using Workbench resides in the scripting and journaling capability, that is the possibility of writing a set of instructions to be executed and record the action performed via the graphical user interface. Scripts and journal are written in the Python language, and they allow to replay simulations already run as well as to automate repetitive analyses.

With scripting, it is also possible to interact and launch applications integrated in ANSYS Workbench. Although for some applications is not possible to directly modify the operations executed, it is possible to use their own native scripting language; for example, operations in DesignModeler, used to create the domain geometry and based on JavaScript, are not journaled in Workbench, but is possible to launch script from the Workbench.

All these capabilities make ANSYS Workbench ideally suited to contain an iterative process as an ice accretion simulation is. Further, the process can also be automatized using a script written in python language. Using a script all the capabilities of ANSYS Workbench are available, but without the need to directly interact with any of the systems. Indeed, a single script is responsible of creating the various systems needed, launching applications when required and sending the appropriate commands. This completely eliminates the need of user intervention; a minimal number of input are required, while the script manages the whole process until a final ice shape is obtained.

3.1.2 UDF development

A user-defined function is a function written in C that can be loaded in Fluent to enhance its features; using UDF is possible to customize boundary conditions, execute on demand some operations, contained in a UDF, enhance post-processing and models existing in Fluent, such as discrete phase model. User defined function are defined using macros supplied by Fluent, and have access to the solver data and may also perform other tasks. Thanks to the UDF feature, that allows the information exchange with the solver, the ice accretion module has been completely integrated in Fluent.

The solution process in Fluent, considering UDFs, for the pressure-based coupled solver begins with a two steps initialization sequence that is executed outside of the solution iteration loop. The solution iteration loop begins with the execution of ADJUST UDFs, used to adjust or modify Fluent variables (for example velocities or pressure). Next, Fluent solves the governing equations of continuity and momentum in a coupled fashion. Energy, species transport, turbulence, and other transport equations are solved sequentially, calling UDFs when necessary; finally, a check for either convergence or additional iterations is done, and the loop either continues or stops.

The ice accretion module is written as a user defined function, executed on demand after the flow field solution has been obtained. To work properly, it needs additional UDFs, which are used to initialize local variables, define particles properties, boundary conditions for the discrete phase model, and to store variables from the particle tracking.

Finally, the update of the mesh based on the iced geometry is also governed by a user

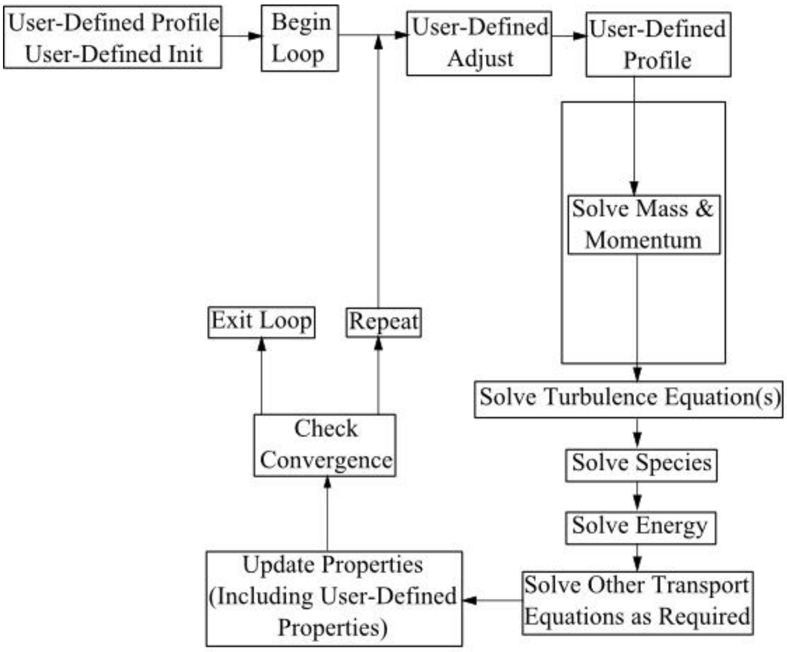

Figure 3.4: Solution process of Fluent with UDFs. Image from [3].

defined function, which is called in the mesh morphing process in Fluent to define the new nodes positions.

3.2 Geometry and Mesh

The solution of the flow field is computed considering a C-shaped computational domain (figure 3.5), with the frontal arc centred on the leading edge of the airfoil. The overall size of the domain is defined in number of chords before and after the airfoil, and can be specified by the user. The domain have to be large enough so that the flow at the boundaries is not altered by the presence of the airfoil.

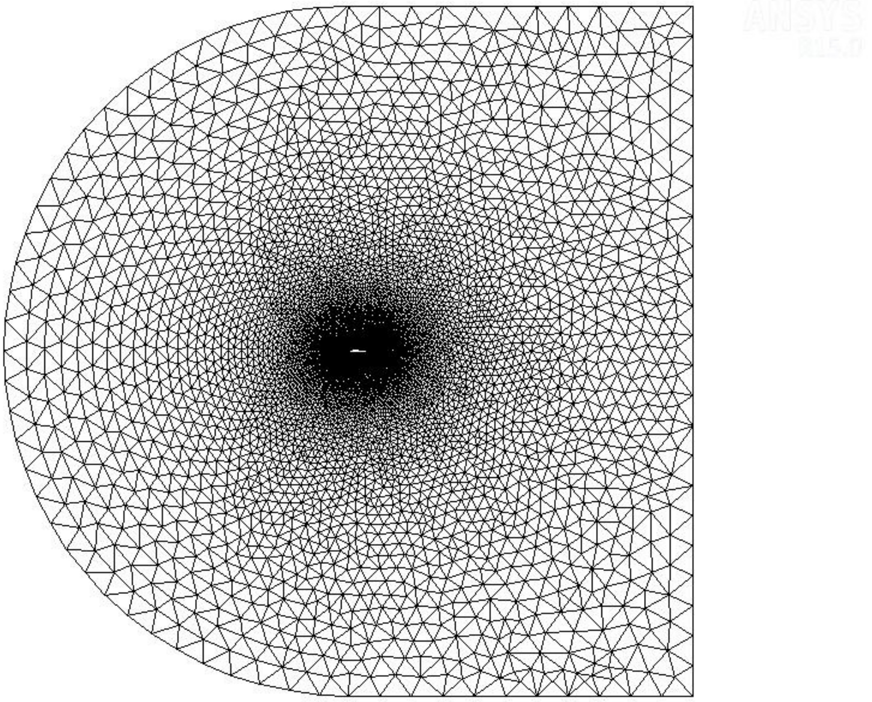

Figure 3.5: Domain and mesh used. The airfoil is at the centre of the domain.

Fluent solves the given set of equations in a number of discrete points in the domain; the discretization and resolution of the domain influences the accuracy of the solution as well as the computation cost of the simulation. The volumetric mesh has be built considering two key parameters: the accuracy of the simulation and the computational cost involved. The accuracy of the flow solution directly impacts the aerodynamic characteristics and the parameters computed on the airfoil; therefore, the particle trajectories and the solution of the thermodynamic balance on the surface are affected and may result in a large difference in the computed ice shape. Computational costs are involved both in the mesh generation process and in the flow solution via CFD. Moreover, because the simulation is a multi step procedure, at each step the geometry and the mesh have to be modified if not completely regenerated. This is the result of the complex shapes typical of ice formation, which may invalidate the mesh generated for the previous time step. Figure 3.6 and 3.7 provide an example of the large difference between the clean and iced airfoil and the mesh differences. Beside the costs due to the mesh generation also the flow solution has to be computed at each time step, which further increase the computational demand. Minimizing the computational costs can thus significantly reduce the time required to run a simulation.

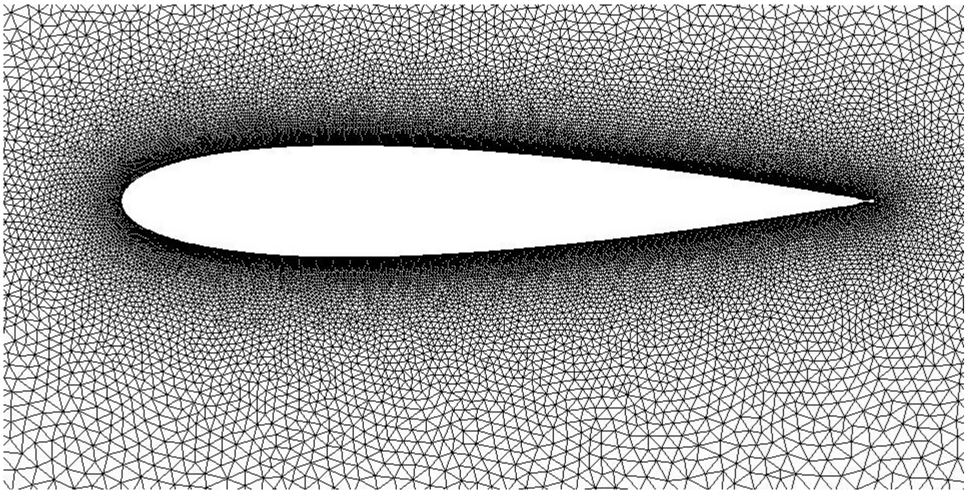

Figure 3.6: Mesh for a clean airfoil NACA0015. Unstructured, triangular mesh.

The volumetric mesh used, as can be seen in figure 3.6, is an unstructured grid made by triangular elements. The creation of structured mesh, consisting of quadrilateral element, may in case of large ice accretion be extremely difficult and time consuming; additionally, in structured quadrilateral mesh the distribution of cells may be less efficient, because the mesh structure forces a fine resolution in areas where it is not required. As a result the computational time necessary to generate a structured mesh is elevated and may result in an unnecessarily high cell count. On the contrary, triangular meshes generally require less setup time and allows more freedom in the placement of cells, thus allowing clustering of elements in specified regions of the flow domain. In icing simulation large horns and irregular surfaces may be expected, as can be seen in figure 3.7, and the advantages offered by triangular mesh are particularly useful.

Generally, increasing the number of elements of the mesh a more accurate flow solution is obtained, at the expense of the computational time, which is heavily increased by the mesh generation and flow solution process. A proper clustering strategy can be employed to significantly reduce the number of cells without deteriorating the accuracy of the flow solution. The element size is variable on the domain, so that the cells are larger far from the airfoil, where the flow is slightly influenced by the presence of the airfoil; on the contrary, near the airfoil the size of cells is dramatically reduced, so that smaller flow characteristic can be distinguished.

To better model the boundary layer the mesh should be particularly refined near the wall; a characteristic of quadrilateral cells is that they permit a larger aspect ratio (that is base length to height ratio) than triangular cells, because for the latter it also impact the skewness and may impede the accuracy and convergence of solution. In the case of the boundary layer, though, it can be modelled using some layers of quadrilateral cells on the surface of the airfoil. In the boundary layer the flow is aligned with the airfoil, and the length of the cells does not affect the accuracy of the solution.

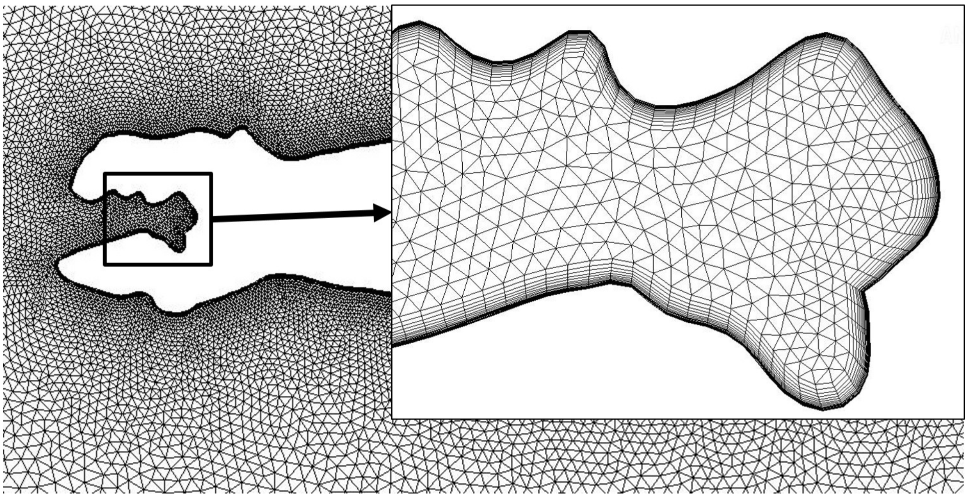

Figure 3.7: Mesh for an iced NACA0015; detail of mesh elements near the leading edge of the clean airfoil.

3.2.1 Mesh creation

A control on the mesh discretization has been provided, which allows to define the size of the elements on the icing surface. This affects not only the mesh size on the surface, but also the overall size distribution; indeed, the base dimension for the prism layer is the face size defined by the user; this further propagate to the subsequent triangular area, as the distribution of the cell size in the interior is defined considering the face size on the boundary, which is the defined by the user. Therefore, the choice of the surface discretization has also a substantial influence on the mesh size near the airfoil and provided good control on the overall size; therefore a single control has been made available, which contributed to reduce the number of settings required.

If needed, though, further control may be accessed by modifying the scripts written to generate the mesh; thus the prism layers characteristics, the size of the triangular mesh in the domain and the type of mesh generated can be controlled. By default, the prism zone comprises 20 layer of quadrilateral cells; the height of the first cell layer is set at 5e-6 m, while the last layer has a thickness that is equal to 25% of the first layer local base mesh size. The settings used proved to be acceptable for all the simulations conducted, and therefore it is not expected to require modifications.

A study of the effects of varying mesh size has been conducted, but further testing is required to provide better guidance to the user. Indeed, in the ice accretion simulations some issues have been observed which are the result of an improper mesh size choice.

Initially, the element size of the mesh was set at 0.1 mm, selected considering exclusively the accuracy of the aerodynamic results. When computing the distribution of the impinging mass on the airfoil, on either the clean or iced airfoil, it resulted in highly irregular distribution, caused by the small size of the elements employed. This is visible in figure 3.8. As a consequence, the impingement distribution had to be smoothed to provide a more realistic result. This also reflected on the shape, which showed large variability even for rime accretion and a reduced number of time steps.

A different approach has been used instead; the mesh on the airfoil has been coarsened, using a larger panel size, so that the mass of impinging water can be used immediately

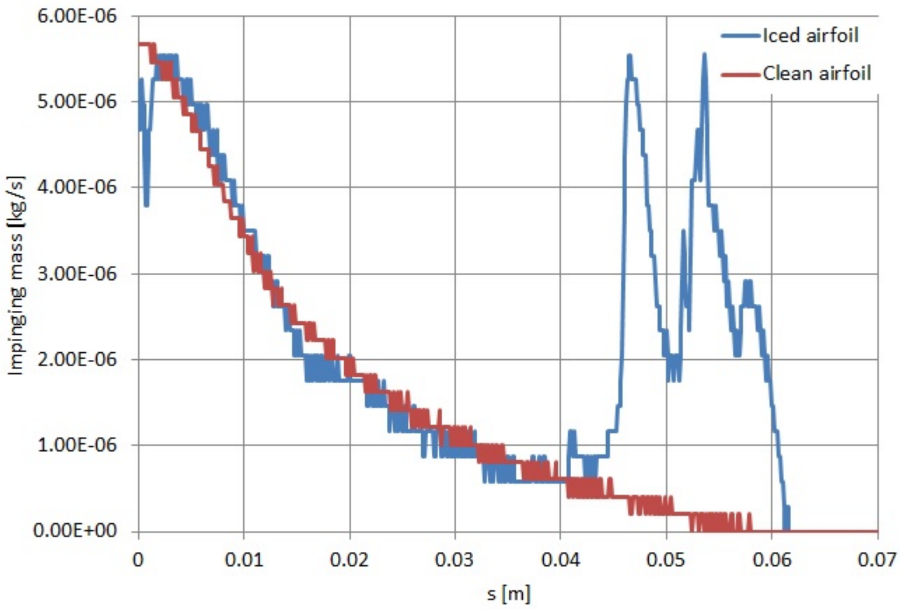

Figure 3.8: Impinging water on clean and iced airfoil, element size 0.1 mm, no smoothing.

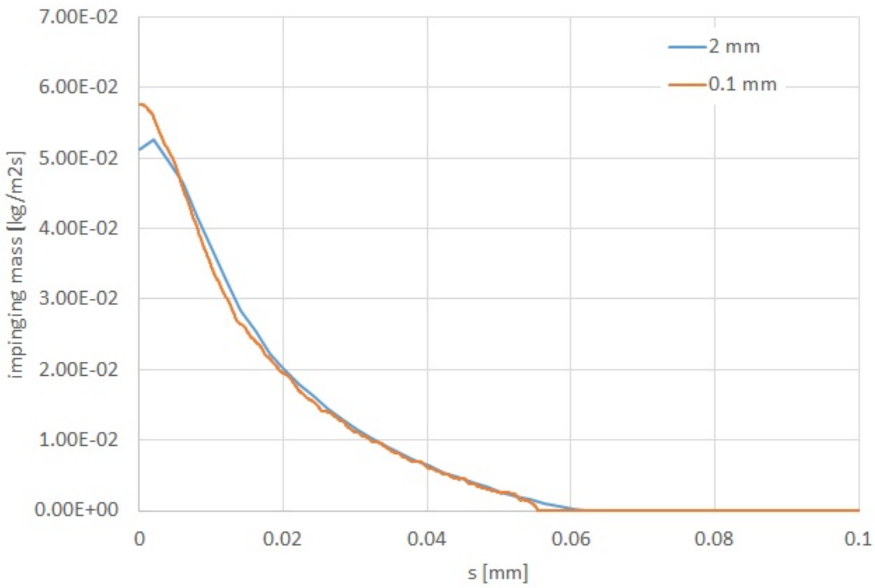

Figure 3.9: Impinging water on a clean NACA0012 airfoil, mesh size 0.1 mm and 2 mm.

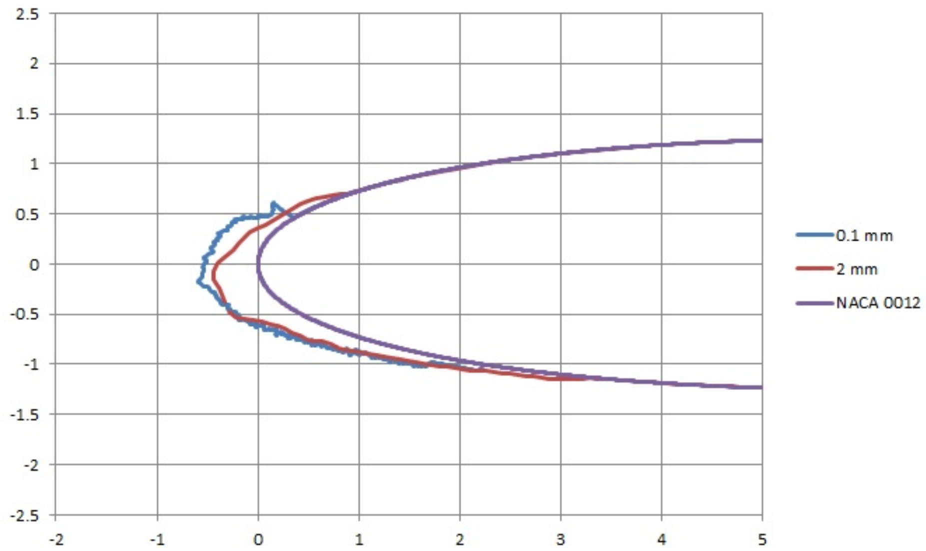

Figure 3.10: Ice shape with mesh size of 0.1 mm and 2 mm.

in the computation of the iced characteristics. The difference in the computed impinging mass with element size of 0.1 mm and 2 mm is visible in figure 3.9; in the finer mesh size the impinging mass was smoothed, but still presented some irregularities. In figure 3.10 also the final ice shape is computed, using two time steps for the finer mesh and five for the coarse mesh. Although ice accretions are not smooth, the irregularities visible using the finer mesh can not be considered representative, because they are the results of the numerical inaccuracies in the impinging mass, visible in figure 3.9. Additionally, the number of time steps usable was dictated by the difficulties encountered in the generation of the mesh for iced surface, because it often resulted in invalid cells near the surface. The issues noted for the finer mesh are largely eliminated considering coarser mesh element.

Some tests have also been conducted by further increasing the size of the surface elements; these resulted in an excessive simplification of the geometry, thus the final ice accretion may be missing relevant ice features like horns. In figure 3.11 the simplifications caused by the excessive size of the mesh are clearly visible.

The external conditions are the same in both cases, and are representative of a prolonged (22.5 minutes) glaze accretion a GLC305 airfoil with a 0.91 m chord length. When the coarser mesh is used, the final ice shape only has limited resemblance to the experimental shape, as the horns are completely missing. Halving the mesh size largely improves the result, and in the final accretion also the presence of horns is visible. In this case the difference is especially clear, as the airfoil used is particularly thin; the maximum thickness of the airfoil is indeed of only 7 cm, for which a 4 mm element size represents a considerable part of the leading edge section. In this specific case no tests have been conducted using smaller mesh size, but may further improve the results.

For the cases considered the size of the mesh is generally around 1 mm, with some variability due to the overall length and thickness of the airfoil simulated; for smaller objects, like a 0.15 m NACA0012, a 0.5 mm has been used without adverse effects.

Based on the tests executed, the user should use a mesh size between 0.5 and 2 mm,

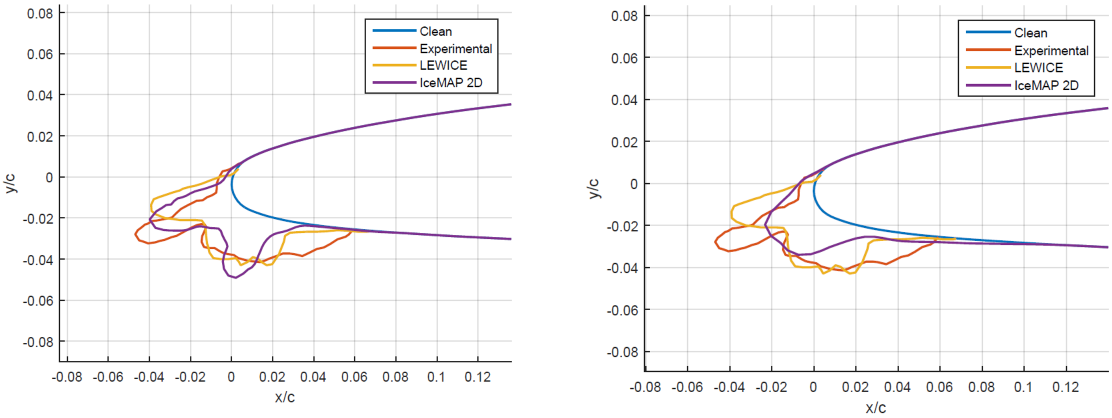

Figure 3.11: Effect of mesh size on ice accretion. Mesh size: 2 mm left, 4 mm right.

which has been found appropriate for most simulations; the choice should be based principally on the thickness of the specific airfoil, and in second instance on the chord length. Although no comprehensive series of tests on the effect of mesh size on ice accretion has been conducted, the 2 millimetres used in the previous example can be safely considered as an upper limit that should not be exceeded, unless for particularly long and thick object. In some cases also smaller elements may be appropriate, but numerical problems may arise.

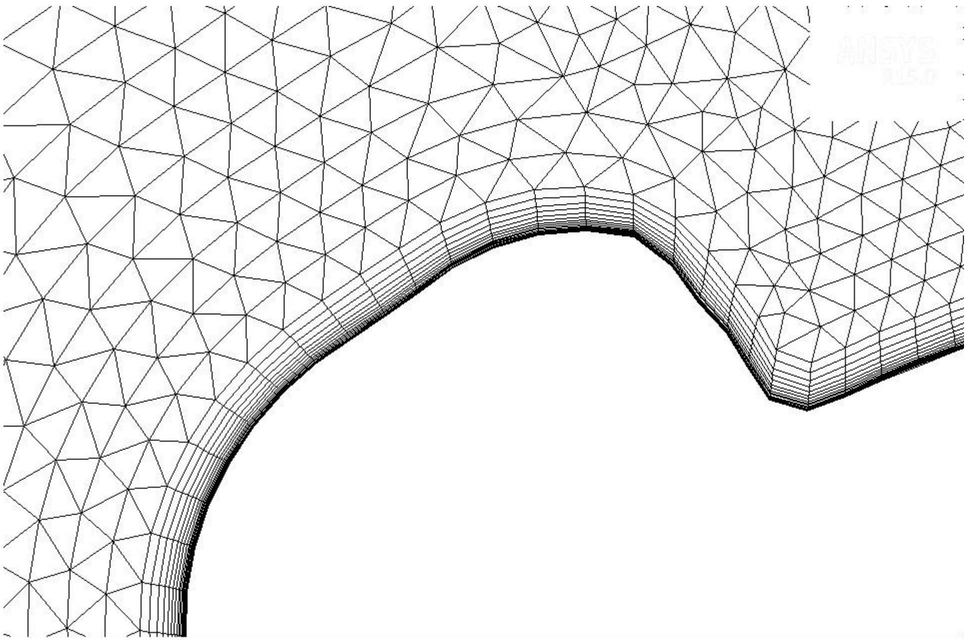

Figure 3.12: Detail of the mesh used for ice accretion. Element size 2 mm.

The mesh size previously indicated is used in the computation of the ice growth and generally provides satisfactory results in the computation of the aerodynamic characteristics of the airfoil. To ensure that the flow over the surface is properly modelled, a different

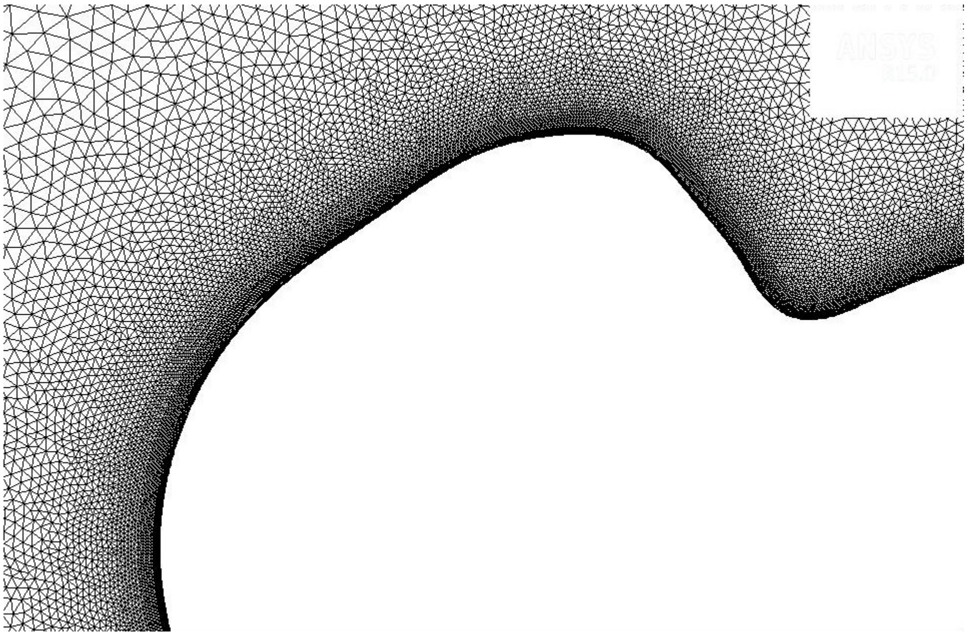

Figure 3.13: Detail of the mesh used for aerodynamic purpose. Element size 0.1 mm.

mesh size may be specified for the determination of the aerodynamic characteristics of the final ice shape. An example of the different refinement in the mesh used in the accretion process and the final computation of the aerodynamic characteristic is shown in figure 3.12 and 3.13. The element size for the aerodynamic mesh is set by default at 1e-4 m, as in 3.13, which guarantees adequate modelling of the flow under all the conditions tested and that may be expected.

A different value may be used, which should be dictated only by aerodynamic considerations, as the negative effects noted in the ice accretion process are not present here. As a consequence of the finer mesh also the aerodynamic coefficients computed should be more representative of the actual values compared to those computed with a coarser mesh. The computational cost of the simulation is also increased, but can be accepted considering that the mesh is only used for a single flow solution.

3.2.2 Mesh refinement

The default mesher in Workbench is ANSYS Meshing, which is integrated with the other applications used. Therefore, the iced geometry could be automatically imported in the meshing tools, and similarly the generated mesh was imported in Fluent without intervention.

Despite the inherent advantages of using ANSYS Meshing, it has been found that in many circumstances can not generate the desired mesh. Therefore, in some cases the representation of the boundary layer using the prism cells is completely missing, or the cells created are highly skewed; this occurs especially in the case of glaze accretion, near horns or irregular shapes. As a result, it is not possible to compute an accurate solution of the flow in Fluent. A unique solution that can provide an acceptable mesh, with all the characteristics required, for the possible ice shape, thus including glaze accretion, has not been found.

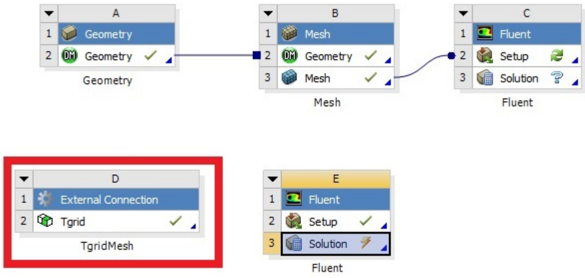

Figure 3.14: Tgrid in the project schematic of ANSYS Workbench.

Because of the issues encountered, ANSYS Meshing is only used to generate a discretization of the boundaries of the domain, which is then imported in an external mesher, Tgrid™, which is widely used in AgustaWestland, including for the generation of meshes on iced airfoil. To maintain the process in the framework provided by ANSYS Workbench, Tgrid has been integrated using the External Application system.

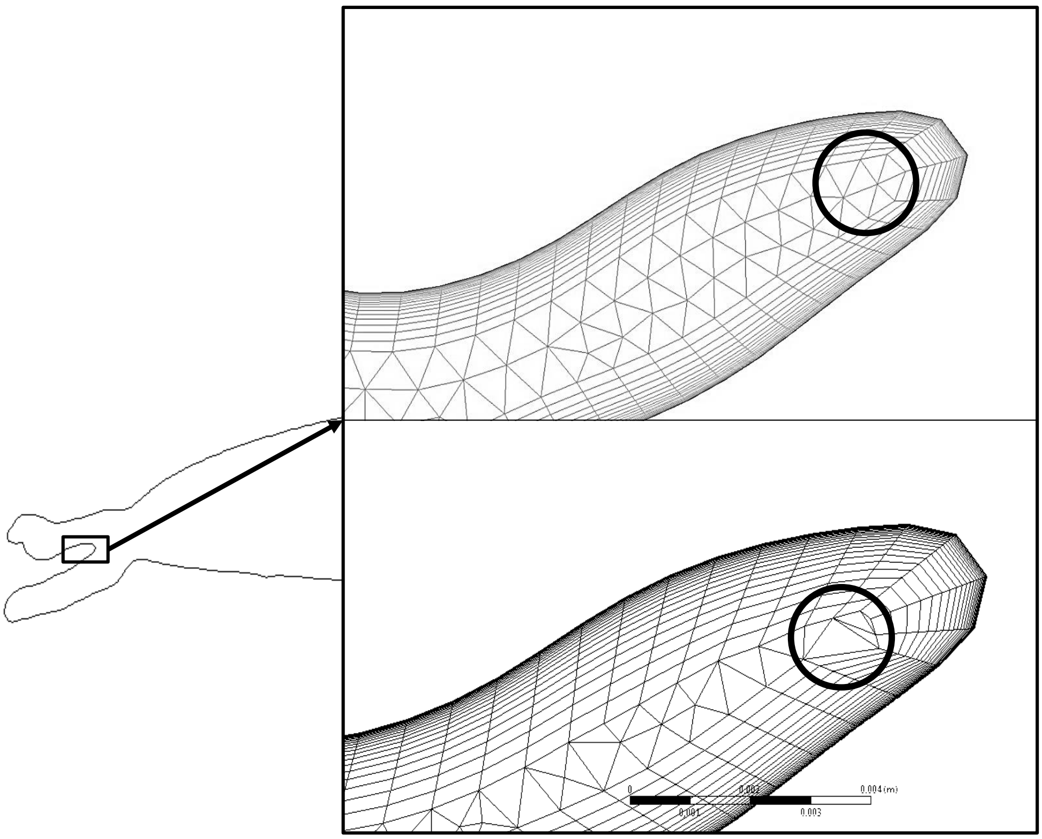

Figure 3.15: Mesh near horns, Tgrid top and ANSYS Meshing bottom.

With Tgrid it is possible to obtain the meshes as intended, even in the case of glaze ice accretion. Additionally, the meshing process in Tgrid can be more easily scripted and modified if need arise. On the contrary, ANSYS Meshing lack any kind of documentation that could help the scripting process.

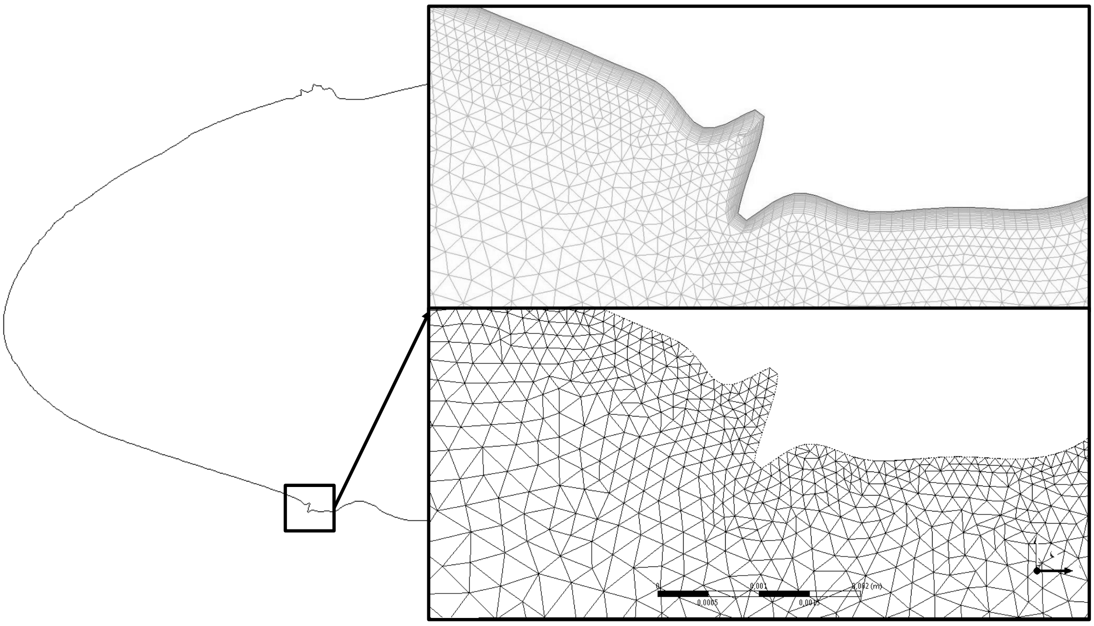

Figure 3.16: Mesh on iced airfoil, Tgrid top and ANSYS Meshing bottom.

Image 3.15 shows the same geometry meshed with ANSYS Meshing (bottom) and Tgrid (top); here a glaze accretion has produced two horns close to each other, and ANSYS Meshing produces some highly skewed cells outside the boundary layer (circled in red). Because of their presence, the convergence of the solution in Fluent is impeded. The top of figure 3.15 shows the same area meshed by Tgrid using the same parameters for mesh size and no skewed cells are present.

In figure 3.16 an irregular accretion on the iced surface is visible; in this case ANSYS Meshing (bottom) fails to generate the layer of prisms representing the boundary layer. As a result, even if Fluent provides a solution, it is not accurate because the modelling of the boundary layer is completely missing. Also in this case Tgrid manages to generate a mesh with the layers of quadrilateral cells on the iced surface.

3.3 Heat Transfer Coefficient

Heat transfer coefficient is an important variable in the simulation of ice accretion. This can be clearly seen in image 3.18: two runs with the same icing conditions have been performed, but the heat transfer coefficient has been computed using a different turbulence models and surface roughness. The computed heat transfer coefficient in the two cases is shown in figure 3.17, while the final ice shape, obtained with the different values of heat transfer coefficient, is given in figure 3.18. The variability of ice shape is the result of the many terms in the energy balance (equation (2.28)) that depend on heat transfer coefficient, like convective and evaporative cooling. These terms are responsible for the freezing of water, thus at lower values of heat transfer coefficient will correspond a decrease in ice formation.

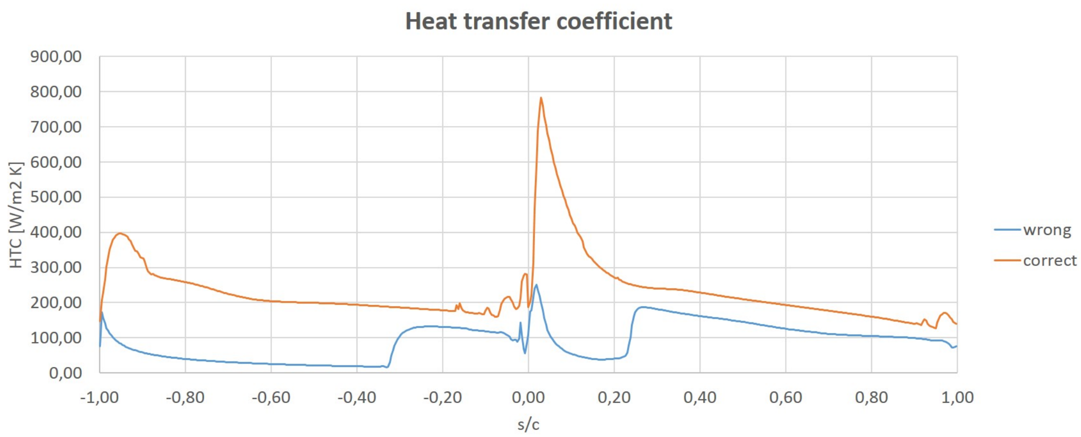

Figure 3.17: Heat transfer coefficient computed with different roughness and turbulence model.

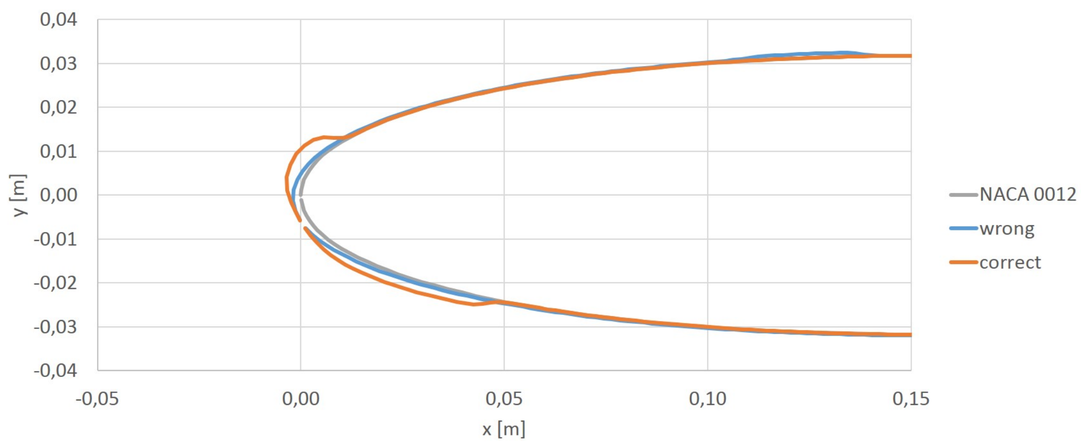

Figure 3.18: Ice accretion with different heat transfer coefficient.

The heat transfer coefficient is significantly increased by the roughness of the iced surface, and in Fluent also by the turbulence model employed. Thus it is essential to determine how to compute surface roughness to properly simulate the roughness of the iced surface and which turbulence model is the most suited to estimate heat transfer coefficient. Moreover, it has been found that changing the settings for thermal boundary condition on the airfoil influence the computed heat transfer coefficient.

3.3.1 Effect of surface roughness

Clean aerodynamic surface can be considered smooth, but the growth of ice leads to the development of surface roughness; the transition to turbulent flow is caused primarily by the increase in surface roughness, which decides the location of laminar/turbulent transition. The surface roughness therefore enhance the heat transfer coefficient by increasing the effective area on the airfoil and increasing the skin friction coefficient. Experimental studies[16] show that roughness is higher for glaze accretion, while is relatively moderate for rime ice.

In report [12] the local heat transfer coefficients for a smooth and roughened NACA 0012 were measured in flight at different angles of attack. Roughness was simulated attaching hemispheres of 2 mm diameter on the surface of the airfoil on a predefined pattern.

The heat transfer coefficient measured in [12] for a smooth and a roughened airfoil are shown in figure 3.21 and 3.22, while the distribution of the roughness element on the surface is visible in figure 3.19 and 3.20.

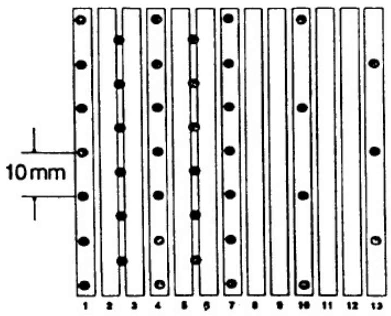

Figure 3.19: Dense roughness pattern on airfoil. Location identified by the number, with 1 = -0.036 s/c and 12 = 0.095 s/c. Heat transfer coefficient measured at 0° and 4°.

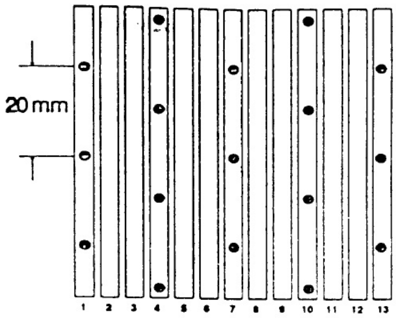

Figure 3.20: Sparse roughness pattern on airfoil. Location identified by the number, with 1 = -0.036 s/c and 12 = 0.095 s/c. Heat transfer coefficient measured at 0°.

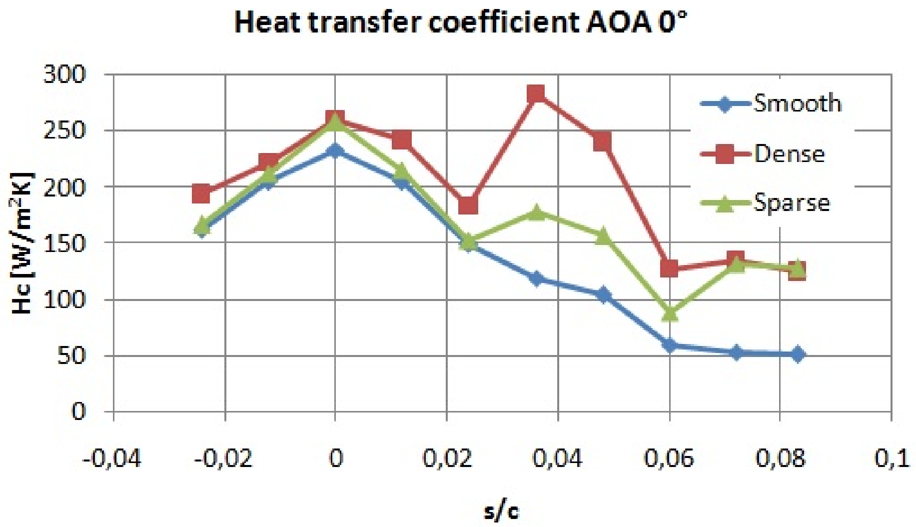

Figure 3.21: Heat transfer coefficient measured in flight for smooth and roughened NACA 0012, angle of attack 0 °. Two roughness pattern used. Data from [12].

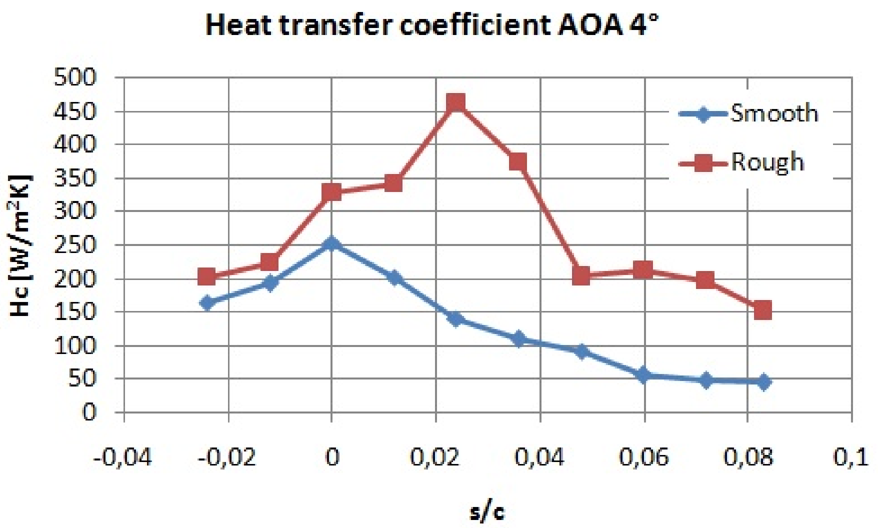

Figure 3.22: Heat transfer coefficient measured in flight for smooth and roughened NACA 0012, angle of attack 4 °. Data from [12].

The data were obtained at an angle of attack of 0 and 4 degrees. The dense pattern was used for both angles of attack, while results for the sparse pattern are only shown for 0 degrees angle of attack. In both cases the heat transfer coefficient for the roughened airfoil is larger than for the smooth airfoil, especially downstream of the stagnation. The difference increases when the density of roughness element increases, as the boundary layer is more and more influenced by the roughness. The variation of the heat transfer coefficient at some location is extremely large, with values more than doubling over their corresponding smooth value. This is even more dramatic increasing the the angle of attack, where the measured heat transfer coefficient is at some point more than four times larger than the smooth value.

A similar effect can be observed in Fluent and is visible in figure 3.23, where the heat transfer coefficient is computed for a smooth and roughened surface under the same external conditions. The value is similar at the stagnation point, but further aft on either the upper or the lower airfoil surface the difference becomes significant and results in drastically different ice shape. Because of the lower heat transfer coefficient less water freezes immediately and flows on the surface, eventually freezing at some location downstream. Therefore, the ice thickness at the stagnation is reduced, while ice grows past the experimental accretion limits. This is clearly visible in figure 3.24 and 3.25, which represents a three minutes glaze ice accretion on a NACA 0012 airfoil. The only difference in the simulation process is the inclusion of the surface roughness in 3.25; the modified heat transfer coefficient is visible in figure 3.23. Although this is a short simulation the ice shapes are already quite different, and it is expected to become more significant for longer accretion time.

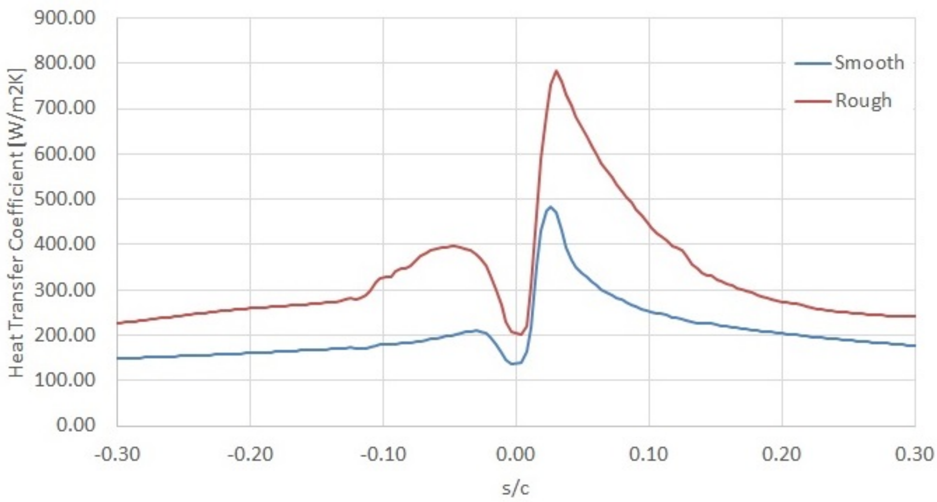

Figure 3.23: Heat transfer coefficient for a smooth and rough NACA 0012; the final ice shape with the different values of htc is visible in figure 3.24 and 3.25.

Because of the large variation of heat transfer coefficient with surface roughness, and its influence on the ice accretion, it is necessary to model the roughness, also considering its variability with icing conditions and the type of ice growing.

The lack of detailed informations on how roughness varies with icing conditions has lead to the development of empirical correlations to calculate an equivalent sand grain

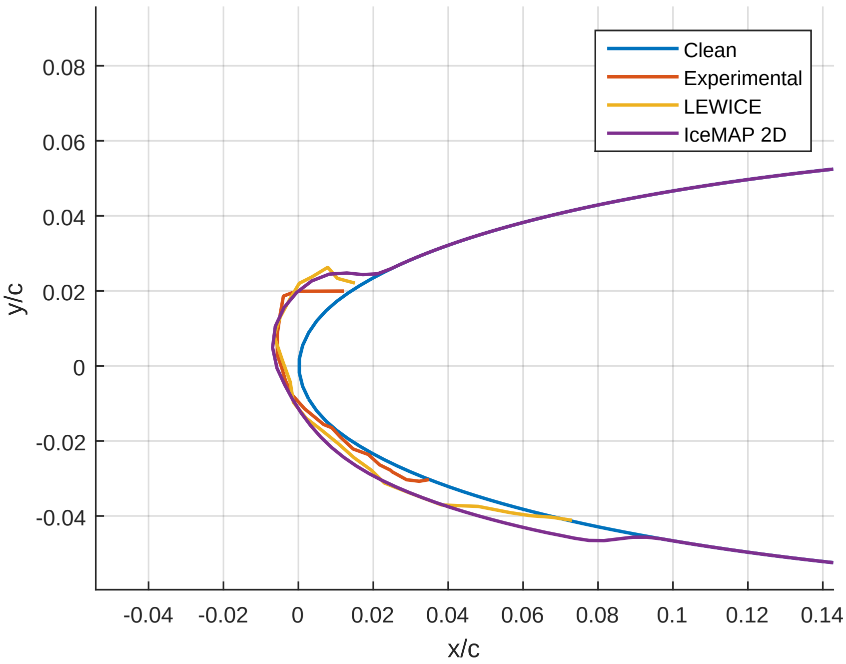

Figure 3.24: With surface roughness.

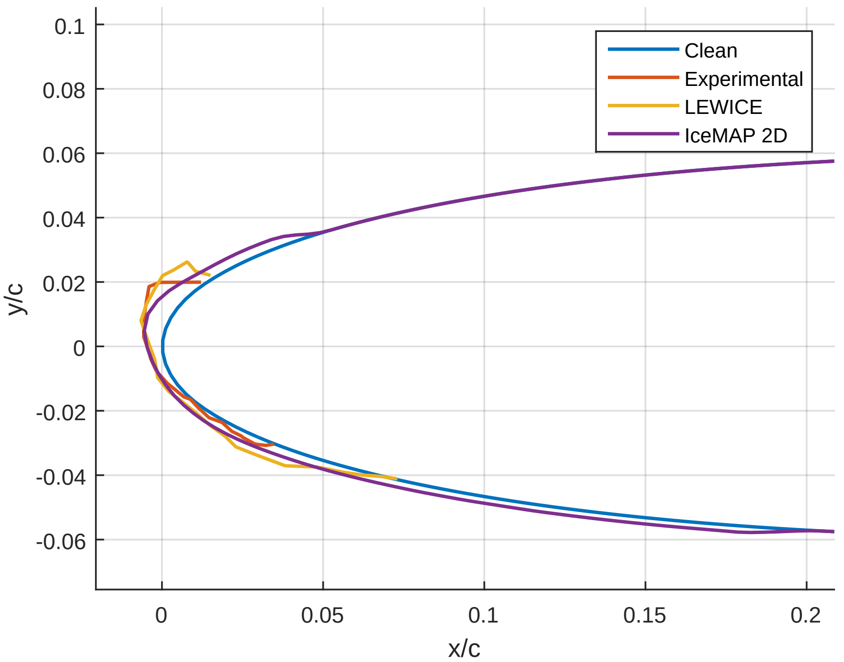

Figure 3.25: Without surface roughness.

surface roughness, which do not take into account the physics of ice accretion or the actual conditions of the iced surface. Instead, they are based on the selection of the surface roughness that best fits the experimental ice shapes.

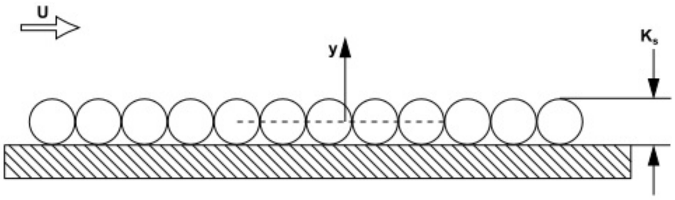

Figure 3.26: Illustration of the equivalent sand grain roughness concept employed in Fluent.

Surface roughness is computed using a correlation presented in [14] and developed by the author. Ruff correlation given in (3.1) uses external conditions (velocity, temperature and liquid water content) to estimate the average surface roughness on the iced surface. The correlation is based on experimental data presented in [1].

$$\begin{aligned} ks &= ks_{V_\infty}\, ks_{LWC}\, ks_T\, 0.00117\, chord \\ ks_{V_\infty} &= 0.4286 + 0.0044139 V_\infty \\ ks_{LWC} &= 0.5714 + 0.2457 LWC + 1.2571 LWC^2 \\ ks_T &= 46.8384 \left(\frac{T_\infty}{1000}\right) - 11.2037 \end{aligned} \tag{3.1}$$

In equation (3.1) the velocity is in m/s, the LWC in g/m^3 and the temperature in K. These three icing parameters were selected because of their influence on the type of ice growing, and because a complete set of experimental data existed from which to form a correlation. The model has some limitations, due to the fact that it does not take into account the physics of ice accretion, especially for glaze condition, when a water film covers the iced surface. For this reason improving the surface roughness model could improve the final ice shape, especially in glaze condition.

In Fluent the equivalent sand grain surface roughness computed using equation (3.1) is then specified in the boundary conditions for the airfoil, so that the fluid flow is computed considering a rough surface.

3.3.2 Effect of turbulence model

The heat transfer coefficient is largely influenced by the boundary layer on the airfoil and therefore its modelling has a significant impact on the computed heat transfer. In Fluent many different formulation for turbulence are available, but it has been found that not all of them provide accurate results for the heat transfer coefficient. As an example, figure 3.28 and 3.29 show a three minutes glaze accretion over a NACA0012 airfoil, where the heat transfer coefficient, shown in figure 3.27, is computed using the $k\epsilon - realizable$ turbulence model and the SST model. The heat transfer coefficient computed with the SST model is significantly lower than in the case of the $k\epsilon - realizable$, especially at the leading edge. This has a dramatic consequence on the final ice shape, because the convective and evaporative cooling are minimal; therefore, less water freezes and flows further back and consequently the icing limits are overestimated. The effect is likely to become even more evident at increasing accretion time, therefore ensuring that the turbulence model employed to compute the heat transfer coefficient is accurate is extremely important.

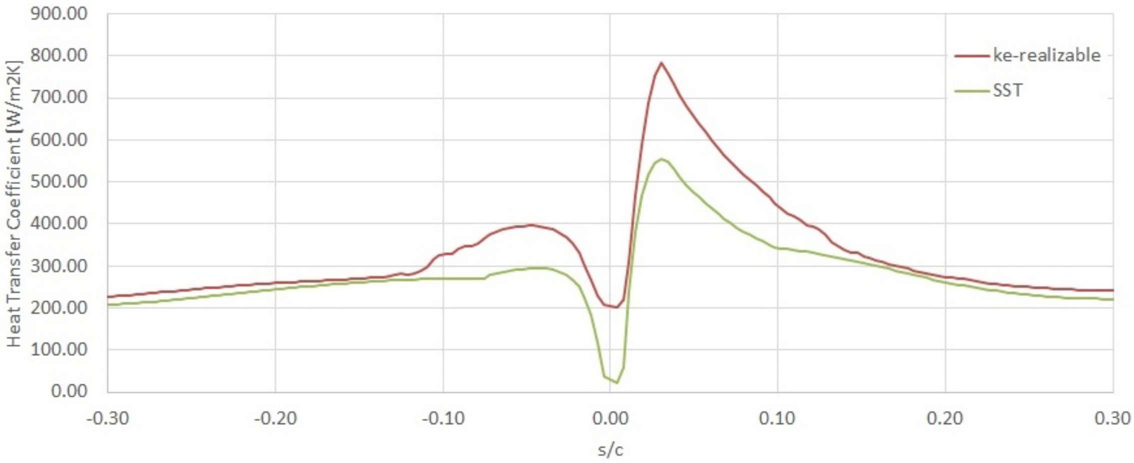

Figure 3.27: Heat transfer coefficient computed with $k\epsilon - realizable$ and SST model.

The accuracy of the turbulence models has been verified with flight and experimental data for a NACA 0012 airfoil, available in a report by NASA[12]. In the paper the Frossling number, computed with equation (3.2), was used to compare the heat transfer coefficient, and therefore it has also been computed in Fluent for uniformity.

$$Fr = \frac{Nu}{Re^{0.5}} = \frac{\frac{Hc\,c}{k}}{\frac{\rho\,V_\infty}{\mu}^{0.5}} \tag{3.2}$$

In figure 3.30 the Frossling number for a smooth NACA0012 airfoil, computed in flight and in wind tunnel, is compared with Fluent, using the $k\omega - SST$ and SST turbulence model. Although both models show good agreement, the Frossling number computed with the SST model is more accurate especially further away from the leading edge.

Beside the results for a smooth NACA 0012, in [12] also measurement for a roughened airfoil were presented. The surface roughness was simulated with hemispheres placed on the surface of the airfoil, an example of which is visible in figure 3.20 and 3.19. Because of the good agreement between SST and experimental data, it was expected that it would still provide accurate result when including the effect of roughness. Unfortunately, it has been found that the SST model largely under predicts the value of heat transfer coefficient at the leading edge. This is visible in figure 3.31, where the surface roughness was simulated using the pattern in figure 3.19. The $k\epsilon - realizable$ and SST models are compared with experimental data, obtained at the Icing Research Tunnel, and an integral boundary layer solution, similar to what is used in LEWICE.

A value of 0.000573 m for the surface roughness was used in the integral boundary layer solution from the correlations given in (3.1), considering a velocity of 62 m/s, static temperature of 266 K and liquid water content of 0.5 g/m^3, assumed as a default value. In

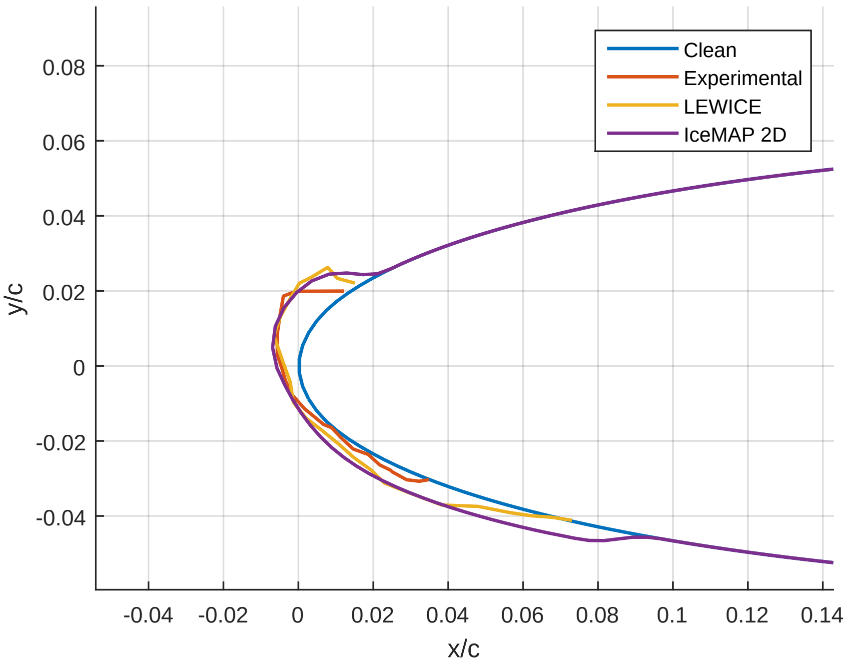

Figure 3.28: $k\epsilon - realizable$ turbulence model used to compute heat transfer coefficient.

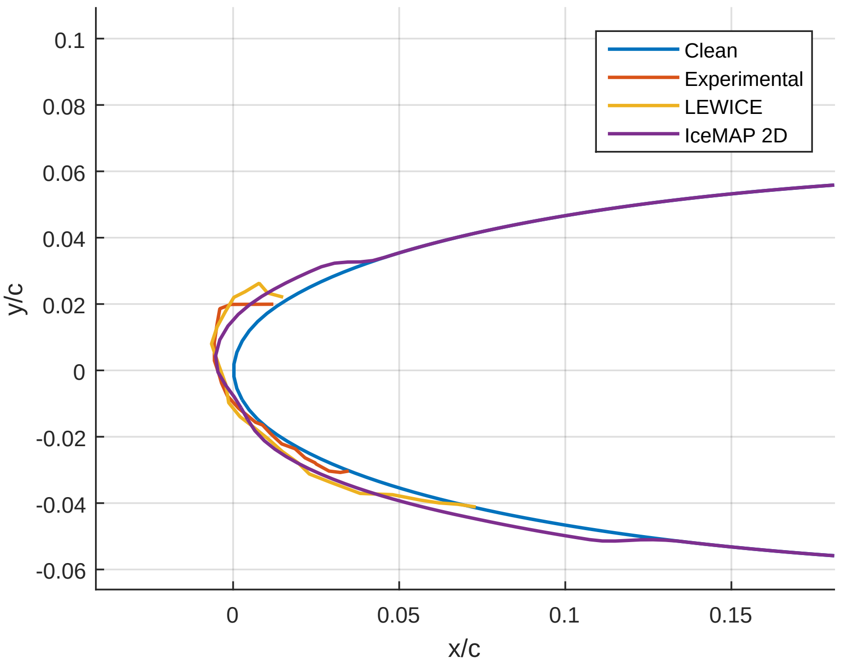

Figure 3.29: SST turbulence model used to compute heat transfer coefficient.

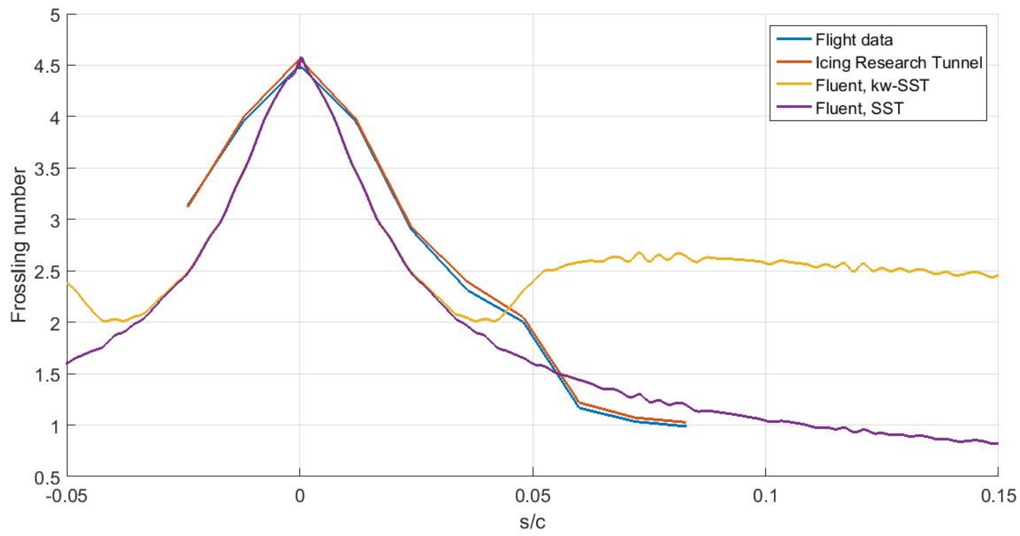

Figure 3.30: Frossling number for a smooth airfoil, flight and wind tunnel data compared with Fluent. Reynolds number approximately 1280000.

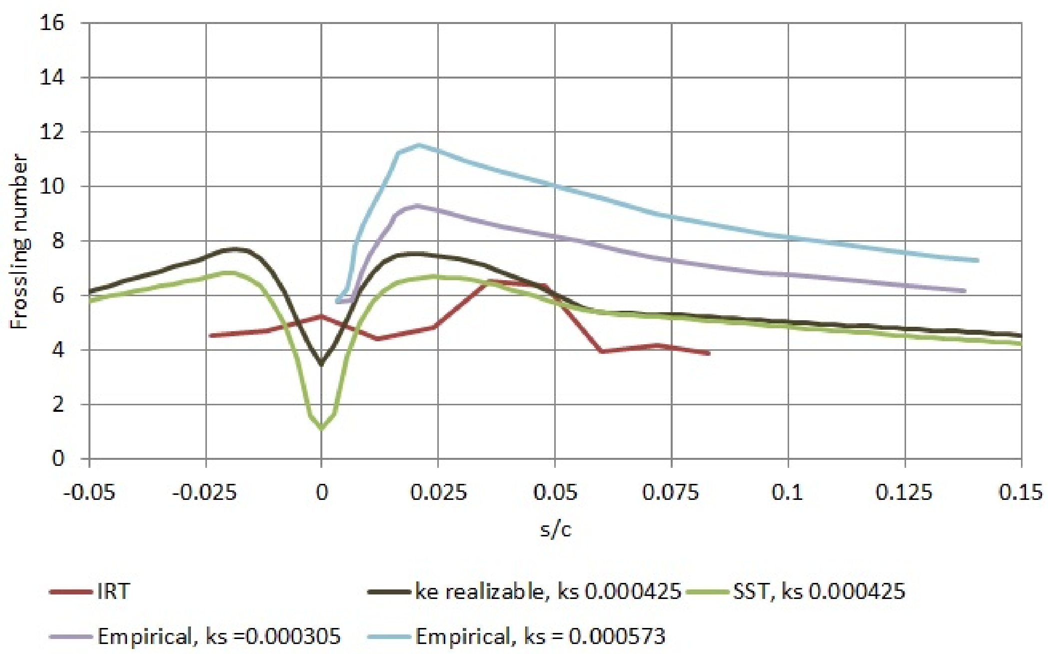

Figure 3.31: Icing Research Tunnel data compared with Fluent and integral boundary layer solution.

Schlicting[15][2] the concept of equivalent sand grain roughness was used to characterize other types of pattern, which are similar to those used in [12]; using this correlation a value of 0.000305 m for the equivalent sand grain roughness can be estimated, and was also used in an integral boundary layer solution. The Frossling number using both roughness value is visible in figure 3.31. In Fluent a single value for the surface roughness has been used, to test the differences between turbulence model. The sand grain roughness was set at 0.000452 m, as is close to the mean values used in the integral boundary layer solutions.

The integral boundary layer solution does not provide a good match of experimental data, especially in the area near the leading edge, where the heat transfer is widely overpredicted. The turbulence models used in Fluent, especially the $k\epsilon - realizable$, yields more accurate results overall. Both the $k\epsilon - realizable$ and the SST provide values comparable with experimental data further from the leading edge ($s/c > 0.03$); in the area near the leading edge the difference is larger, especially for the SST model, which largely under predicts the Frossling number, while for $k\epsilon - realizable$ is fairly close to the experimental values. Both Fluent turbulence models fare well in comparison with the integral boundary layer solution, as they both provide a more accurate heat transfer coefficient throughout.

However, it must be noted the roughness pattern employed in [12] are not exactly the same used by Schlicting, therefore the equivalent sand grain roughness value 0.000305 may be treated as an estimate. Additionally, the roughness correlation (3.1) was derived from experimental ice shapes and therefore may not yield accurate values for the roughness used in [12].

Indeed, the roughness pattern, modelled with hemispherical elements placed on the surface, does not accurately represent ice roughness, and therefore the differences may reside in a different modelling; thus the data in [12] may not be used to validate an integral boundary layer solution based on the surface roughness, as in LEWICE.

LEWICE models the heat transfer coefficient considering the effect of surface roughness, and based on the computed value of roughness determine whether the boundary layer is laminar or turbulent. The heat transfer coefficient computed in LEWICE has also been subject to some validation[14]. The results of the integral boundary layer solution were compared with experimental data on a roughened cylinder at various Reynolds number and on simulated ice accretion. The cases tested showed that the predicted values of heat transfer coefficient generally compared well with experiments in the leading edge region where much of the accretion process takes place.

Therefore the heat transfer coefficient computed in Fluent by different turbulence models has also been compared with LEWICE, which is considered to provide accurate values of heat transfer coefficient and ice shape.

A comparison is shown in figure 3.32, using for both LEWICE and Fluent the same surface roughness. The turbulence models used are $k\omega - SST$, $k\epsilon - realizable$ and SST.

The heat transfer coefficient computed by different turbulence model in Fluent are almost identical far from the leading edge, and the result can probably be considered accurate; indeed, also in the wind tunnel the integral boundary layer solution over predicted the Frossling number far from the leading edge, in an area where no roughness elements were present, while values computed in Fluent were relatively close. At the leading edge, instead, the difference is larger, with the $k\epsilon - realizable$ computing a heat transfer coefficient similar to LEWICE and the other turbulence models under predicting

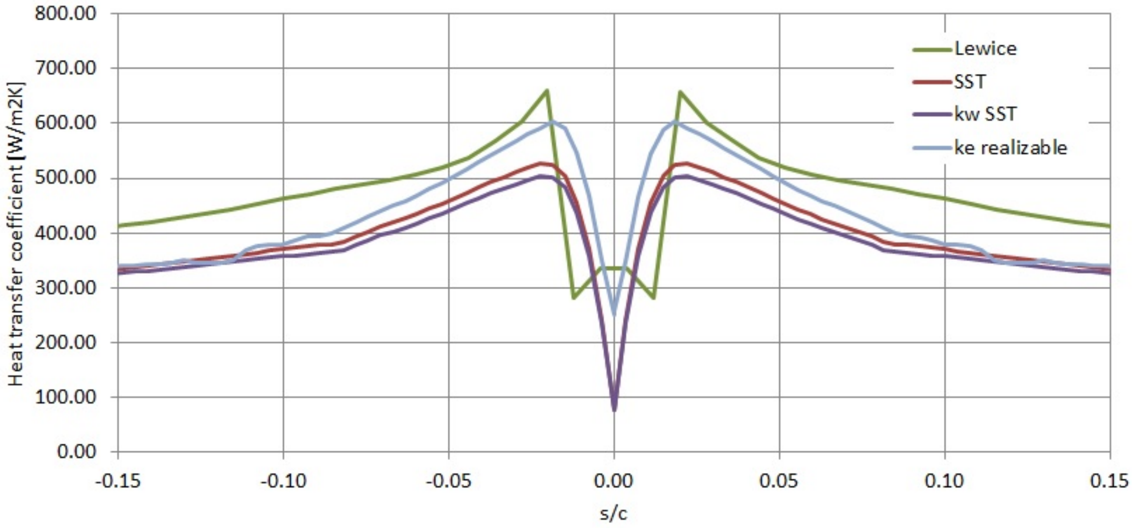

Figure 3.32: Heat transfer coefficient computed with different turbulence model and compared with LEWICE.

it.

A similar trend is also visible when comparing Fluent with wind tunnel data, where $k\epsilon - realizable$ shows generally better agreement with experimental near the leading edge. Because most of the ice accrues in the leading edge region a proper modelling of the heat transfer coefficient in that area is necessary. Therefore the $k\epsilon - realizable$ was used to compute the heat transfer coefficient, which is subsequently utilized in the solution of the thermodynamic balance.

3.3.3 Thermal boundary conditions

Ideally, the heat transfer coefficient would be computed setting as a boundary condition on the airfoil the appropriate surface temperature. In Fluent, though, it results in the computation of unrealistic values when the surface temperature is close to the external temperature, as in figure 3.33, where the surface temperature is given in 3.34. In this test case the free stream temperature was 254.15 K (total temperature $\approx$ 256 K).

As can be seen the heat transfer coefficient has some peaks where the surface temperature reaches a minimum, and then remains negative for the rest of the airfoil. This will result in a heat flux from the colder surface to the warmer surface, which violates the principles of thermodynamics, and therefore must be considered the result of computational errors in Fluent. Fluent computes the heat transfer coefficient for each wall face using the convective heat flux at the boundary and the surface and free stream temperature using equation (3.3). The heat flux is computed by Fluent in the solution process, while the surface temperature is equal to the temperature of the airfoil.

$$Hc = \frac{q_c}{T_{surf} - T_\infty} \tag{3.3}$$

Numerical errors may be the result of surface temperature close to the free stream temperature, as the denominator approaches zero. This is not acceptable, because the value

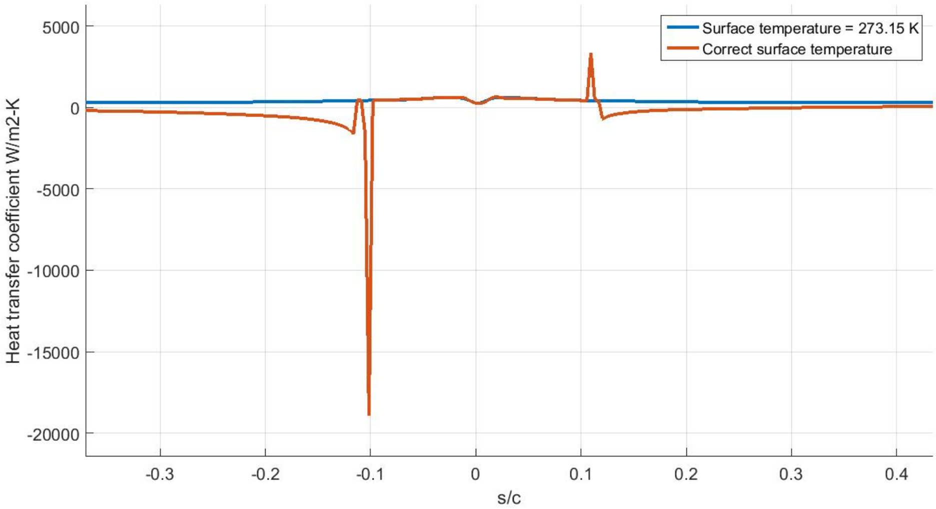

Figure 3.33: Heat transfer coefficient computed with fixed surface temperature and correct temperature distribution. Free stream temperature 254.15 K.

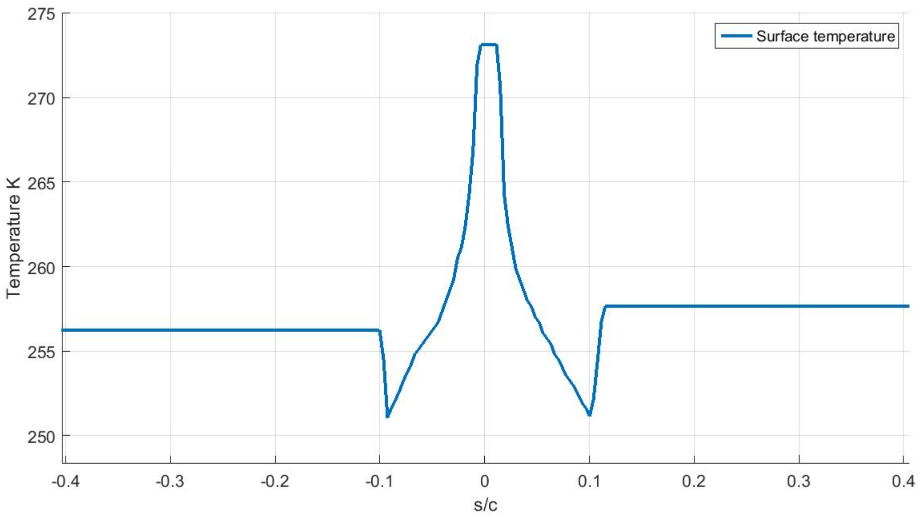

Figure 3.34: Temperature distribution on the surface of the airfoil. Free stream temperature 254.15 K.

of heat transfer coefficient is needed independently of the surface temperature to compute the heat fluxes to and from the airfoil; therefore the thermal boundary conditions in Fluent must be set up so that a realistic value for the heat transfer coefficient is computed. The heat transfer coefficient depends on the geometry of the airfoil, the physical properties of the fluid, and the characteristics of the fluid flow; although the fluid flow is influenced by the energy flux, it may be neglected if the boundary conditions applied on the surface are not significantly different from the actual surface temperature. Thus the effects of varying the thermal boundary conditions have been investigated, so that a boundary condition resulting in an acceptable heat transfer coefficient could be selected and used in all cases.

The boundary conditions tested are a fixed heat flux and a fixed temperature on the surface. Different values of heat flux and temperature have been used to verify the repeatability of the data obtained. Because in Fluent the heat transfer coefficient is a derived quantity, a heat flux must always be present, otherwise also the heat transfer coefficient in zero. Therefore the airfoil can not be considered adiabatic.

Figure from 3.35 to 3.39 compare the heat transfer coefficient computed using different boundary conditions on a NACA 0012 airfoil at 67.1 m/s, freestream temperature of 262.15 K and at different angles of attack. In figure 3.35 and 3.36 a fixed heat flux is applied on the surface to compute the heat transfer coefficient; at zero angle of attack also the heat transfer coefficient from LEWICE is plotted. Clearly, using too low a heat flux (1000 $W/(m^2\,K)$) does not reproduce correctly the trend visible in LEWICE, while increasing the heat flux results in more consistent result, also comparable with LEWICE. When the angle of attack is set at 4 degrees, the lower heat flux again under estimates the heat transfer coefficient when compared with the other heat fluxes applied. With respect to the case at 0 degree, a larger variability exists in the coefficient between the 10000 and 50000 $W/(m^2\,K)$ heat fluxes, but results are still comparable; additionally, the variability is mostly far from the leading edge, which is the area more subject to icing. It must also be noted that imposing too high a heat flux results in a significant raise in the temperature on the surface of the airfoil, which may exceed 300 K (figure 3.37); therefore, also the effect of the temperature on the heat transfer coefficient may not be negligible, and caution must be exerted in order to prevent it. On the opposite, small heat flux are not sufficient to compute accurately the heat transfer coefficient and therefore can not be considered. The heat flux applied therefore should be in a limited range, so that an accurate coefficient can be computed without altering the flow near the airfoil.

In figure 3.38 and 3.39 a fixed temperature is used instead as a boundary condition on the airfoil. The values used are 273.15 and 283.15 K; the lower value is equal to the temperature of the water film on the surface, and in case of icing at temperature close to freezing it may be close to the free stream temperature; as a consequence the problems previously discussed may still occur. Therefore a second higher value (283.15 K) has been used to verify the results; because no icing occur at temperature that high it should not be encountered in icing simulation and should prevent the denominator of (3.3) from becoming zero.

At zero angle of attack the heat transfer coefficient is comparable with LEWICE in both cases and with the fixed heat flux boundary condition. Also at the higher angle of attack there is good agreement between the two boundary conditions, with less variability compared with the fixed heat flux. Indeed, compared with the fixed heat flux condition

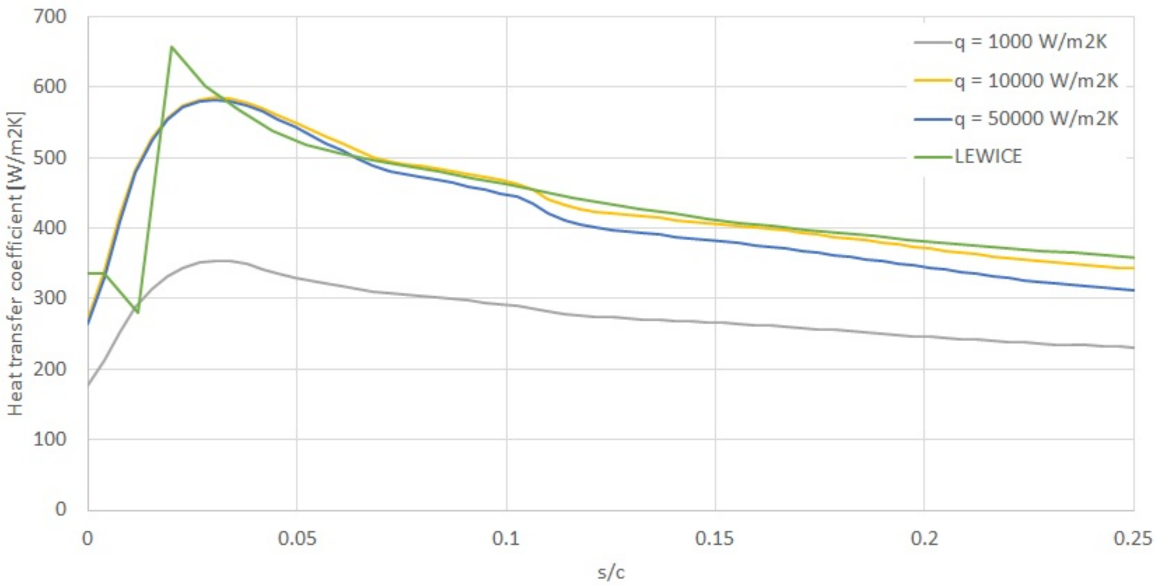

Figure 3.35: Fixed heat flux used to compute htc, AoA = 0°.

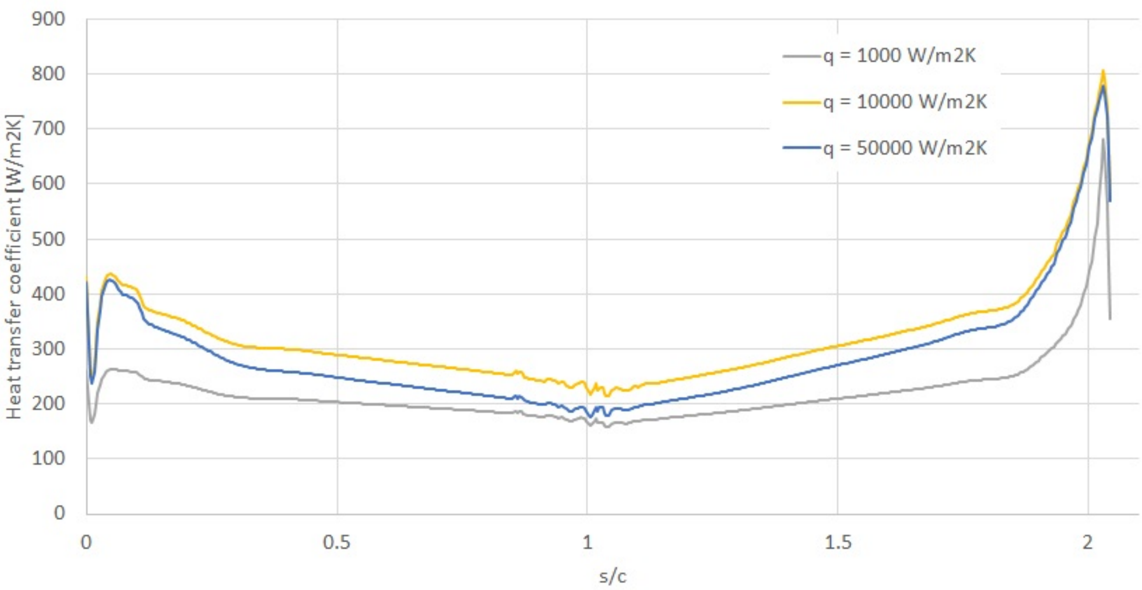

Figure 3.36: Fixed heat flux used to compute htc, AoA = 4°.

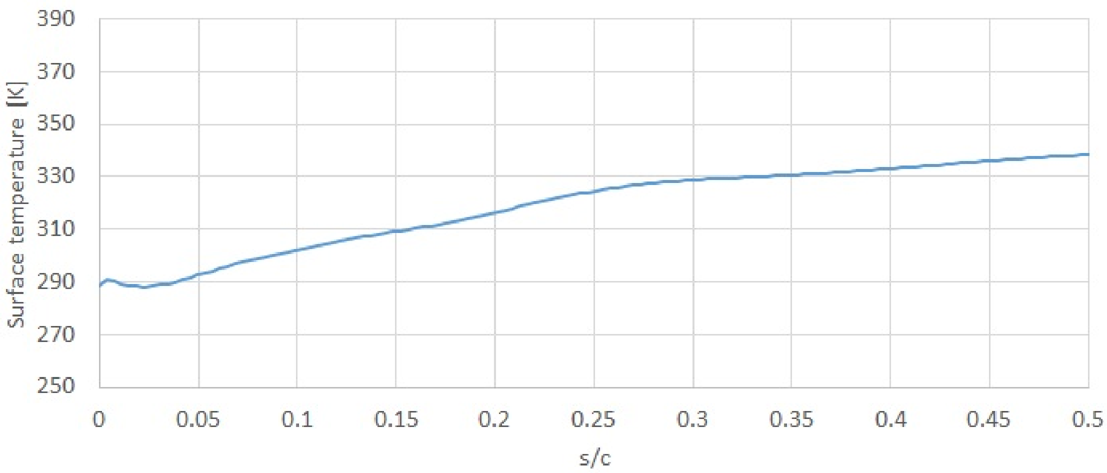

Figure 3.37: Surface temperature near the leading of a NACA 0012 airfoil; heat flux 50000 $W/(m^2\,K)$, AoA = 0 °.

the heat transfer coefficient is less influenced by the difference in the surface temperature.

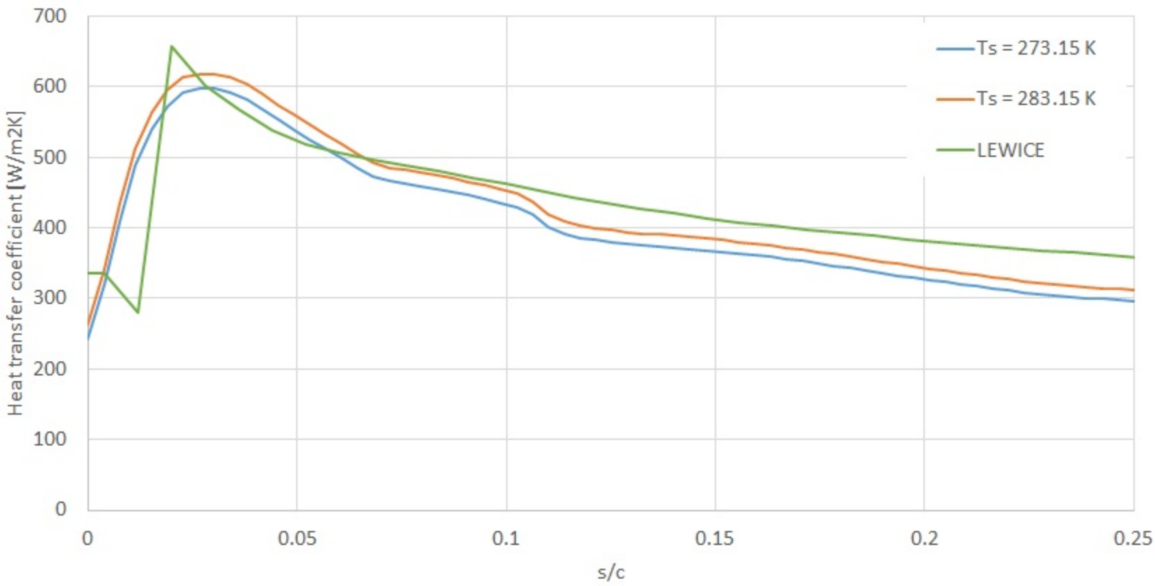

Figure 3.38: Fixed surface temperature used to compute htc, AoA = 0°.

When using a fixed heat flux as a boundary condition the surface temperature can still be expected to be higher that in the case of fixed temperature; additionally, a larger variability can be expected, because the influence on the boundary layer due to the surface temperature is higher. Therefore the heat transfer coefficient is computed using a fixed temperature of 283.15 K as a condition on the surface. In figure 3.40 the heat transfer coefficient is computed at the same external condition as in 3.38, except that the free stream temperature has been increased to 270 K from its previous value of 262.15 K. Therefore also the heat transfer coefficient should not be altered significantly, and the

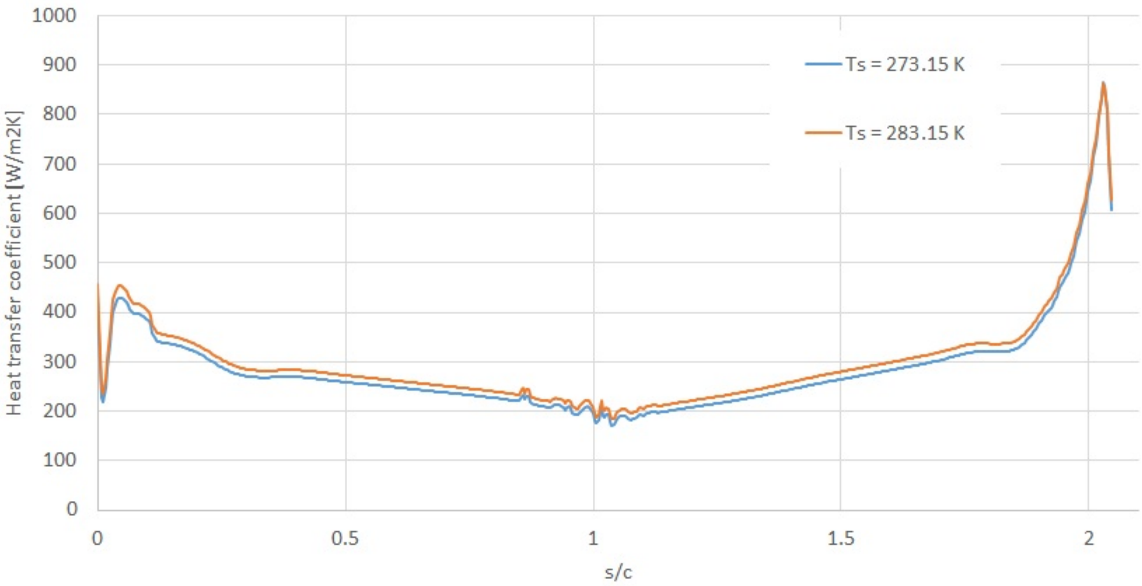

Figure 3.39: Fixed surface temperature used to compute htc, AoA = 4°.

values computed in LEWICE can still be considered accurate. This is also verified imposing the higher surface temperature, as the heat transfer coefficient is almost identical in figure 3.40 and 3.38; on the contrary, using the lower surface temperature (273.15 K) as a boundary condition the computed value is almost half of its original value, that can only be explained considering the effect of numerical errors.

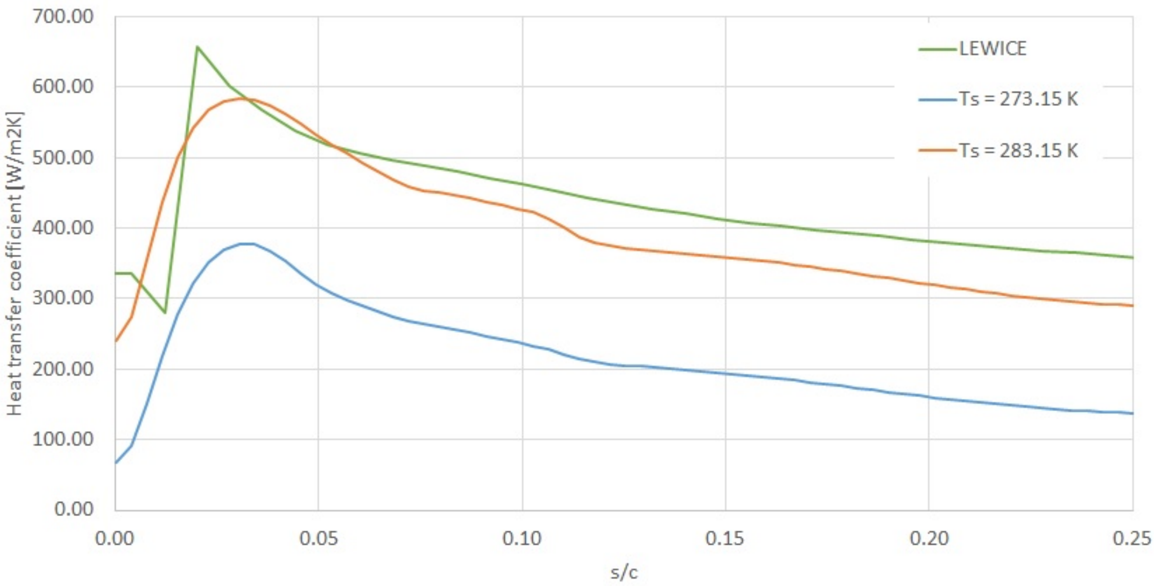

Figure 3.40: Fixed surface temperature used to compute heat transfer coefficient, $T_\infty = 270\ K$.

3.4 Flow field computation

The fluid flow in the domain is solved in Fluent at every time step, considering the boundary conditions applied and the settings used. The boundary conditions specify the flow and thermal variables on the boundaries of the model, thus they are a critical component of the simulation.

The pressure far field condition is used in Fluent to model a free stream condition at infinity, and is used for the external boundary of the domain. The free stream Mach number, static temperature and pressure and flow direction are specified, considering the ambient condition specified by the user.

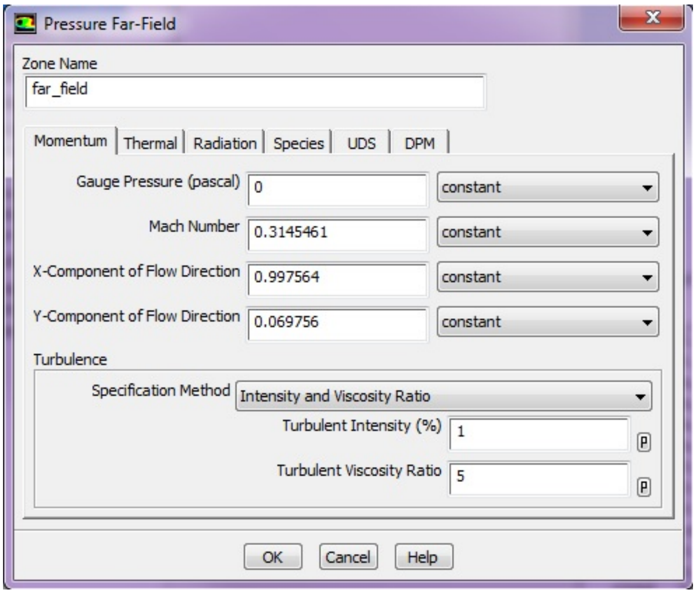

Figure 3.41: Example of pressure far field settings in Fluent.

The wall boundary condition is used to define the fluid/solid interface, thus is applied for the airfoil. The surface temperature, as defined in 2.4.1, and the equivalent sand grain roughness, computed with (3.1), are set for the airfoil. Additionally, the velocity on the airfoil is automatically set to zero for viscous flow to enforce the no-slip condition.

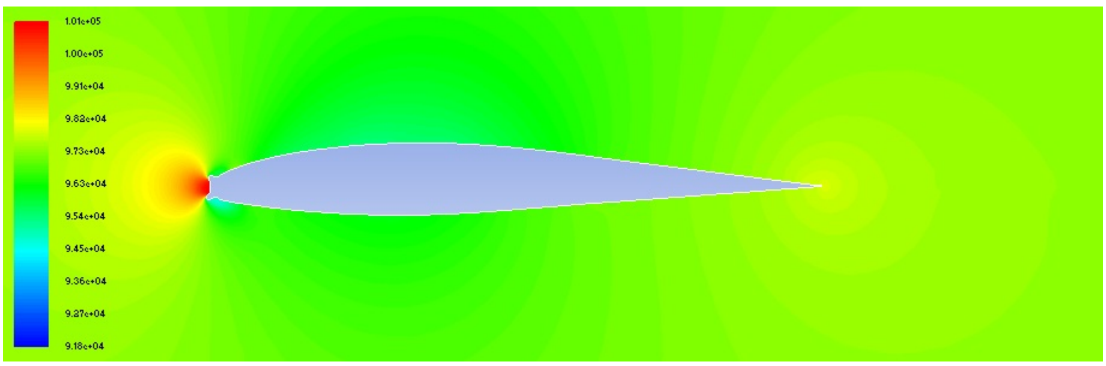

Figure 3.42: Pressure field around a 22.5 minutes ice shape on the Twin Otter tail; angle of attack 0°, free stream velocity 90 m/s, pressure 97216 Pa.

Compressibility effects are encountered in flows at high velocity and in area of large pressure variation. In the case of ice accretion large pressure gradient may be encountered, and the variation of gas density may have a significant impact on the flow velocity and temperature. Additionally, compressibility effects are also important at high Mach, thus the compressibility effect have been included to ensure a larger range of validity for the flow solution. Therefore, air is considered an ideal gas and its density at a given location is computed according to equation (3.4).

$$\rho = \frac{p_{op} + p}{\bar{R}T} \tag{3.4}$$

The viscosity of the fluid under consideration also has an impact on the heat transfer; therefore, the viscosity of the air is considered as a function of temperature and modelled using Sutherland's viscosity law, which resulted from a kinetic theory by Sutherland using an idealized intermolecular-force potential. Sutherland's law with three coefficients has the following form:

$$\mu = \mu_{ref} \left(\frac{T}{T_{ref}} \right)^{\frac{3}{2}} \frac{T_{ref} + S}{T + S} \tag{3.5}$$

Where the reference conditions are:

$$\mu_{ref} = 1.716 \cdot 10^{-5} \tag{3.6}$$

$$T_{ref} = 273.11 \tag{3.7}$$

$$S = 110.56 \tag{3.8}$$

The fluid flow is then solved using the $k\omega - SST$ (Shear Stress Transport) equation, based on the Reynolds Averaged Equations, which is one of the most widely used models for aerodynamic flows. Compared to $k\epsilon$ the $k\omega$ models are typically better in predicting adverse pressure gradient boundary layer flows and separation. The downside is a strong sensitivity of the solution depending on the free stream values of turbulence. The $k\omega - SST$ has been designed to avoid the free stream sensitivity of the standard $k\omega$, by combining elements of $k\omega$ with $k\epsilon$ model; boundary layer is modelled as in $k\omega$, while in the far field region, where $k\omega$ is most sensible to turbulence, like the $k\epsilon$.

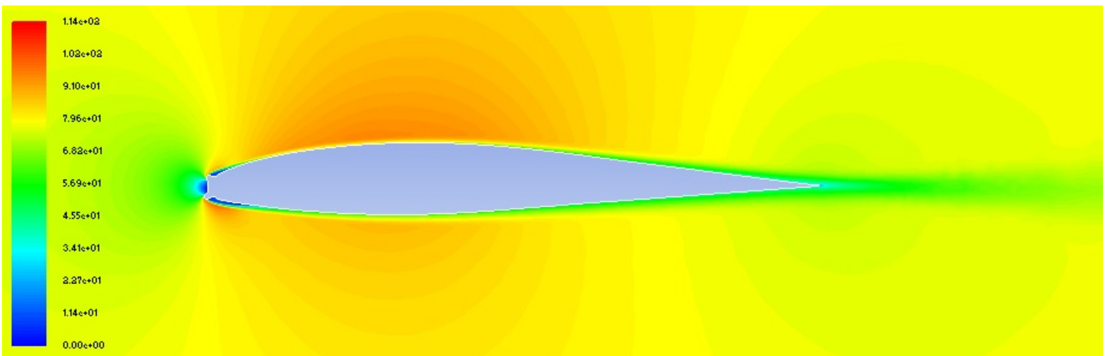

Figure 3.43: Velocity flow field around a 22.5 minutes ice shape on the Twin Otter tail; angle of attack 0°, free stream velocity 90 m/s, pressure 97216 Pa.

The accuracy of the model and the mesh used in the ice accretion process has been tested by comparing the pressure coefficient on the surface with experimental and analytical data for both clean iced airfoil. The data used to verify the Fluent solution is available in [11], and has been obtained at different wind tunnel and using LEWICE potential flow solution.

A clean GLC 305 and a clean and simulated ice shape on an aircraft (Twin Otter) tail have been used. Figure 3.46 shows the result for the clean GLC305. In figure 3.44 and 3.45 the coefficient of pressure is computed for clean and a 22.5 minutes ice accretion on the horizontal tail section of the Twin Otter. In all of cases the Fluent solution provides excellent agreement with experimental data, including for the iced airfoil.

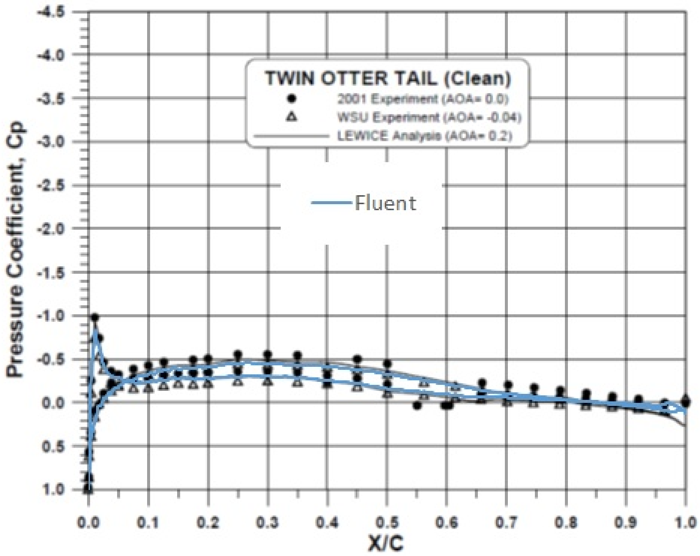

Figure 3.44: Coefficient of pressure on the Twin Otter horizontal tail; angle of attack 0°, free stream velocity 78.23 m/s, pressure 99974 Pa.

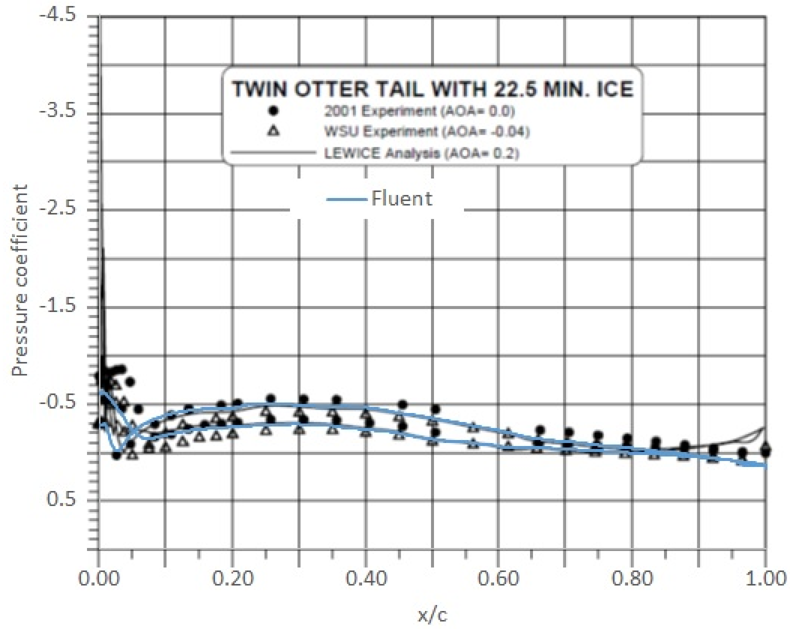

Figure 3.45: Coefficient of pressure on a simulated 22.5 minutes ice shape on the Twin Otter horizontal tail; angle of attack 0°, free stream velocity 90 m/s, pressure 97216 Pa.

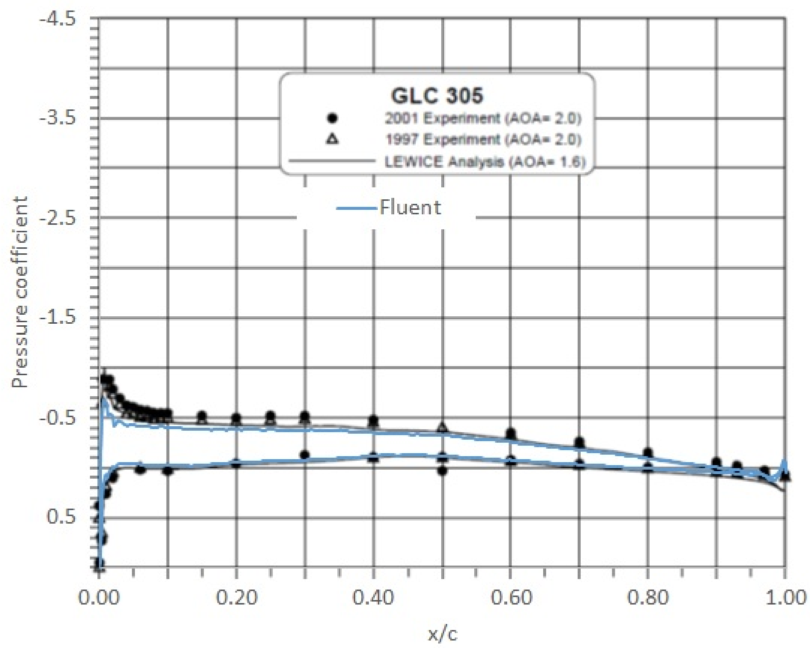

Figure 3.46: Coefficient of pressure on a clean GLC 305 airfoil; angle of attack 1.5°, free stream velocity 78.23 m/s, pressure 98732 Pa.

3.5 Particle tracking

The purpose of the discrete phase model is to determine the distribution of impinging water on the airfoil and to compute the variables associated with impinging particles necessary to compute the growth of ice on the surface. In Fluent a second phase, composed of spherical droplets dispersed in the air, can be simulated in a Lagrangian frame of reference activating the Discrete Phase Model available. Fluent computes the trajectories of particles as well as the heat and momentum exchange with the continuous phase, that affect both the particles and the surrounding air. Because the influence of droplets on the airflow is marginal, an aerodynamic solution is first computed, and then particle trajectories are simulated. The trajectories and heat and momentum transfer calculation are based on the force balance and the convective heat transfer, defined in section 2.3, using the local conditions of the continuous phase.

3.5.1 Particle initialization

The number of water particles that should be tracked at each iteration can be computed from the mean volume diameter and the liquid water content. This is given by equation (3.9), in which the liquid water content is divided by the mass of a single particle.

$$n_p = \frac{6LWC}{\pi MVD^3 \rho_p} \tag{3.9}$$

With a droplets size of 20 μm and a liquid water content of 0.5 g/m^3 the number of particles in a cubic metre of air is close to 400 millions. This is a prohibitive number of particle to be tracked, and therefore in Fluent a number of parcels, each representative of a fraction of the total mass flow rate, is tracked. A parcel can still be considered as representative of a single particle, as it has the specified diameter and specified properties of a single droplet. However, the effect on the continuous phase are computed by summing the effect of all the particles represented by the parcel.

Therefore, the particles are simulated launching a group of particles in the domain, for which is necessary to define the initial conditions. With these conditions, along with physical properties defined choosing an appropriate material, the computations of the trajectories and energy/mass transfer can be initiated. The inputs required are:

- Material.
- Position.
- Velocity.
- Temperature.
- Diameter.
- Flow rate.

Selecting as material liquid water the physical properties necessary to compute the particle trajectory and heat transfer are automatically defined. The initial position must be far enough from the airfoil that the flow is not influenced by the airfoil, and is required as

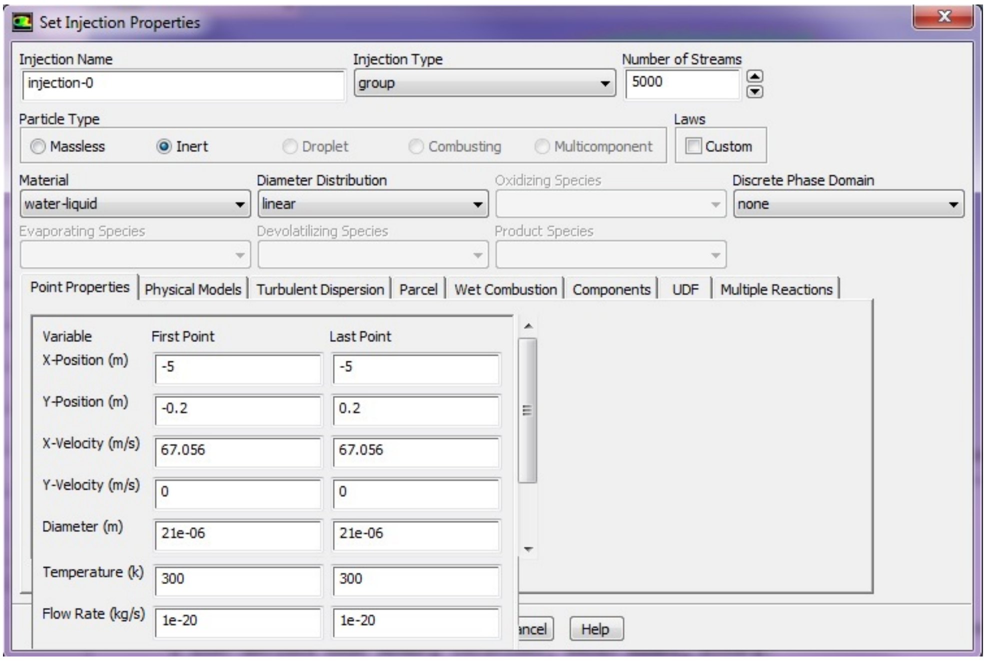

Figure 3.47: List of particle properties. These are set using a UDF.

an user input. The particles velocity and temperature are set equal to the velocity of air at the same location, as computed by Fluent solving the continuous phase. Indeed, when particles are far from the airfoil, they can be considered in equilibrium with the continuous phase, and hence the settings used are appropriate. The diameter is constant and equal to the median volumetric diameter of the icing conditions. Finally the mass flow rate associated with each parcel is computed using the local air velocity and liquid water content, using equation (3.10); additionally, the launch coordinates and the number of parcels is used.

$$\dot{m} = (LWC)V\frac{y_{max} - y_{min}}{n_p} \tag{3.10}$$

The inputs are automatically computed in a user defined function, which is responsible of defining the appropriate variables.

3.5.2 Collection efficiency

After computing the particle trajectories the collection efficiency can be computed for each face of the mesh. For this reason in IceMAP 2D the collection efficiency is obtained using equation (3.11), in which the collection efficiency is defined as the ratio of impinging droplets to the number of particles in the corresponding freestream area.

$$\beta_i = \frac{dy_0}{\frac{face\ area_i}{number\ of\ impacts_i}} \tag{3.11}$$

$$dy_0 = \frac{y_{max} - y_{min}}{number\ of\ particles\ launched} \tag{3.12}$$

In (3.11) dy_0 is the distance in the launch position of two particles. When a particle hits a face of the airfoil it is removed from the flow field and Fluent stop tracking it. For every segment impinged a set of data (number of particle impacts, mass flow rate, particle temperature, velocity) is collected and stored. The number of particle impacts and initial position are immediately used to compute the local collection efficiency, while the mass flow rate, impact velocity and impact temperature are later used in the ice accretion module.

The local collection efficiency obtained gives informations on which area of the surface are more exposed to droplet impacts and therefore more subject to icing. A proper modelling of impingement is necessary for accurate icing simulation, and therefore the results obtained in Fluent have been verified with LEWICE and experimental data from the Icing Research Tunnel, IRT, published in [11]. LEWICE is an icing software developed by NASA, whose results, including collection efficiency, have been validated through a large number of test cases. The Icing Research Tunnel is a facility operated by NASA to simulate in a wind tunnel icing conditions and is therefore capable of visually tracking particles and their impact position.

In [11] collection efficiency data were obtained for four different airfoils and two simulated ice shapes on the Twin Otter tail. The airfoils used were MS(1)–0317, GLC305, NACA 652–415 and the Twin Otter horizontal tail section, and the two simulated ice shapes were 22.5 and 45 minutes ice shape on the Twin Otter tail as computed in LEWICE. Collection efficiency was computed for droplets diameter ranging from 11 μm to 168 μm for different angles of attack.

To verify the result, two airfoil and a simulated ice shape have been considered; the airfoil used are the GLC 305 and the Twin Otter tail, and a 22.5 minutes simulated ice accretion on the Twin Otter tail. In Fluent only smaller droplet size (up to 79 μm) have been used, because at larger diameter other factors, which are not modelled, influence the droplets impingement. Large droplets are indeed subject to splashing and breakup, which are the result of the different regimes that a droplet can encounter in a region with high pressure gradients, such as in the boundary layer near an airfoil. In [11] it was found that droplet splashing and breakup has a significant impact on the collection efficiency and subsequently on the final ice shape, but it mainly affect larger droplets. For the range of size typical of ice accretion though these effect can be safely neglected without impacting the collection efficiency results. Larger droplets than those simulated are possible, but they are rarely encountered, especially for helicopter operations, and therefore it is not considered a limitation of IceMAP 2D.

Test conditions are reported in table 3.5.2, while comparison of results is visible in figure 3.48 to figure 3.54. Collection efficiency computed by Fluent is comparable to experimental data for the smaller droplet size used (11 to 21 μm) for all airfoil, including the simulated ice shape. As expected, larger differences exist for 79 μm droplet diameter, but the result is still acceptable; this is caused by droplet breakup prior to impact and droplet splashing effect, which start to become important factors in the modelling of particles.

Airfoil	**chord** $[m]$	V_∞ $[m/s]$	**AOA**	**MVD** $[\mu m]$	**Figure**
GLC305	0.9114	78.25	1.5	11	3.48
GLC305	0.9114	78.25	1.5	21	3.49
TwinOtter horizontal tail	1.448	78.25	0	11	3.51
TwinOtter horizontal tail	1.448	78.25	0	21	3.51
TwinOtter horizontal tail, 22.5min ice shape	1.448	78.25	0	11	3.52
TwinOtter horizontal tail, 22.5min ice shape	1.448	78.25	0	21	3.53
TwinOtter horizontal tail, 22.5min ice shape	1.448	78.25	0	79	3.54

Table 3.1: Test cases conditions.

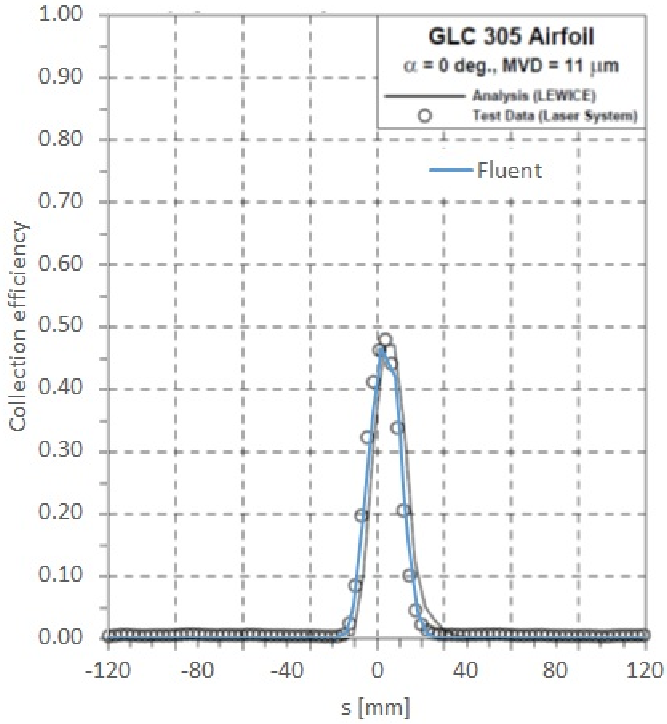

Figure 3.48: GLC305 collection efficiency for 11 μm MVD.

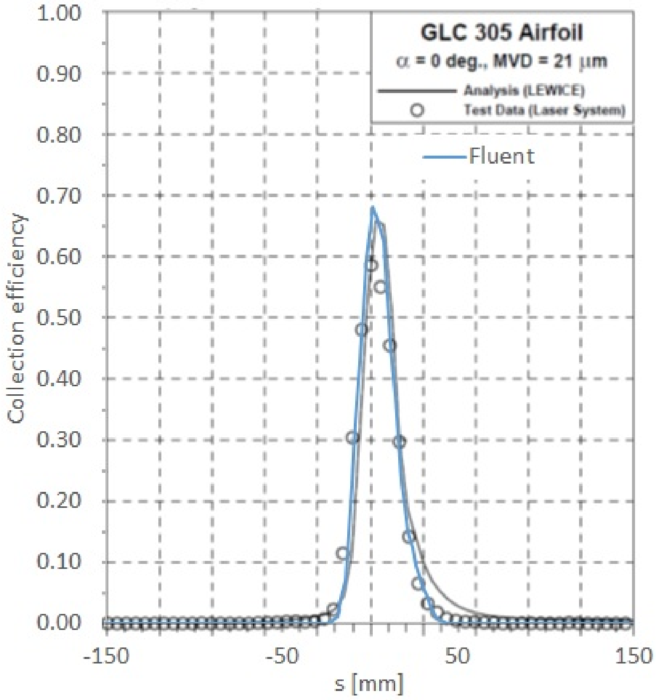

Figure 3.49: GLC305 collection efficiency for 21 μm MVD.

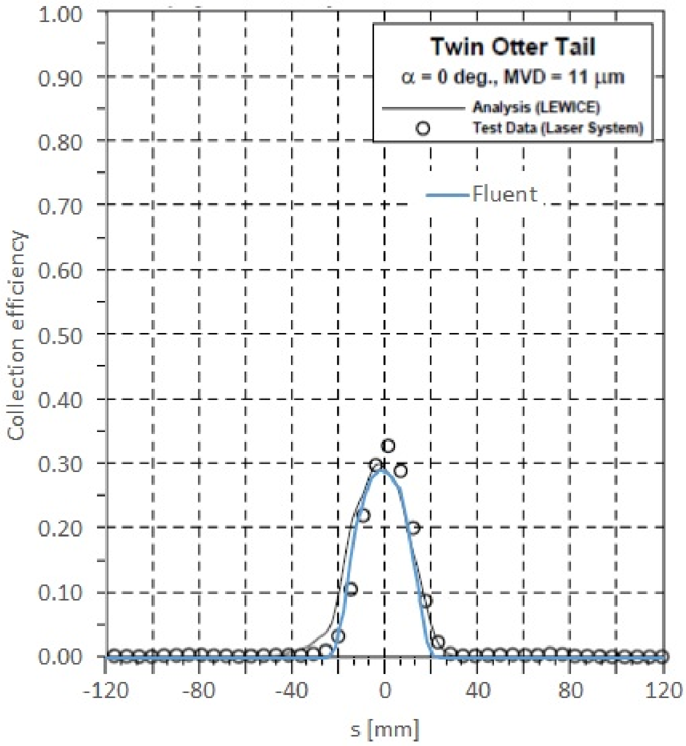

Figure 3.50: Collection efficiency for 11 μm MVD on the Twin Otter horizontal tail section.

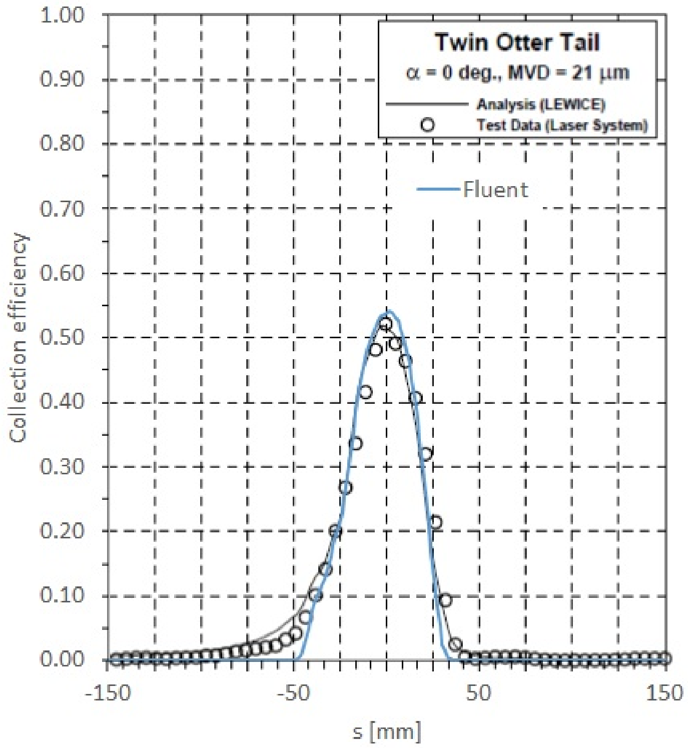

Figure 3.51: Collection efficiency for 21 μm MVD on the Twin Otter horizontal tail section.

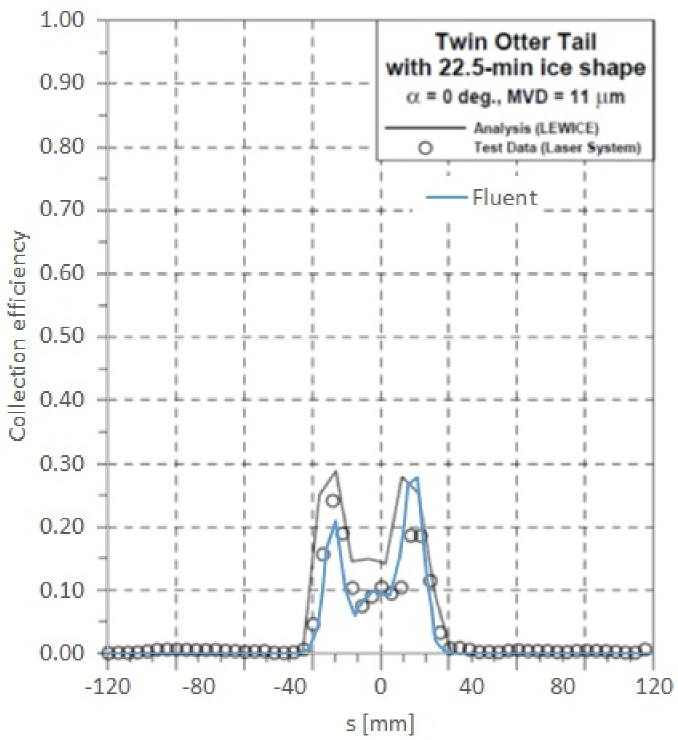

Figure 3.52: Collection efficiency for 11 μm MVD on a simulated 22.5 minutes ice shape on the Twin Otter horizontal tail section.

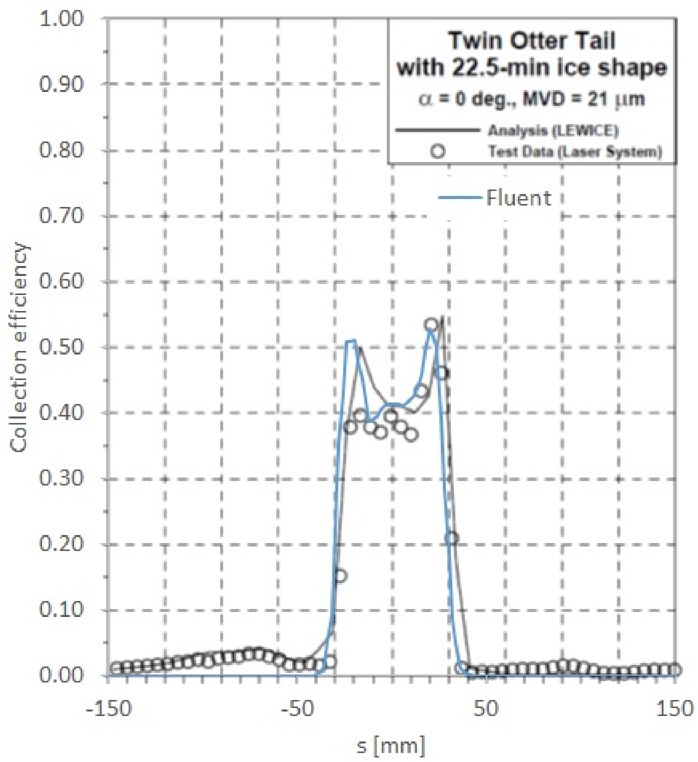

Figure 3.53: Collection efficiency for 21 μm MVD on a simulated 22.5 minutes ice shape on the Twin Otter horizontal tail section.

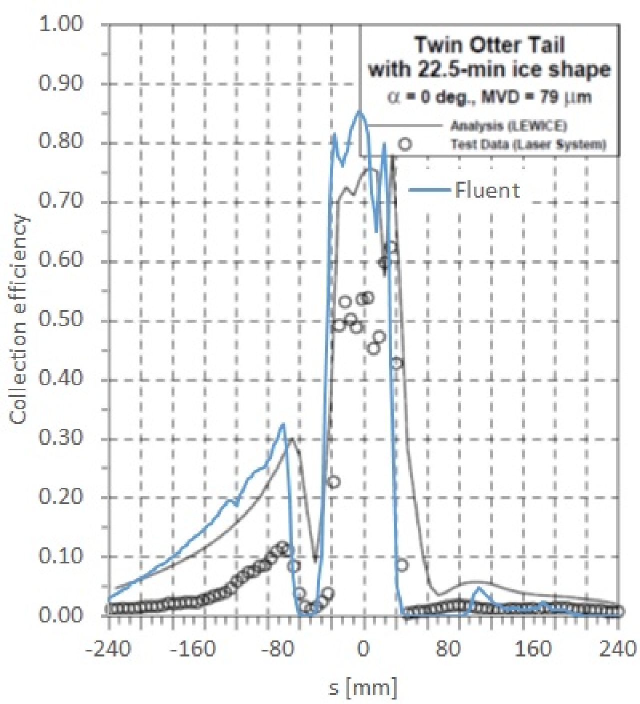

Figure 3.54: Collection efficiency for 79 μm MVD on a simulated 22.5 minutes ice shape on the Twin Otter horizontal tail section.

3.6 Thermodynamic balance

The solution of the thermodynamic balance on the surface is the core of the ice accretion simulation. Indeed, the result of its solution is the freezing fraction at each airfoil location, which translates in a local ice thickness. The solution of the balance is implemented in Fluent by means of a user defined function, because it was not possible to simulate ice accretion in Fluent. The user defined function is launched when the flow field solution has been obtained and the particle tracking module has been executed. For the first time step also the initial surface temperature has been computed, as indicated in section 2.4.1. Therefore, when the thermodynamic balance is solved, the flow variables, the heat transfer coefficient, obtained as indicated in 3.3, and the mass of impinging water, derived from the particle tracking described in 3.5, are known at each airfoil location.

The module is implemented with a udf that is executed outside the Fluent solution process, so that the variables of interest do not vary in the execution. The solution of equation (2.18) and (2.28) begins at the stagnation point, where it is assumed that there is no runback water. At each body location, defined by a mesh face, the contribute of the energy and mass terms, detailed in 2.4, is computed, and are used to determine the local freezing fraction. Using the freezing fraction and the user input of time step length the mass of water freezing at a given location is determined; consequently, with the ice density, also the local ice thickness. Also the mass flux of runback water leaving the control volume can be computed from the solution of the mass balance, using the input of freezing fraction and icing mass. Finally, the temperature on the initial surface, the ice thickness and the energy and mass terms are used to calculate the temperature on the iced surface, which is obtained considering the effect of conduction through the ice layer.

This process is then repeated for the mesh face immediately downstream, where the mass of runback water entering the volume is equal to the mass flux of runback water leaving the preceding volume. At the end of the procedure the parameters characterizing the ice accretion are therefore defined, and are subsequently used to determine the geometry of the iced surface. Thus, for each face of the mesh has been defined:

- Freezing fraction.
- Mass of freezing water.
- Ice thickness.
- Temperature on the iced surface.

Finally, the user defined function prints in external files the energy and mass fluxes used to solve the thermodynamic balance as well as the parameters derived, like the freezing fraction and the ice thickness.

3.7 Accretion algorithm

The solution of the energy and mass balance on the airfoil yields the ice thickness to be added at each location. Because the thermodynamic balance is solved in a control volume, the output thickness can be associated with the thickness at the center of the face; the mesh instead is defined by the position of nodes, therefore it is first necessary to compute the thickness to be added at each node. The node thickness is obtained by averaging the ice thickness computed at the node adjacent faces, as in equation (3.13).

$$b_{node} = \frac{b_{(i)} + b_{(i+1)}}{2} \tag{3.13}$$

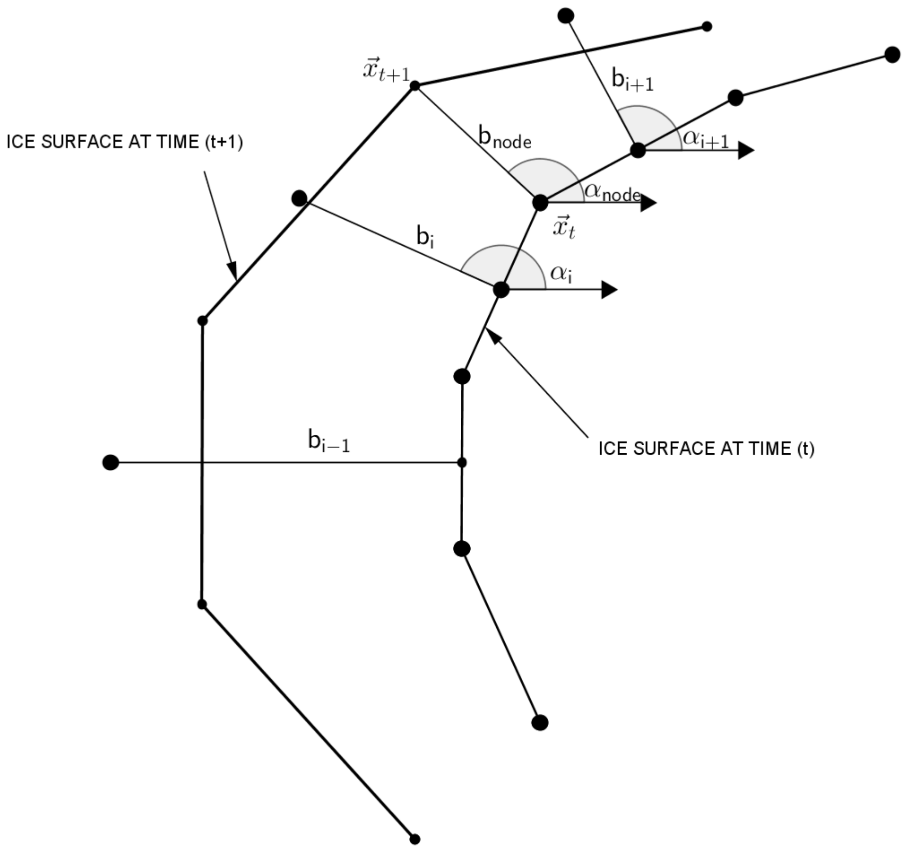

Figure 3.55: Illustration of ice accretion procedure.

The local ice thickness have to be converted in a pair of coordinates, so that the nodes position of the iced geometry can be computed. Therefore, the direction of accretion must be defined, and is obtained averaging the normals of the node adjacent face; this is given by equation (3.14), where α is the angle defining the face normal.

$$\alpha = \frac{\alpha_{(i)} + \alpha_{(i+1)}}{2} \tag{3.14}$$

Using the thickness and direction of accretion, computed with equation (3.13) and (3.14), is then possible to compute the new coordinates of each node, that is:

$$x_{t+1} = x_t + b_{node}\, cos(\alpha) \tag{3.15}$$

$$y_{t+1} = y_t + b_{node}\, sin(\alpha) \tag{3.16}$$

When the iced geometry has been computed the accretion algorithm checks that there is no intersection in the iced geometry; therefore, IceMAP 2D determines for each pair of segments, excluding the two adjacent segments, whether they intersect. If an intersection is found all of the segments between the two intersecting are removed. Figure 3.56 illustrates the procedure used: in red the calculated ice shape is intersecting in two different position, while in blue the final ice shape shows that the intersecting segments have been eliminated.

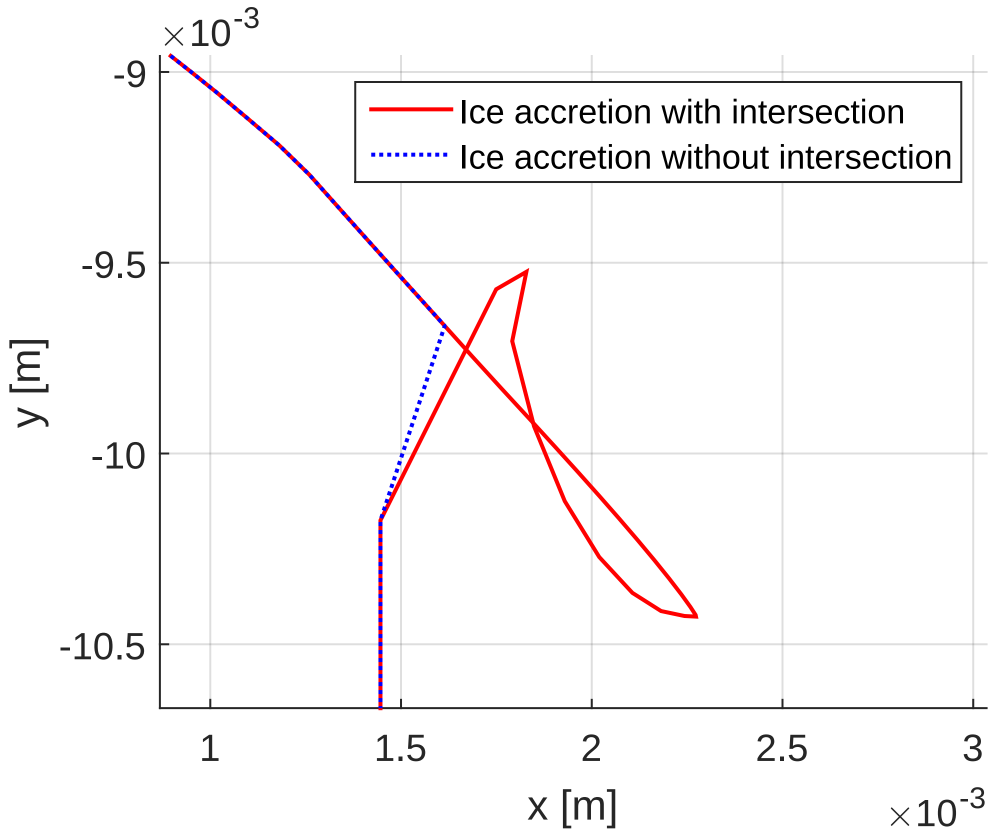

Figure 3.56: Illustration of the procedure to remove intersections.

3.8 Mesh modification and control

The dynamic mesh feature available in Fluent allows to move the nodes positions of a wall with respect to other cell zones and to adjust the mesh accordingly. The motion of the nodes is governed by a user defined function, using the coordinates computed in 3.7. This has the advantage that the flow calculation is restarted from the solution of the preceding time step; because the difference between the geometries are not excessively large, the convergence of the solution is faster than it would be reinitializing the solution. Additionally, the time required to recreate the geometry and the mesh is eliminated, because the same mesh is reused for the successive time step. Thanks to the speed of the mesh modification process and solution computation this is the preferred method to adapt the mesh to the new geometry.

The morphed mesh, though, has to satisfy certain quality requirements to ensure that Fluent can compute a flow solution properly, therefore some of the properties of the mesh are controlled. Specifically, volumes, skewness and face length on the airfoil are verified after each mesh modification. These are the parameters with more effect on the solution process, in that they can prevent Fluent from computing a proper flow solution. If these parameters are not satisfied, like in figure 3.57, the domain is remeshed, figure 3.58, with the procedure described in 3.2 which guarantees sufficient quality.

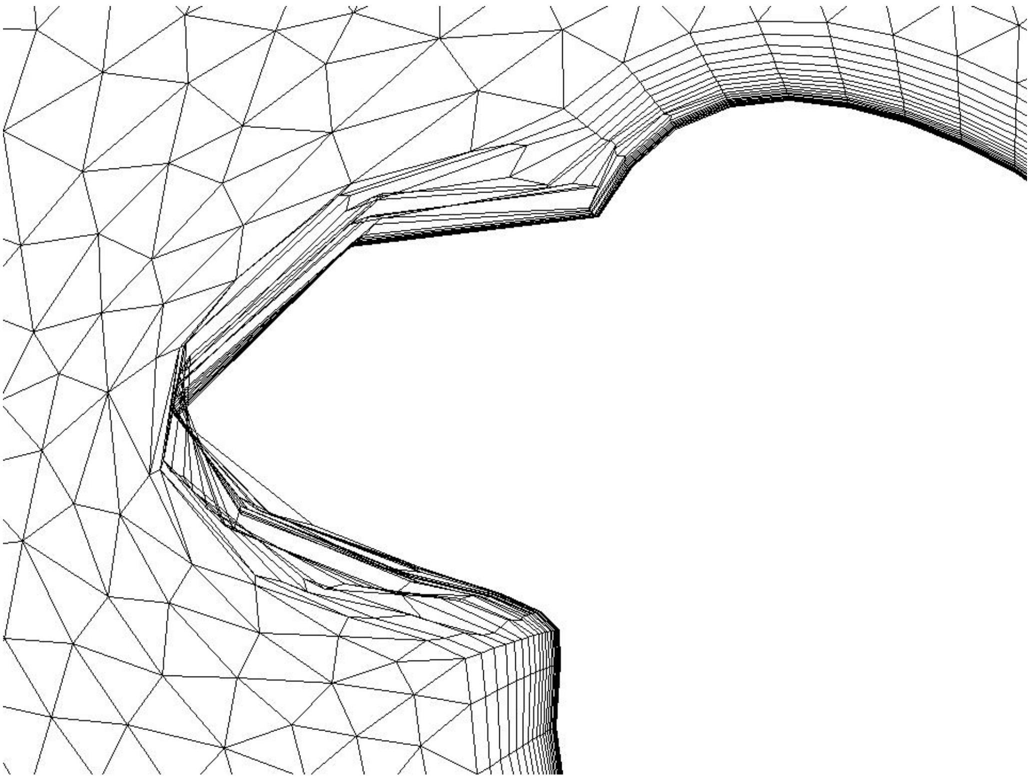

Figure 3.57: Example of mesh morphed in Fluent, with highly skewed cells and negative volumes.

A mesh containing negative volumes will lead to divergence in the solution process, and for this reason they must be eliminated. Therefore, the quality check of the mesh begins with a control on the cells volume, and if any volumes is non positive the domain

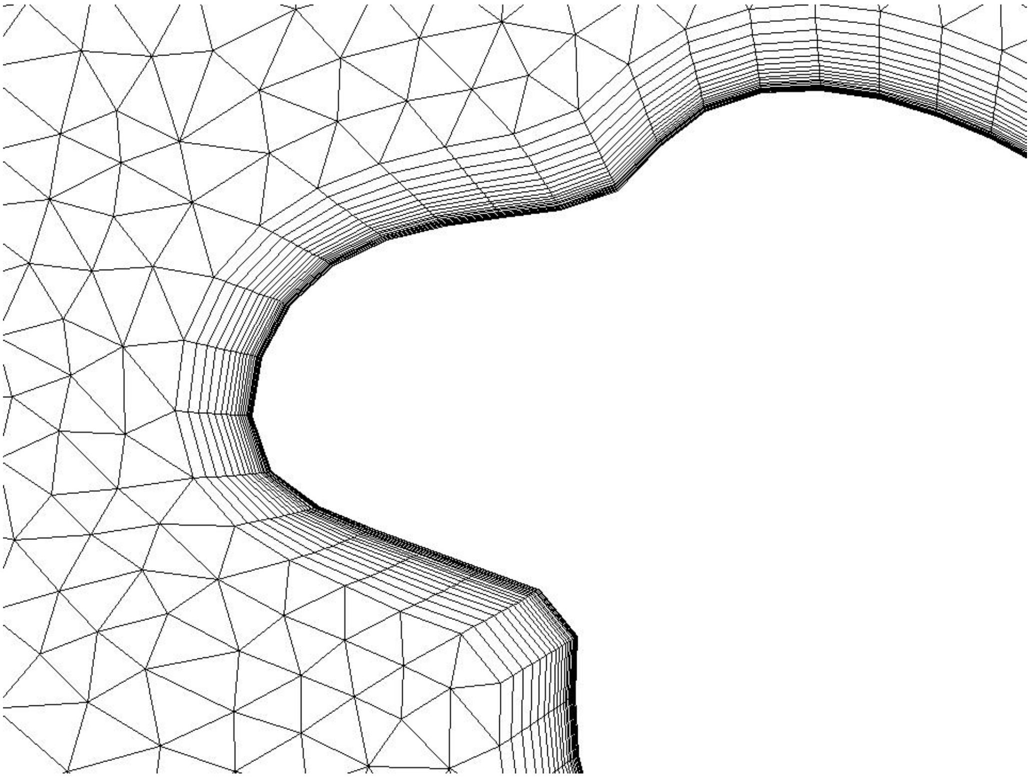

Figure 3.58: Domain remeshed, satisfying the quality requirements.

is remeshed.

Next the segments length is verified. Indeed, when ice grows on the surface the length of a segment increases, but at some point will reach an excessive length; as a consequence sufficient definition of the surface may be lost and the flow field solution may not be accurate. Therefore, the ratio between the actual length and initial face length is computed to ensure that it does not exceed a given value. This is given in (3.17), where ΔL_{max} is a user input.

$$\frac{ds_{t+\Delta t}}{ds_t} < \Delta L_{max} \tag{3.17}$$

In this case the domain is remeshed, and the surface is divided in faces of length specified in input. In the script ΔL_{max} was generally set at value between 1.5 and 2; when setting the maximum allowed elongation of faces the same principles illustrated in section 3.2.1 apply. Therefore, the maximum face length should generally not exceed a value of 2 mm, in order to ensure that the mesh is sufficiently fine at all the time steps.

Finally the mesh equiangular skewness, defined by equation (3.18), is checked.

$$skewness = max\left[\frac{\Theta_{max} - \Theta_e}{180 - \Theta_e}, \frac{\Theta_e - \Theta_{min}}{\Theta_e}\right] \tag{3.18}$$

Where Θ_e is the angle for an equiangle (ideal) cell, thus 60 degrees for triangular cells and 90 degrees for quadrilateral cell. The skewness determines how close to ideal a cell is; a value of 0 indicates an equilateral cell (best), while a value of 1 indicates a degenerate cell, which are characterized by nodes almost collinear. Highly skewed cell should be avoided because they can compromise the accuracy of the solution; a maximum value of 0.85 is generally accepted for quadrilateral cell, and triangular cells should not have skewness above 0.9. A single skewed cell does not generally alter significantly the solution, thus in IceMAP 2D a small percentage of cells is allowed skewness above a given threshold. Both the threshold skewness and the percentage of skewed cells allowable is settable by the user. In the test cases, the threshold value was set at 0.75, while the maximum percentage was 0.005%; these are also the default values in the script, and generally ensured an acceptable mesh quality.

Chapter 4

Results

The ice accretion simulation tool, IceMAP 2D, has been tested against both experimental data and test cases available in literature. The experimental ice shapes used for the comparison have been obtained at the NASA Icing Research Tunnel and are presented in [20], [19] and [17]. The analytical ice shape have been obtained from different icing software and are also reported in literature; these are LEWICE[20][19][17], which is a well validated icing software developed by NASA, TRAJICE2[19], developed by DRA, and ONERA[19]. In some cases the simulated ice shape have been computed using LewInt and [1] no experimental ice shape is available as the test conditions were not found in literature. Therefore, in the chapter with ice shapes and discussions is indicated whether LEWICE, and thus data from literature, or LewInt is used.

Four different airfoils have been considered: a NACA 0012 symmetric airfoil, visible in figure 4.1, a NACA 0015 symmetric airfoil, visible in figure 4.2, a non symmetric thin airfoil, figure 4.3 and an AgustaWestland proprietary airfoil. For the NACA 0012 airfoil two different chord length have been considered: this allowed to represent both smaller tail rotor blade (using a chord of 0.152 m) and main rotor blade, considering a chord of 0.53 m. The size of the body also influences the amount of icing accreting, mainly because of the different collection efficiency; for the NACA 0012 the differences resulting from the different chord can therefore be analysed. A thick NACA 0015, with chord length of 0.35 m, was selected, in order to also simulate thicker rotor blade. The GLC 305 airfoil considered has a chord length of 0.91 m and is representative of airfoil typically employed in wings. Finally a non symmetric AgustaWestland airfoil[2] has been used, to verify the behaviour of the tool with the type of airfoil used for helicopter; for this airfoil the original geometry has not been plotted.

To ensure repeatability of the shapes obtained the timestep used for each run was selected using the procedure described in 4.1; in section 4.2 the test conditions, the ice shapes are presented and discussed.

[1]LewInt integrates the ice accretion code LEWICE (version 3.2.2) with icing analysis tools and automated plotting. A fully functioning version of LewInt with LEWICE can be freely downloaded for a trial period.

[2]The shape and size of the airfoil are not reported because they are property of AgustaWestland and can not be disclosed.

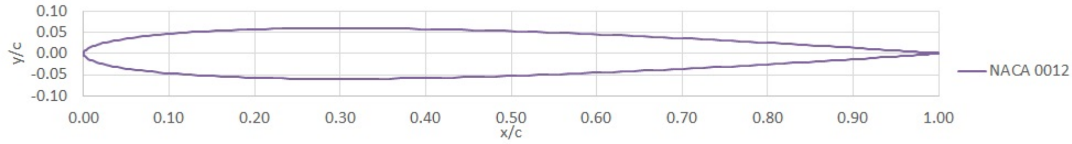

Figure 4.1: NACA0012 airfoil in adimensional coordinates.

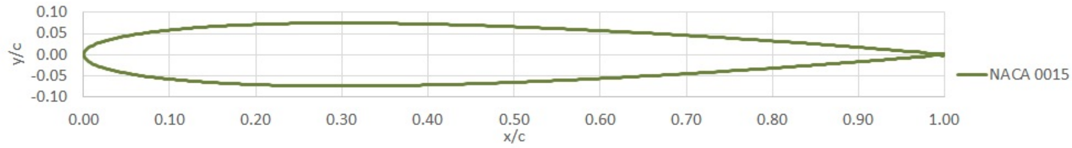

Figure 4.2: NACA0015 airfoil in adimensional coordinates.

4.1 Time step selection

Because icing is a continuous phenomenon simulated in discrete time interval, the size of the time step should not be excessive. The number of time steps was selected following the procedure given in [18] and used by LEWICE, so that results could be verified using an equal number of ice accretion steps; a first time step is computed using equation (4.1), which states that the maximum amount of ice accreted in a single time step should be no greater than 1% of the chord.

$$N = MIN\left(\frac{V_\infty \, LWC \, t_{spray}}{0.01 \, c \, \rho_{ice}}, 30\right) \tag{4.1}$$

Equation (4.1) may in some cases compute an excessively long timestep and consequently influence the ice shape. A second time step was then introduced, computed using equation (4.2), which results in a number of time steps equal to the minutes of ice accretion.

$$N2 = MIN\left(\frac{t_{spray}}{60}, 15\right) \tag{4.2}$$

A single number of time step was then obtained by selecting the largest between N and N2 and rounding to the next integer using equation (4.3).

$$N_{timestep} = ceil\left(MAX\left(N, N2\right)\right) \tag{4.3}$$

4.2 IceMAP 2D validation

Test cases conditions have been chosen in order to cover as much as possible the spectrum of icing conditions and to simulate all the possible typologies of ice forming, from rime to glaze accretion. For this reason the lowest temperature used was -28 $°C$, while the highest was -3 $°C$ (and total temperature above freezing, being equal to 1.3 $°C$); in the temperature range selected the other icing parameters have been modified, so that their effect on the final ice shape can be verified. Additionally, it also verified the capabilities of the IceMAP 2D for a wide range of conditions.

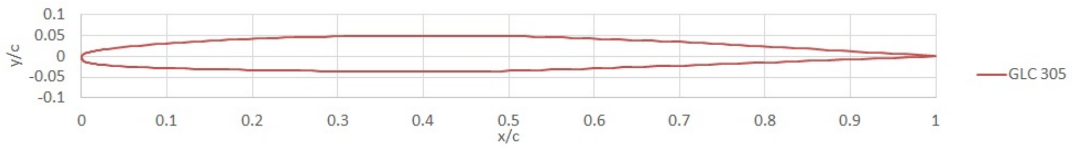

Figure 4.3: GLC305 airfoil in adimensional coordinates.

The icing conditions tested were selected in order to be also representative of the flight conditions typical of helicopter operations, especially for the main rotor. Helicopter main rotor blades are subject to large variation in angle of attack and Mach number: the blade tip on the advancing side generally operates at low angle of attack and Mach number of 0.8, while on the retreating side it operated at angles of attack up to 10 degrees and Mach number less than 0.4. These conditions can be averaged for a single revolution, to provide a single representative icing conditions; considering that the blade tip is generally less exposed to icing, as the kinetic heating due to the high speed limits the accretion of ice, and that the Mach number is higher at tip, the average angle of attack is about 5 degrees and the Mach number is roughly 0.4.

In the temperature range selected the following parameters have been modified:

- Airspeed: from 67 m/s to 130 m/s, corresponding to Mach 0.4. No experimental ice shape were found in literature for higher Mach number, thus test cases at higher Mach number were not simulated.
- Liquid water content: from 0.4 g/m^3 to 1 g/m^3. The value of 1 g/m^3 is similar to the maximum value expected in icing conditions and therefore leads to large amount of ice formation.
- Droplets diameter: from 15 μm to 38 μm. The 15 μm is the minimum size prescribed for icing certification, and the the range selected is representative of the dimensions mostly affecting airfoils.
- Angle of attack: from -2.5° to 8.5°.
- Accretion time: from 2 to 45 minutes.

The test conditions also allowed to test the capabilities and robustness of the tool: indeed, extremely long accretion time, up to 45 minutes, and have been combined with high external temperature (-10 $°C$) and high angle of attack (6°). These icing conditions leads to wet accretion with large horns on the surface, which are the most critical conditions to simulate. The tool worked properly also under this demanding conditions, and still produced an acceptable ice shape. Generally, though, ice is not allowed to grow for that long, as de icing systems will cyclically remove the accretion thus leaving a clean surface. Additionally, at lower temperature the accretion will have more and more rime characteristics, resulting in a streamlined accretion with no runback water on the surface. For these conditions the simulation is generally not as complex, and therefore it is expected that the code should be stable and reliable for all conditions.

The following ice shapes have been obtained for a symmetric NACA 0012 airfoil at increasing temperature while the other parameters remain unchanged. The results of IceMAP 2D has been compared with the output of LewInt and no data are available in literature for the following conditions:

	Run Rime	**Run Mixed**	**Run Glaze**
Airfoil	NACA 0012		
chord $[m]$	0.53		
Figure	4.4	4.6	4.8
AOA $[°]$	0		
$\mathbf{V}_\infty$ $[m/s]$	67.056		
$\mathbf{T}_\infty$ $[K]$	246.15	254.15	262.15
LWC $[g/m^3]$	0.99		
MVD $[\mu m]$	38		
t $[min]$	7		

Figure 4.4, 4.6 and 4.8 show the effect of increasing temperature, while the other variables remain unchanged; due to the high water loading ice shows glaze characteristics already at -18 $°C$, which are even more clear at -10 $°C$; yet the amount of runback water does not largely affects the icing limits, which remain almost unchanged in all conditions. Compared to LEWICE, the thickness at the leading edge is comparable for all the conditions, while some differences are visible at higher temperature in the horn size and position. Specifically, in LEWICE the horns appear to form at a further location while in IceMAP 2D they are closer to stagnation.

Because of the lack of an experimental ice shape to compare the simulated accretion no judgement can be expressed on the quality of the final result. In any case, the shape computed with IceMAP 2D and LEWICE are similar, and an experimental ice shape obtained at the given conditions should be significantly different.

For these runs also the pressure coefficient for the iced shape is compared with the output from LEWICE. The pressure coefficient shows a similar trend for all cases, but some differences in peaks are visible. These may be attributed to the differences in the shape computed, as the horns are positioned in the area where the largest discrepancies are visible. Additionally, for the rime condition, the coefficient of pressure for the iced airfoil has been computed using either the mesh used in the accretion process and the aerodynamic mesh. In this condition the computed coefficient is extremely similar, but may still result in some differences in the computation of the aerodynamic coefficients.

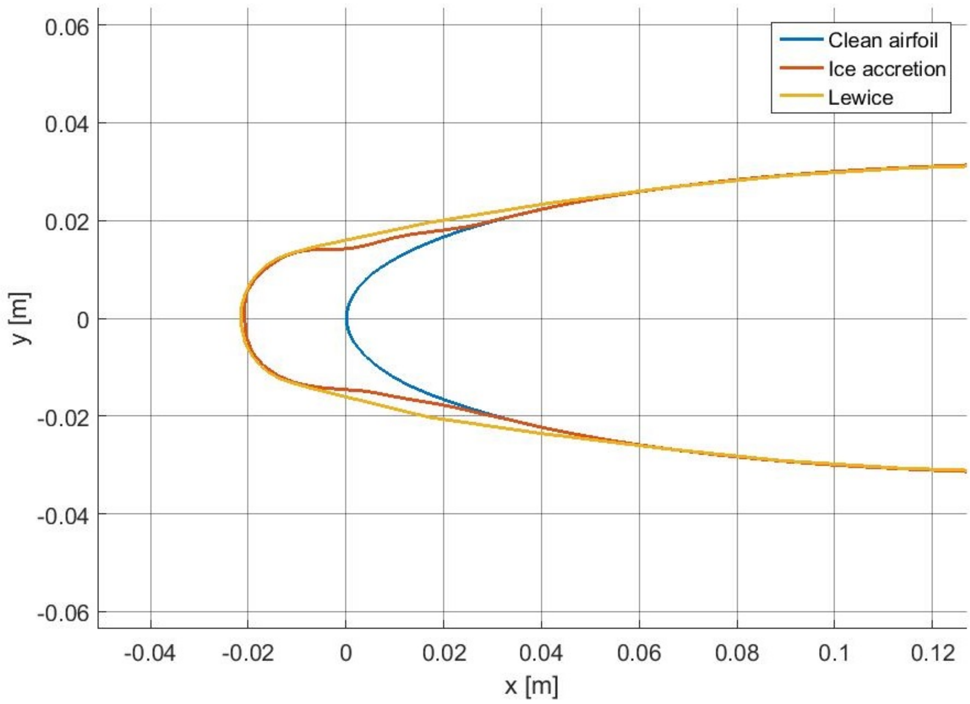

Figure 4.4: Run: rime. NACA0012, $V_\infty = 67.056\ m/s$, $T_\infty = 246.15\ K$, AOA = 0°, LWC = $0.99\ g/m^3$, MVD = $38\ \mu m$, t = $7\ min$.

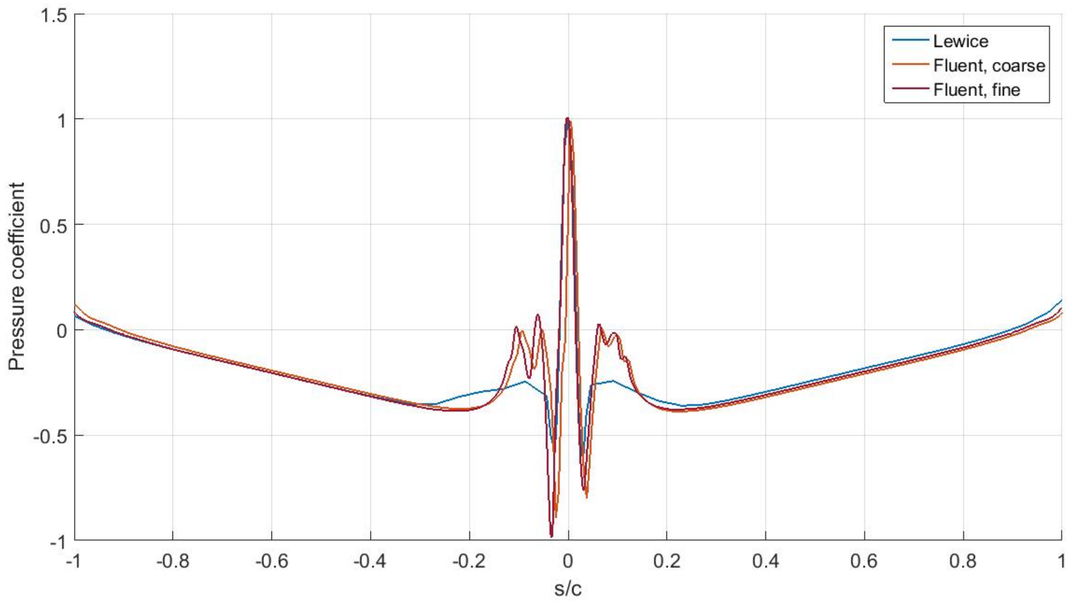

Figure 4.5: Coefficient of pressure on iced airfoil for run rime computed with two different meshes and compared with LEWICE.

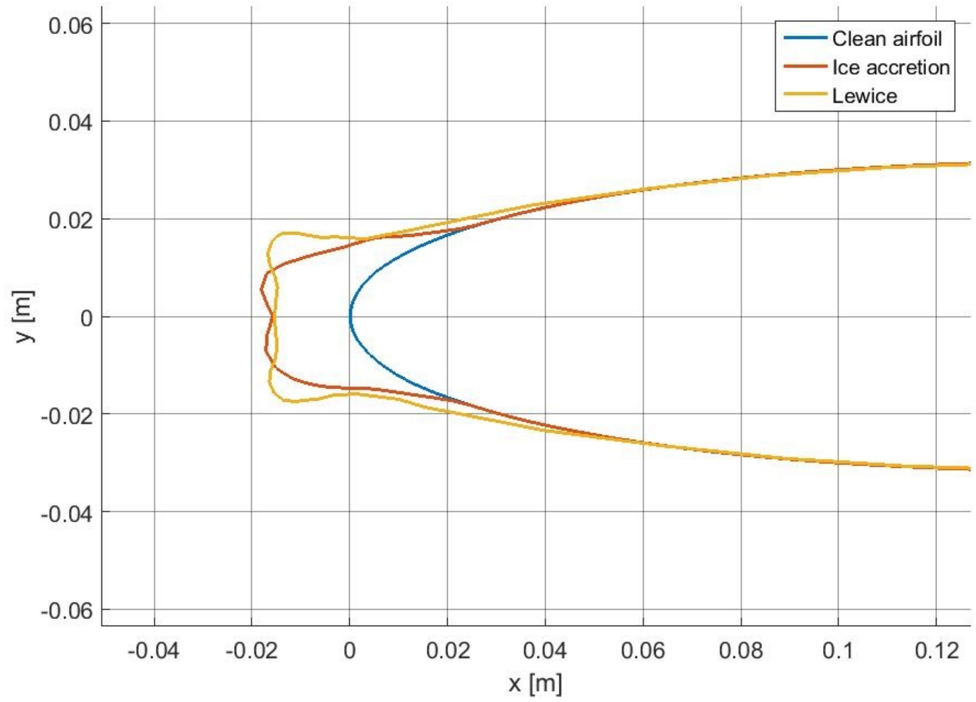

Figure 4.6: Run: rime. NACA0012, $V_\infty = 67.056\ m/s$, $T_\infty = 254.15\ K$, AOA = 0°, LWC = 0.99 g/m^3, MVD = 38 μm, t = 7 min.

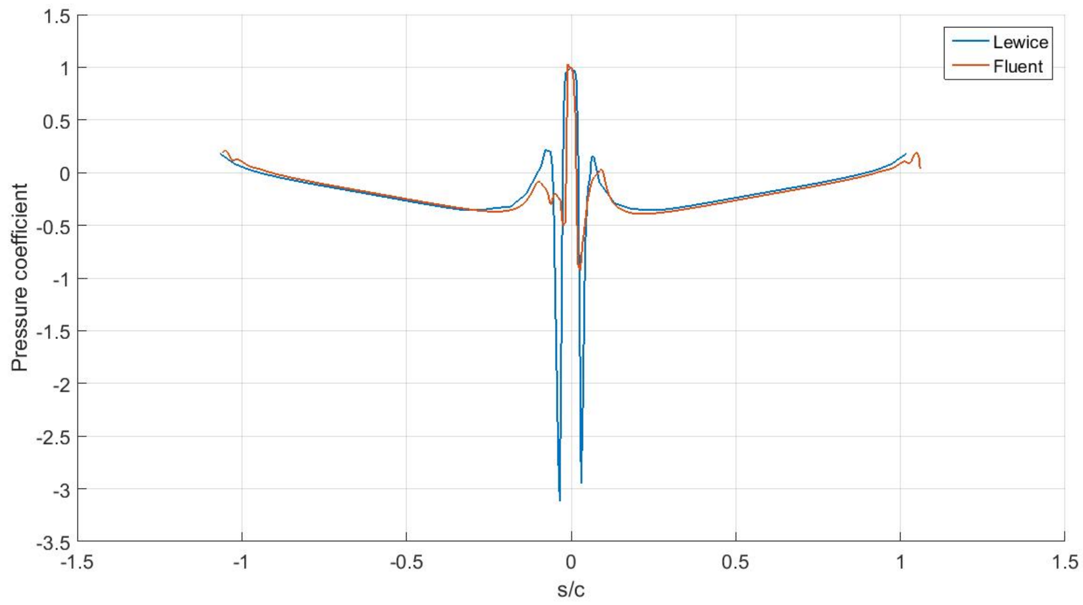

Figure 4.7: Coefficient of pressure for final ice shape compared with LEWICE.

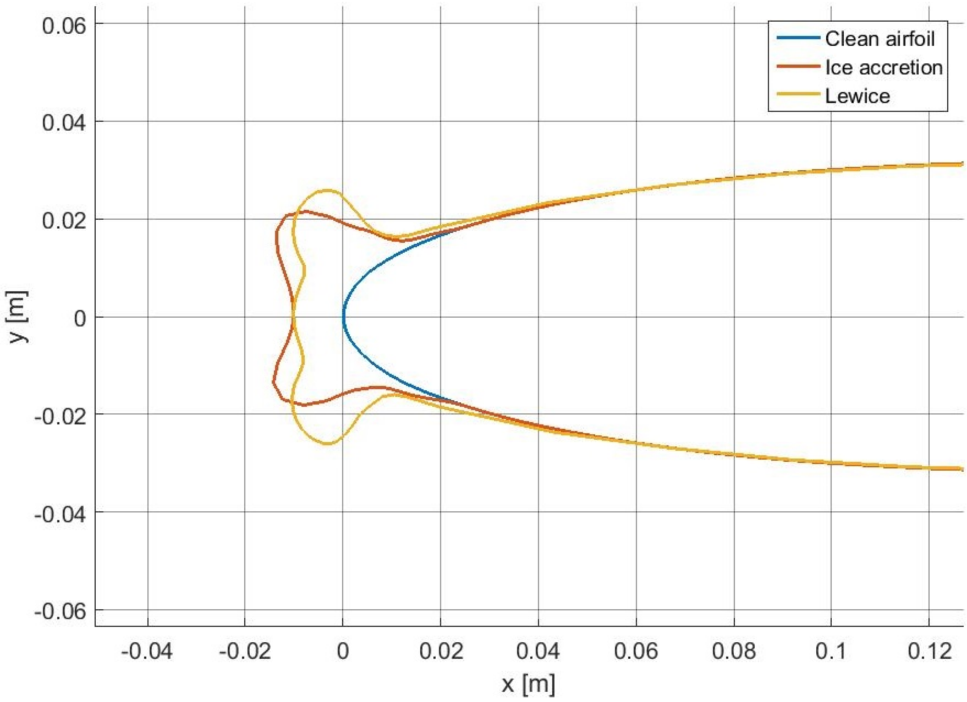

Figure 4.8: Run: rime. NACA0012, $V_{\infty} = 67.056\ m/s$, $T_{\infty} = 262.15\ K$, AOA = 0°, LWC = $0.99\ g/m^3$, MVD = $38\ \mu m$, t = $7\ min$.

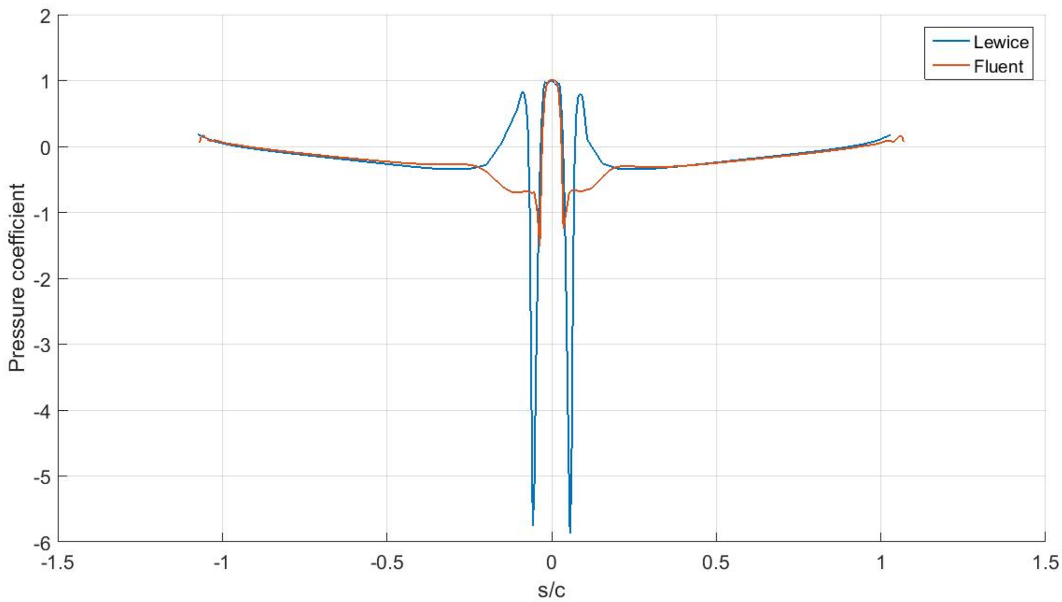

Figure 4.9: Coefficient of pressure for final ice shape compared with LEWICE.

The following ice shapes have been obtained for a symmetric NACA 0012 airfoil at increasing temperature while the other parameters remain unchanged. The results of IceMAP 2D has been compared with the output of LEWICE and experimental data available in literature for the following conditions:

	Run 425	**Run 11**	**Run 112**	**Run 118**	**Run 122**	**Run 421**
Airfoil	NACA 0012					
chord $[m]$	0.53					
Figure	4.10	4.11	4.12	4.13	4.14	4.15
AOA $[°]$	4					
$\mathbf{V}_\infty$ $[m/s]$	67.16	67.056	67.056	67.056	67.056	67.1
$\mathbf{T}_\infty$ $[K]$	244.51	253.69	259.84	263.14	265.35	268.4
LWC $[g/m^3]$	1					
MVD $[\mu m]$	20					
t $[min]$	6					

The icing conditions for figure 4.10 to 4.15 are similar to those of 4.4, 4.6 and 4.8, but the airfoil is at 4 degrees and droplet size is almost halved. The total accretion time has also been reduced to 6 minutes. In these cases (and all of the following) also an experimental ice shape is available. In run 4.10 the accretion is of type rime, but compared to 4.4 the positioning of the maximum thickness has slightly moved on the lower side of the airfoil due to the angle of attack. Therefore the ice shape is not symmetrical, and the icing limits on the suction and pressure side are different; additionally, the smaller particles also result in a larger impinged airfoil surface. Comparison with experimental data and LEWICE shows good agreement for both the icing limit and the maximum thickness and direction. Compared with LEWICE IceMAP 2D shows only minor differences, as can be expected in a rime accretion.

When free stream temperature reaches -20 $°C$, in figure 4.11, a limited amount of runback water starts to appear; temperature is similar to that in 4.6, as can be expected considering that only the angle of attack and the particle size have changed. The iced surface computed with IceMAP 2D shows more irregularities, but there is still good agreement with experimental data for icing limit and maximum thickness.

Runback water increases when temperature reaches -13 $°C$, as in figure 4.12, but in this case IceMAP 2D predicts the formation of a distinct horn on the lower side which is not visible in the experimental shape. A similar effect, although less evident, is visible in figure 4.13. In both cases the thickness at stagnation and icing limits are comparable with the experimental ice shape, as well as the ice formation on the upper side of the airfoil. The differences are probably caused by the modelling of the water film and the thermal exchange between water and air; indeed, the horn formation is caused by the freezing of runback water, and therefore a correct value of surface roughness and heat transfer coefficient can impact the type of ice growing. Also the modelling of the film flow may be responsible for differences, which in the present work is computed without considering the effect of air shear. In these cases also LEWICE exhibit some clear differences with the experimental ice shape, although the thickness location is different compared with IceMAP 2D. In LEWICE more ice is predicted on the upper horn, while the lower accretion is underpredicted.

In figure 4.14 the air temperature is further increased at -7 $°C$, and the ice shape computed in IceMAP 2D has significantly improved compared to previous runs; the horns on the lower side is not visible, because convective and evaporative cooling are not sufficient to freeze the water film, which can flow further aft. This is also visible on the upper horn, which has moved further away from the stagnation point. In this case IceMAP 2D compares favourably with the experimental ice shape, as icing limits, ice thickness and distribution are similar to those tested. Compared to LEWICE, in this condition IceMAP 2D also provides a better representation of the actual accretion, as the upper horn and lower accretion is more accurate.

In run 421, figure 4.15, the higher temperature (approximately -4 $°C$) has a dramatic effect on the final ice formation, because the amount of heating on the airfoil impedes the formation of distinctive horns; in these conditions, the water film mostly affects the extent of the iced surface, which compared to previous runs has increased on both the upper and lower surface. A significant amount of ice is still forming on the airfoil, but the maximum thickness is less than in previous cases. Although the horn on the upper side and the thickness of ice near stagnation are marginally under estimated, the icing limit, especially on the lower side are correctly captured by IceMAP 2D; instead, LEWICE seems to under estimate not only the amount of ice accreting but also the icing limit on the lower surface.

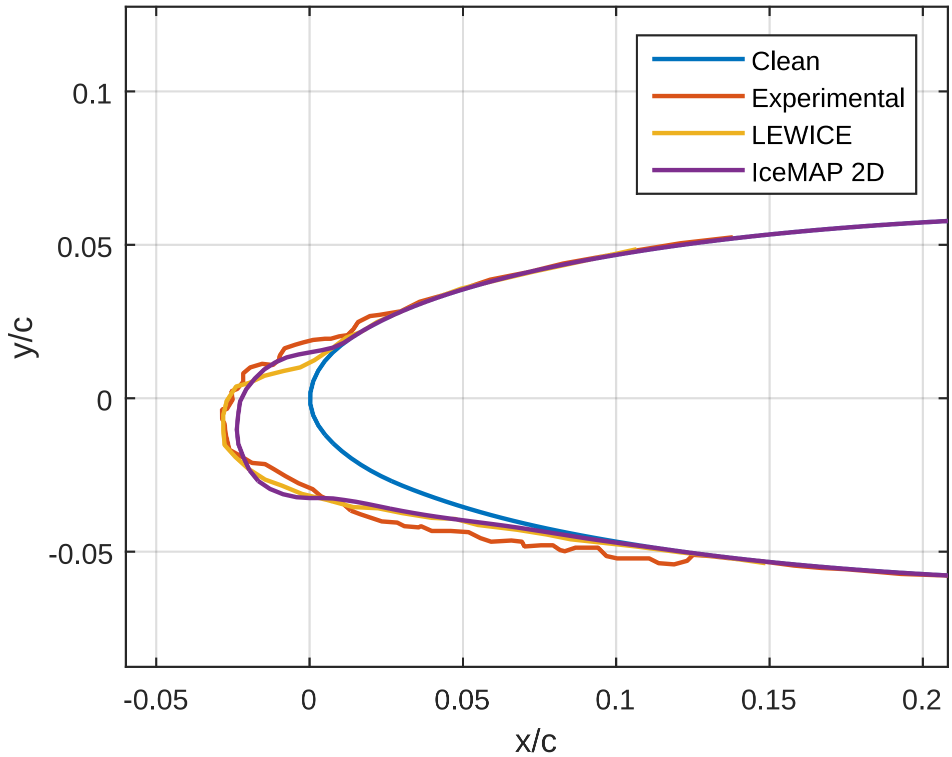

Figure 4.10: Run: 425. NACA0012, $V_\infty = 67.1\ m/s$, $T_\infty = 244.51\ K$, AOA = 4°, LWC = 1 g/m^3, MVD = 20 μm, t = 6 min.

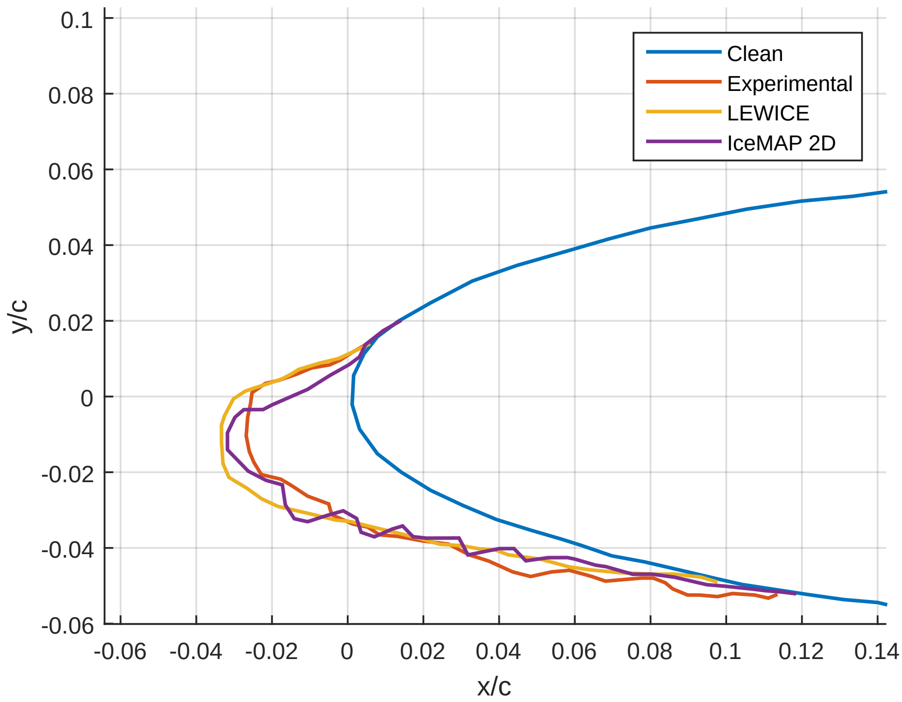

Figure 4.11: Run: 11. NACA0012, $V_\infty = 67.056\ m/s$, $T_\infty = 253.69\ K$, AOA = 4°, LWC = $1\ g/m^3$, MVD = $20\ \mu m$, t = $6\ min$.

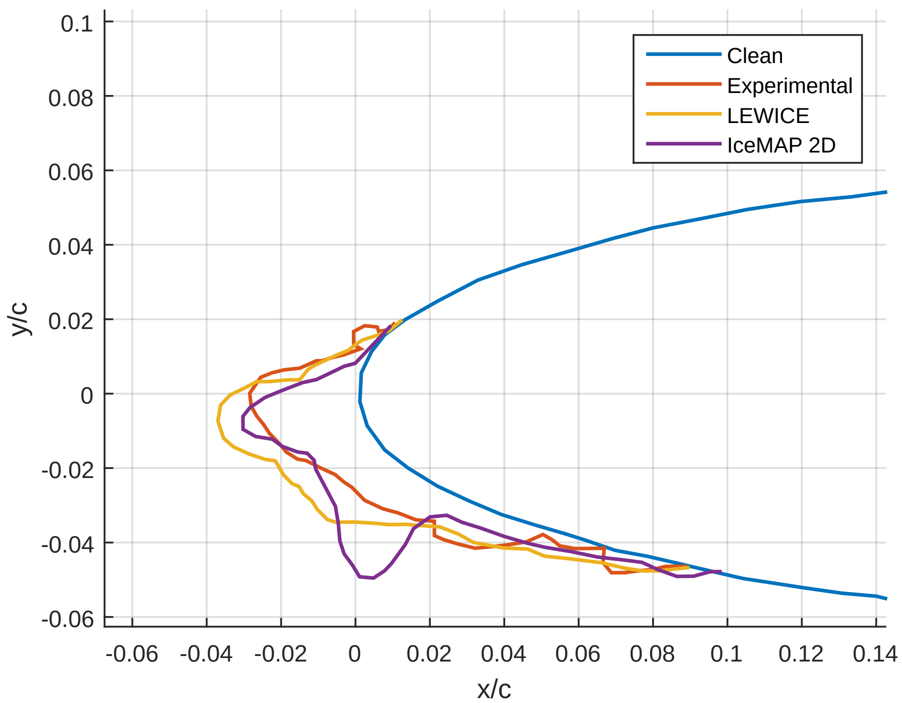

Figure 4.12: Run: 112. NACA0012, $V_\infty = 67.056\ m/s$, $T_\infty = 259.8\ K$, AOA = 4°, LWC = $1\ g/m^3$, MVD = $20\ \mu m$, t = $6\ min$.

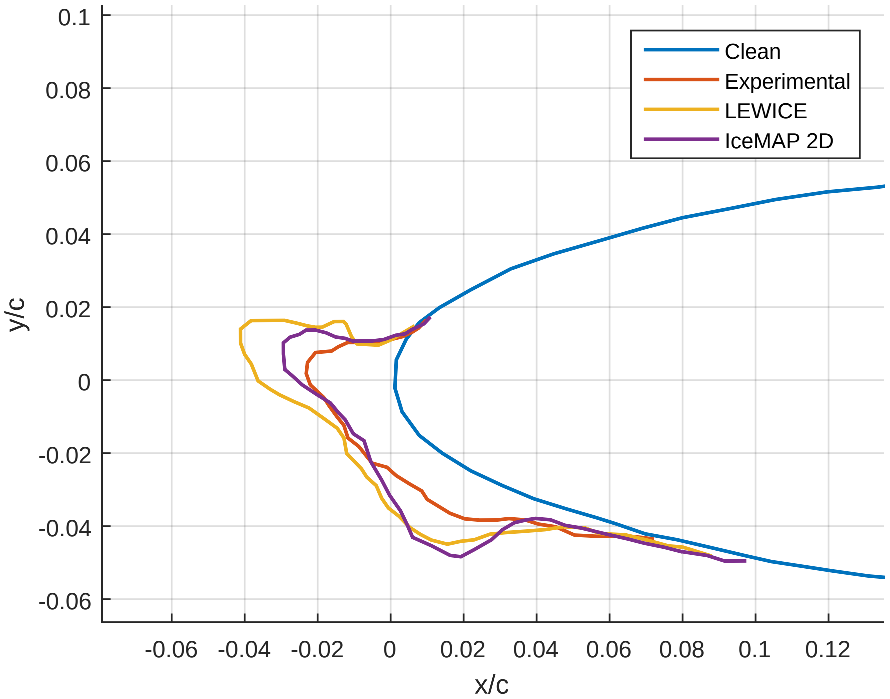

Figure 4.13: Run: 118. NACA0012, $V_\infty = 67.056\ m/s$, $T_\infty = 263.14\ K$, AOA = 4°, LWC = 1 g/m^3, MVD = 20 μm, t = 6 min.

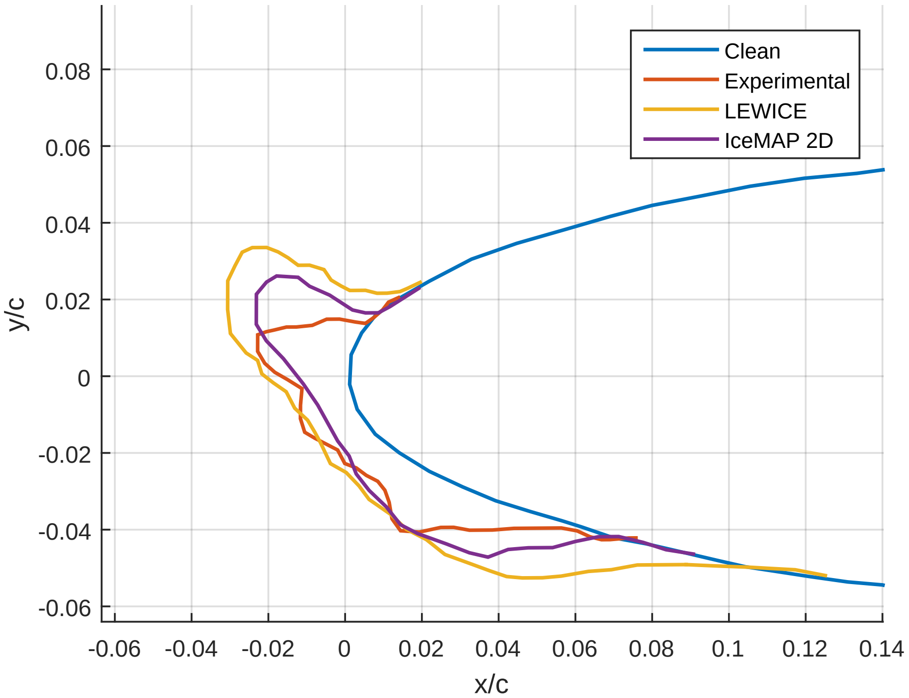

Figure 4.14: Run: 122. NACA0012, $V_\infty = 67.056\ m/s$, $T_\infty = 265.35\ K$, AOA = 4°, LWC = 1 g/m^3, MVD = 20 μm, t = 6 min.

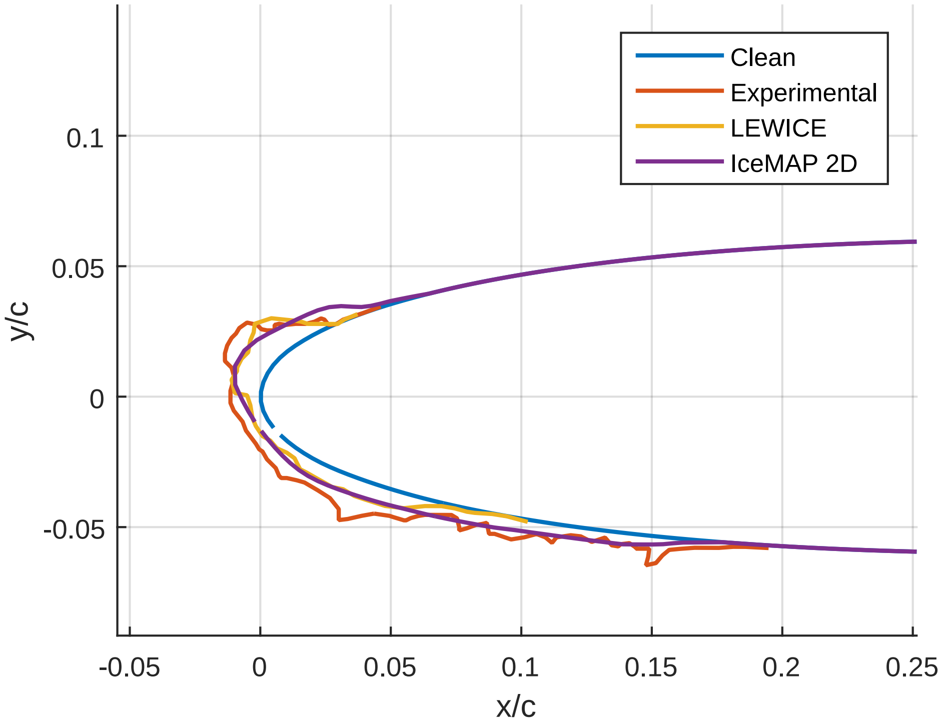

Figure 4.15: Run: 421. NACA0012, $V_\infty = 67.1\ m/s$, $T_\infty = 268.4\ K$, AOA = 4°, LWC = $1\ g/m^3$, MVD = $20\ \mu m$, t = $6\ min$.

The following ice shapes have been obtained for a symmetric NACA 0012 airfoil at increasing temperature while the other parameters remain unchanged. The results of IceMAP 2D has been compared with the output of LEWICE and experimental data available in literature for the following conditions:

	Run 405	**Run 5512**	**Run 403**	**Run 5528**
Airfoil	NACA 0012			
chord $[m]$	0.53			
Figure	4.16	4.17	4.18	4.19
AOA $[°]$	4			
$\mathbf{V}_\infty$ $[m/s]$	102.8			
$\mathbf{T}_\infty$ $[K]$	250.37	256.78	262.04	265.67
LWC $[g/m^3]$	0.55			
MVD $[\mu m]$	20			
t $[min]$	20			

Compared to the previous runs in this cases also the freestream velocity has been increased to 102 m/s and accretion time to 7 minutes, while the liquid water content has been decreased to 0.55 g/m^3. As a result, the decrease in impinging mass due to the lower LWC is compensated by the raise in free stream velocity, therefore the differences with the previous runs should only be caused by the different collection efficiency (affected by airspeed) and aerodynamic heating.

The lowest temperature used was -23 $°C$ in run 405, figure 4.16, which is sufficiently low to freeze all impacting water. The computed shape is comparable with both experimental and analytical simulations, and is also similar to that computed in run 425.

A limited amount of runback water appears in run 5512, figure 4.17, which mostly affect icing near the stagnation. In LEWICE, though, the ice shape is still identical to that computed in run 405.

A larger difference is visible in figure 4.18, where the water film resulted in the formation of a pair of horns of limited dimension on lower surface and at the leading edge. Both horns are well captured by IceMAP 2D, but in the experimental shape some water is also freezing past the lower horn; the difference may be attributed to both the simplified modelling of the water film, which appear to be result in more regular freezing in all icing simulation. In any case it has not a large impact on the IceMAP 2D shape, which still captures the most significant features.

At the highest temperature of -6 $°C$ of run 5528, figure 4.19, the mass of runback water has largely increased, as can be seen by the lower thickness at stagnation and the size of the horns, which are now clearly distinguishable, especially on the upper side. Additionally, also their position has changed, as water flows further back before freezing. In this case IceMAP 2D show an extremely good agreement with experimental data for the upper horn, while only minor differences appear on the lower side. The localized accretion visible on the lower surface for the experimental ice shape are most probably the result of a limited number of droplets either flowing or impinging further aft; this would require a modelling of single droplets, which is not possible with the macroscopic approach considered. Still, the influence is extremely limited and the IceMAP 2D shape is well compares with wind tunnel data. In this case, on the contrary, LEWICE simulate a significant amount of water freezing on the upper horn, which largely alter the final accretion.

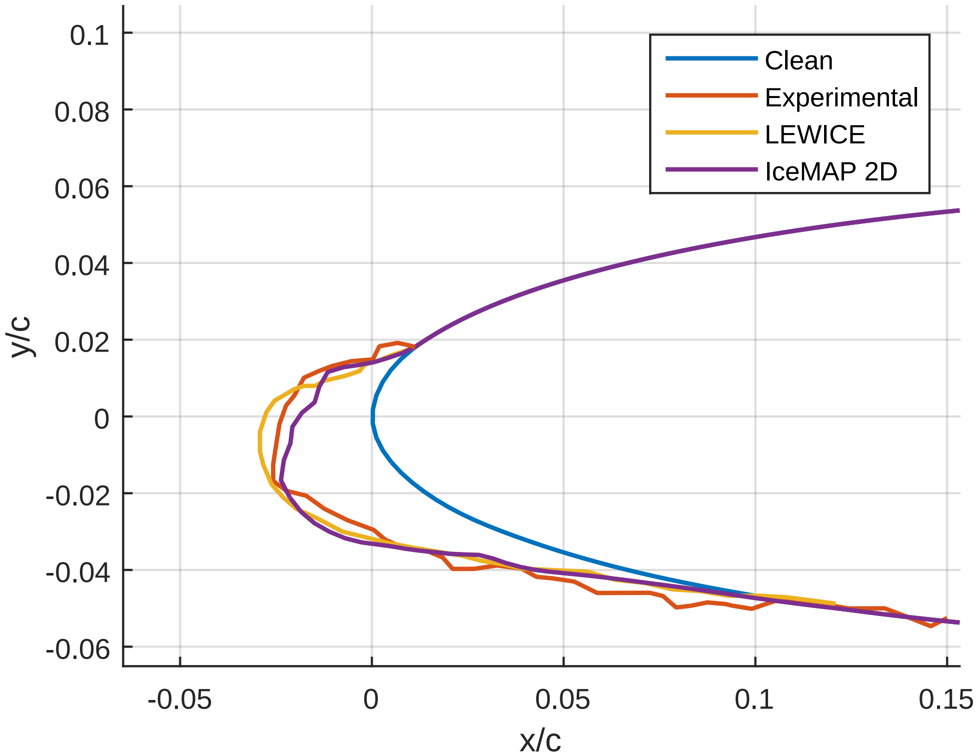

Figure 4.16: Run: 405. NACA0012, $V_\infty = 102.8\ m/s$, $T_\infty = 250.37\ K$, AOA = 4°, LWC = 0.55 g/m^3, MVD = 20 μm, t = 7 min.

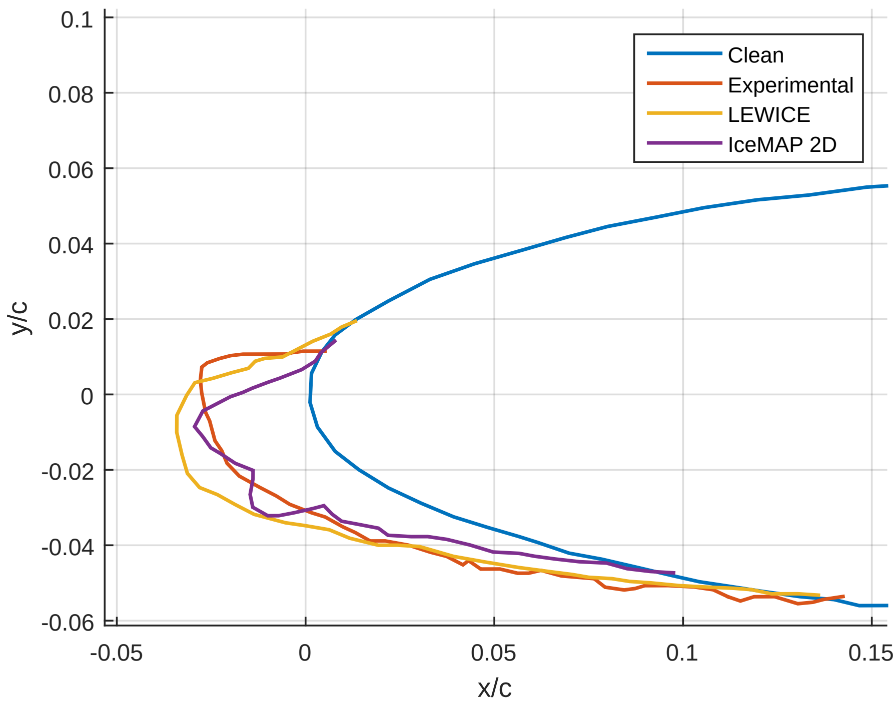

Figure 4.17: Run: 5512. NACA0012, $V_\infty = 102.8\ m/s$, $T_\infty = 256.78\ K$, AOA $= 4°$, LWC $= 0.55\ g/m^3$, MVD $= 20\ \mu m$, t $= 7\ min$.

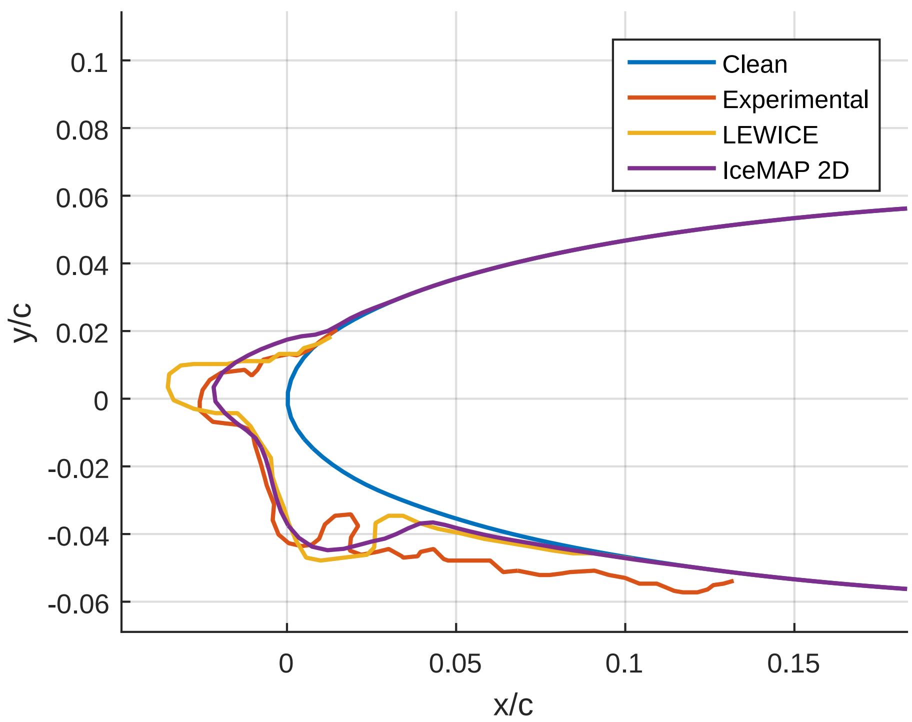

Figure 4.18: Run: 403. NACA0012, $V_\infty = 102.8\ m/s$, $T_\infty = 262.04\ K$, AOA $= 4°$, LWC $= 0.55\ g/m^3$, MVD $= 20\ \mu m$, t $= 7\ min$.

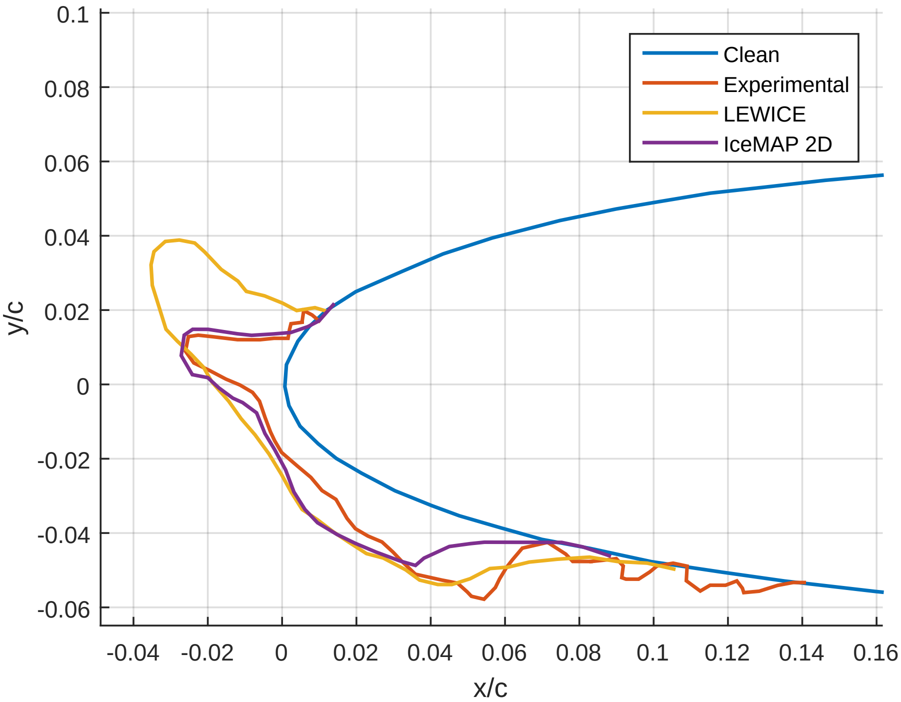

Figure 4.19: Run: 5528. NACA0012, $V_\infty = 102.8\ m/s$, $T_\infty = 265.67\ K$, AOA = 4°, LWC = 0.55 g/m^3, MVD = 20 μm, t = 7 min.

The following ice shapes have been obtained for a symmetric NACA 0012 airfoil at increasing accretion time while the other parameters remain unchanged. The results of IceMAP 2D has been compared with the output of LEWICE and experimental data available in literature for the following conditions:

	Run 411	**Run 403**
Airfoil	NACA 0012	
chord $[m]$	0.53	
Figure	4.20	4.18
AOA $[°]$	4	
$\mathbf{V}_\infty$ $[m/s]$	102.8	
$\mathbf{T}_\infty$ $[K]$	262.04	
LWC $[g/m^3]$	0.55	
MVD $[\mu m]$	20	
t $[min]$	14	7

In run 411, figure 4.20, the conditions are the same as in run 403, figure 4.21, but the accretion time has been increased to 14 minutes. Interestingly, in the 7 minutes ice accretion the experimental lower icing limits are larger than in the 14 minutes run; this is probably the result of the variability typically observable in icing tests under nominally identical conditions. Indeed, it is not possible to perfectly replicate the conditions (like temperature and droplet diameter) in different runs; a further variability is due to the icing of individual droplets at slightly different position, which eventually leads to localized accretion at different location.

Because of the good agreement with the experimental shape for the lower accretion time, also run 411 could be expected to provide as good a result. In this case, instead, IceMAP 2D under predicts the size of the horn near the leading edge of the airfoil, while the lower accretion is modelled correctly. The differences may be explained by the coarse mesh size (2 mm) used in the case; as a result, a single mesh element covers a large area of the horn, reducing the definition of the geometry and leading to accretion in the wrong direction. A finer size may in this run provide improvement of the result, but it has not been verified.

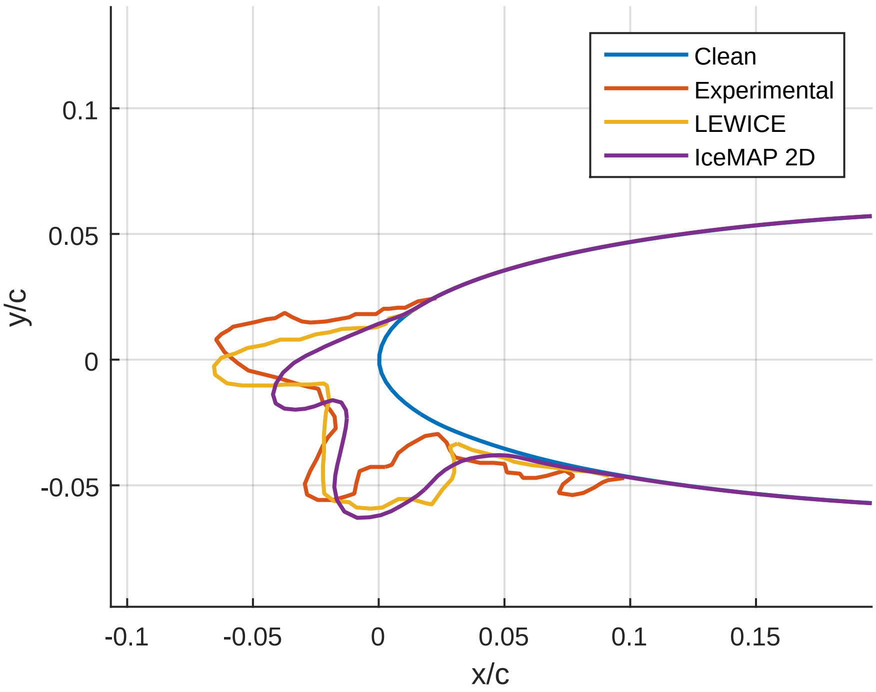

Figure 4.20: Run: 411. NACA0012, $V_\infty = 102.8\ m/s$, $T_\infty = 262.04\ K$, AOA = 4°, LWC = $0.55\ g/m^3$, MVD = $20\ \mu m$, t = $14\ min$.

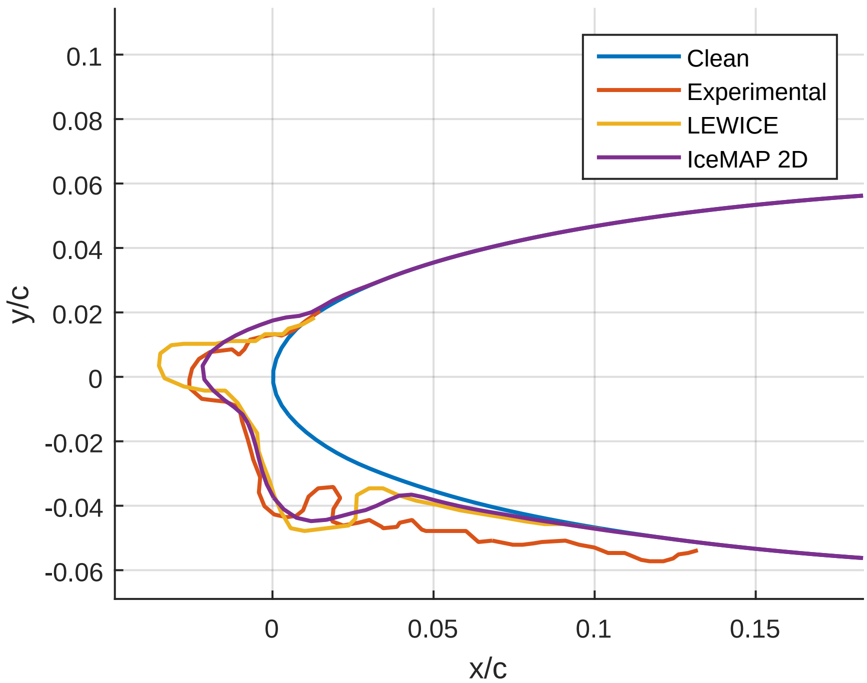

Figure 4.21: Run: 403. NACA0012, $V_\infty = 102.8\ m/s$, $T_\infty = 262.04\ K$, AOA = 4°, LWC = $0.55\ g/m^3$, MVD = $20\ \mu m$, t = $7\ min$.

The following ice shapes have been obtained for a symmetric NACA 0012 airfoil at increasing angle of attack while the other parameters remain unchanged. The results of IceMAP 2D has been compared with the output of LEWICE and other icing tools and experimental data available in literature for the following conditions:

	Run DRA37	**Run DRA38**
Airfoil	NACA 0012	
chord $[m]$	0.152	
Figure	4.22	4.23
AOA $[°]$	0	8.5
$\mathbf{V}_\infty$ $[m/s]$	130.5	
$\mathbf{T}_\infty$ $[K]$	260.7	
LWC $[g/m^3]$	0.5	
MVD $[\mu m]$	17.5	
t $[min]$	2	

In run DRA37, figure4.22, and DRA38, figure 4.23, a particularly small NACA 0012 is used, with chord length of 0.152 m, combined with a high velocity (130 m/s, $Ma \approx 0.4$) and different angle of attack. Additionally, the ice shape is compared with experimental data, LEWICE and other icing software, developed respectively by DRA and ONERA. In 4.22 the angle of incidence was zero, but the computed ice shape was not perfectly symmetrical; this the result of the non exact solution of the flow field, which also impact the solution of thermodynamic balance and eventually affects the ice shape. However, IceMAP 2D simulated two large horns, typical of glaze accretion, in the correct direction; indeed, the horn thickness is comparable with experimental data, but not the thickness at stagnation point. Probably this is caused by the runback water modelling in IceMAP 2D; in the accretion module the water is expected to flow away from the stagnation point, but in reality this is an approximation that may be incorrect in some cases. At high velocity and glaze conditions, for example, this would result in water flowing from the stagnation point (located at the leading edge when the airfoil is at zero angle of attack) over the horns; in reality, the film flow is governed by air shear which in this case would probably prevent water from flowing past the horns, eventually freezing near the stagnation.

In run DRA38, figure 4.23, the angle of attack is 8.5 degrees, which is the highest angle tested. In this case the computed accretion is similar to LEWICE, but the experimental data has feature that are not captured correctly. The feathers on the lower surface are the result of localized ice accretion caused by the effects of single droplets, which in the icing tools are not modelled. A larger difference is visible near the leading edge, where the direction of accretion is different. Beside the effect of surface roughness and the modelling of the water film, also the size of the mesh may have influenced the result. Although in this case the size of the element used was 0.5 mm, because of the small airfoil size an even smaller dimensions may be needed, but no test have been conducted.

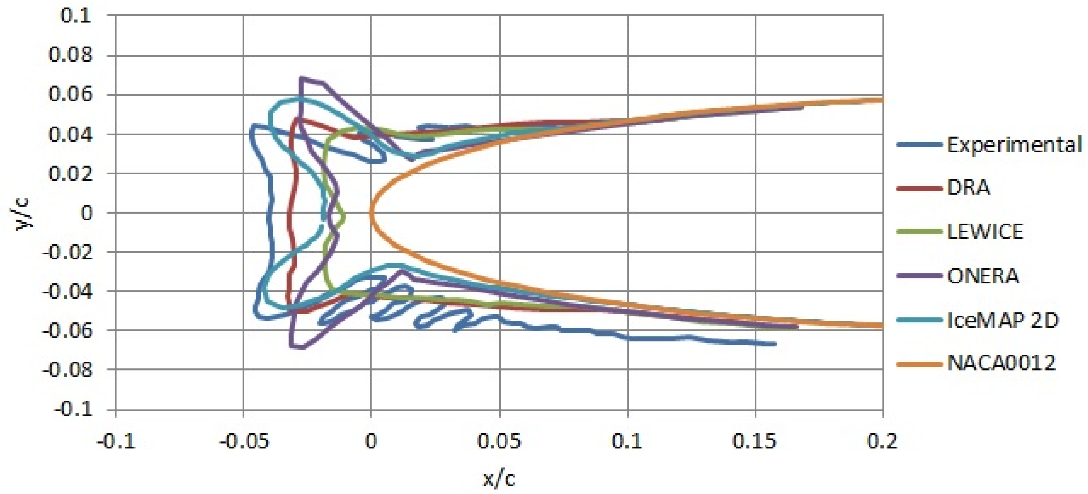

Figure 4.22: Run: DRA37. NACA0012, $V_\infty = 130.5\ m/s$, $T_\infty = 260.7\ K$, AOA $= 0°$, LWC $= 0.5\ g/m^3$, MVD $= 17.5\ \mu m$, t $= 2\ min$.

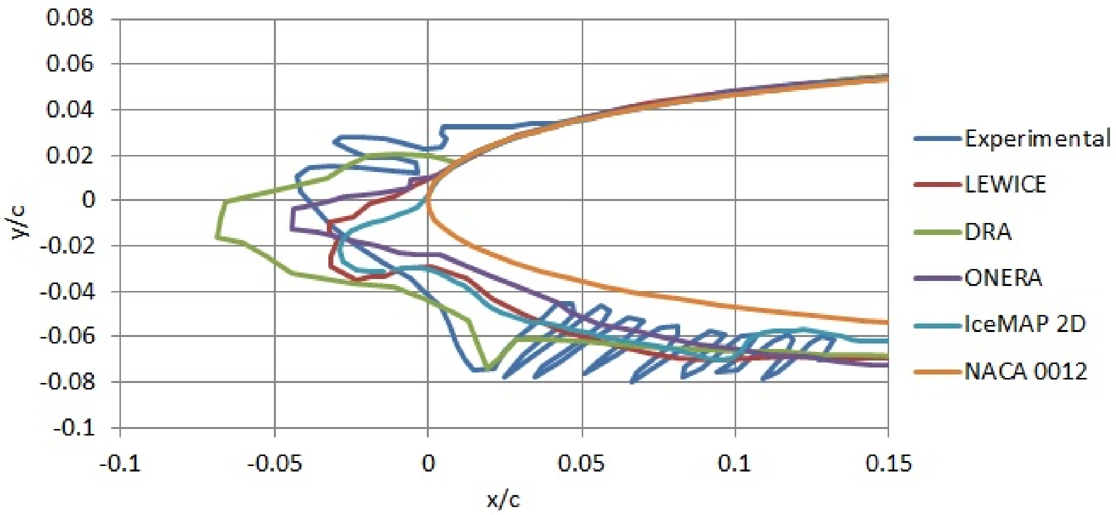

Figure 4.23: Run: DRA38. NACA0012, $V_\infty = 130.5\ m/s$, $T_\infty = 260.7\ K$, AOA $= 8.5°$, LWC $= 0.5\ g/m^3$, MVD $= 17.5\ \mu m$, t $= 2\ min$.

The following ice shapes have been obtained for a symmetric NACA 0012 airfoil. The results of IceMAP 2D has been compared with the output of LEWICE and experimental data available in literature for the following conditions:

	Run 412	**Run 406**
Airfoil	NACA 0012	
chord $[m]$	0.53	
Figure	4.24	4.25
AOA $[°]$	0	
$\mathbf{V}_\infty$ $[m/s]$	102.8	
$\mathbf{T}_\infty$ $[K]$	261.54	264.37
LWC $[g/m^3]$	0.47	0.4
MVD $[\mu m]$	30	20
t $[min]$	8.2	9.8

Run 412, figure 4.24, and run 406, figure 4.25, show the result of a longer icing exposure, reaching 8.2 and 9.8 minutes. In both cases the ice thickness is generally comparable as well as the icing limits. Larger differences exist for the longer accretion time, run 406, which also has the highest temperature; in this case the horn thickness on the upper surface and the lower accretion are partly under estimated. However, the final ice shape shows good agreement with experimental ice shape, and although LEWICE better model the horn it misses part of the accretion on the lower side of the airfoil.

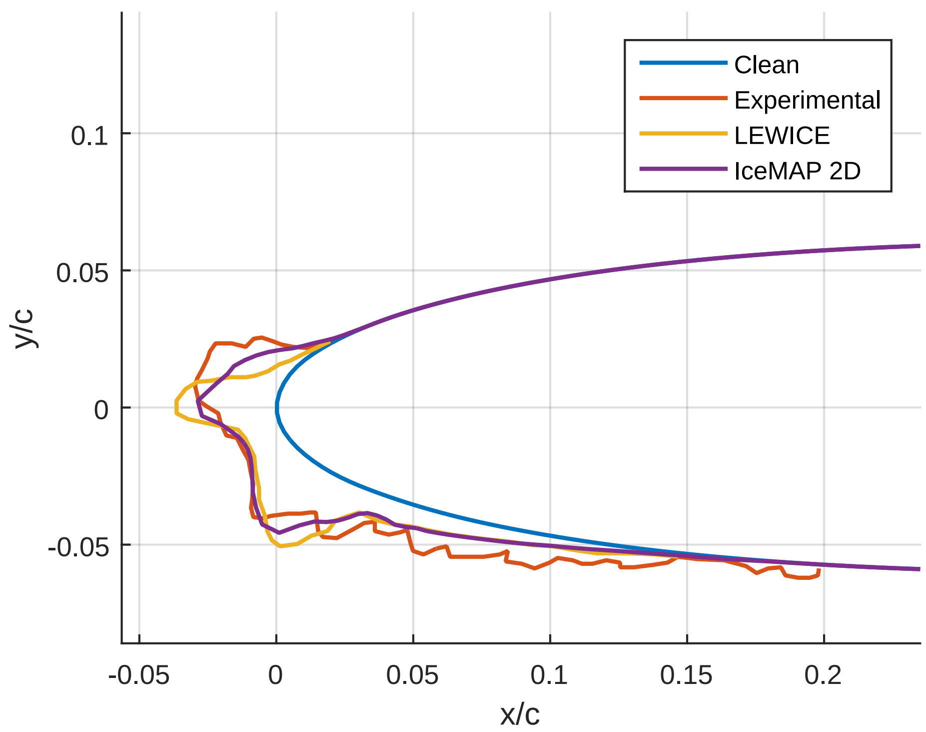

Figure 4.24: Run: 412. NACA0012, $V_\infty = 102.8\ m/s$, $T_\infty = 261.54\ K$, AOA = 4°, LWC = $0.47\ g/m^3$, MVD = $30\ \mu m$, t = $8.2\ min$.

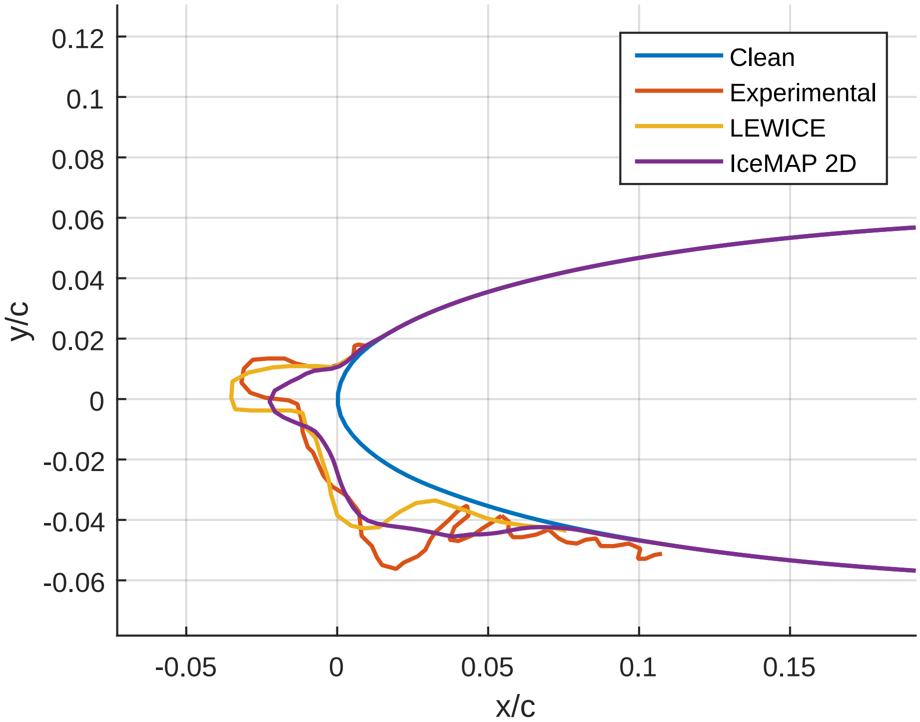

Figure 4.25: Run: 406. NACA0012, $V_\infty = 102.8\ m/s$, $T_\infty = 264.37\ K$, AOA = $4°$, LWC = $0.4\ g/m^3$, MVD = $20\ \mu m$, t = $9.8\ min$.

The following ice shapes have been obtained for a symmetric NACA 0015 airfoil. The results of IceMAP 2D has been compared with the output of LEWICE and experimental data available in literature for the following conditions:

	Run 624963	**Run 624966**
Airfoil	NACA 0015	
chord $[m]$	0.353	
Figure	4.26	4.27
AOA $[°]$	0	
$\mathbf{V}_\infty$ $[m/s]$	95.215	85.39
$\mathbf{T}_\infty$ $[K]$	262.85	263.07
LWC $[g/m^3]$	0.75	0.77
MVD $[\mu m]$	19	23.4
t $[min]$	10	10.8

In run 624963 and 624966, figure respectively 4.26 and 4.27, the airfoil used is a thick NACA0015 of 0.35 m chord. Again, the conditions are typical of wet accretion, as can be seen by the large horn accreting at the leading edge. Although the two cases are different, the icing conditions are not significantly different and result in similar ice formation. The experimental ice shape shows two main large horns forming and additional accretions further aft. In both of these runs IceMAP 2D provide a more accurate result than LEWICE; the direction and thickness of the main horns is significantly closer to the experimental, while the thickness at the leading edge is similar for both icing tools. The smaller ice formations past the two horns is not clearly visible in either analytical tools, although in IceMAP 2D a small ridge appears on both the upper and lower horns.

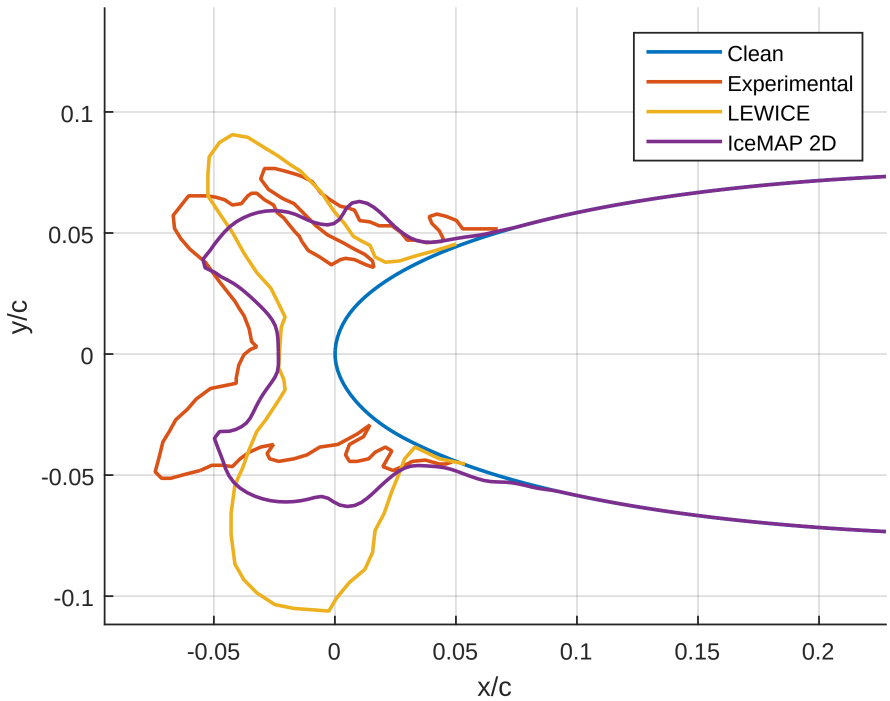

Figure 4.26: Run: 624963. NACA0015, $V_\infty = 95.215\ m/s$, $T_\infty = 262.85\ K$, AOA $= 0°$, LWC $= 0.75\ g/m^3$, MVD $= 19\ \mu m$, t $= 10\ min$.

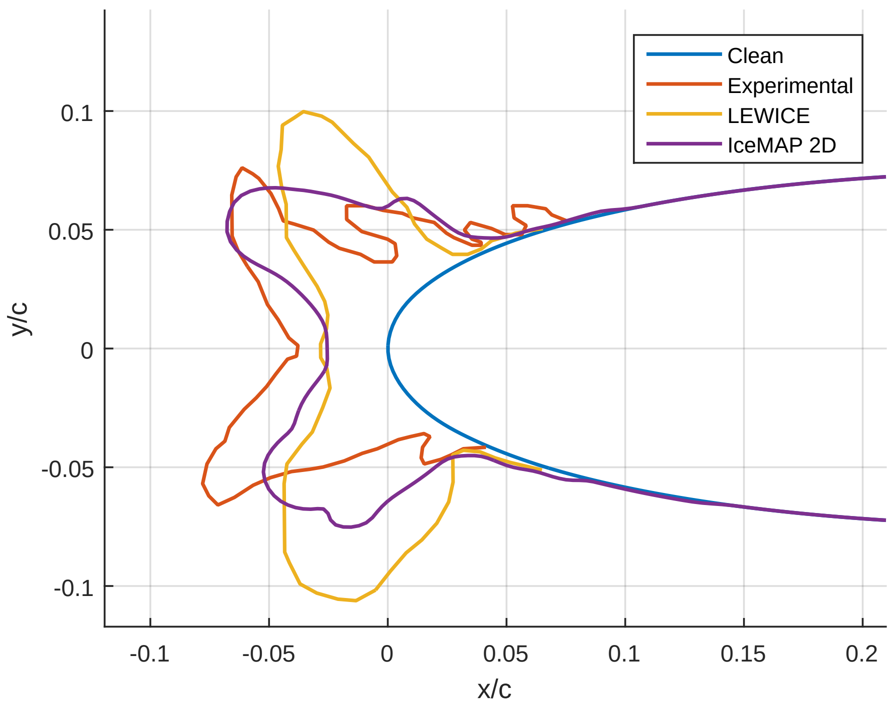

Figure 4.27: Run: 624966. NACA0015, $V_\infty = 85.39\ m/s$, $T_\infty = 263.07\ K$, AOA $= 0°$, LWC $= 0.77\ g/m^3$, MVD $= 23.4\ \mu m$, t $= 10.8\ min$.

The following ice shapes have been obtained for a GLC 305 airfoil. The results of IceMAP 2D has been compared with the output of LEWICE and experimental data available in literature for the following conditions:

	Run 72701	**Run 72703**
Airfoil	GLC 305	
chord $[m]$	0.91	
Figure	4.28	4.29
AOA $[°]$	6	
$\mathbf{V}_\infty$ $[m/s]$	90	
$\mathbf{T}_\infty$ $[K]$	263.2	
LWC $[g/m^3]$	0.43	0.6
MVD $[\mu m]$	20	15
t $[min]$	45	22.5

In run 72701, figure 4.28, the airfoil is 0.91 m chord GLC305, which is a particularly thin airfoil. Ice conditions are extremely demanding, as they include long accretion time, 45 minutes, high angle of attack, 6 degrees, and high temperature, -10 $°C$. This is the longest accretion time used with IceMAP 2D, and was divided in 15 time steps of three minutes each. As an indication of the computation time required, the simulation took 1 hour and 45 minutes with a serial computation, which is acceptable considering that Fluent is tasked with computing a flow field solution at each accretion. Indeed, most of the simulation time is due to flow field solution, while the ice accretion module, therefore considering particle tracking, thermodynamic solution and update of the geometry and mesh takes roughly 1 minutes per time step.

IceMAP 2D successfully completed the simulation and provided an accurate ice shape, even if some differences can be seen. Specifically, these are in the area near the top horn, which is only partially visible in IceMAP 2D, and in the lower icing, where a small accretion is present. Still, the differences are not particularly large, especially considering the long accretion time. In the simulation process no errors were encountered, thus reducing the time step, at the cost of the simulation time, may also be a possibility to improve the result obtained. Further, the fact that the ice shape is still comparable proves that the approximations introduced in the modelling, like the simplification of the water film flow, are reasonable and do not have a particularly large effect on the final ice shape.

Run 72703, figure 4.29, also is long accretion simulation of 22.5 minutes, at higher liquid water content (0.6 g/m^3) and smaller droplet size (15 μm). Compared to run 72701 the ice thickness at the leading edge is smaller, because of the lower icing time, but not halved as the accretion time because of the higher water content. In this case therefore glaze feature, like horns, are more visible, because the increase of impinging water is not coupled with an increase in icing in the impacting area. Water may flow and result in larger area of the airfoil being affected by icing. In this case the horn thickness is not significantly less than the experimental value, and its direction is almost correct; compared to LEWICE this provide a better approximation of the upper horn, while on the lower surface IceMAP 2D predicts the formation of a second horn which is as clear in the experiments. Overall, also in this case the computed ice shape is comparable, including for what concern the icing limits.

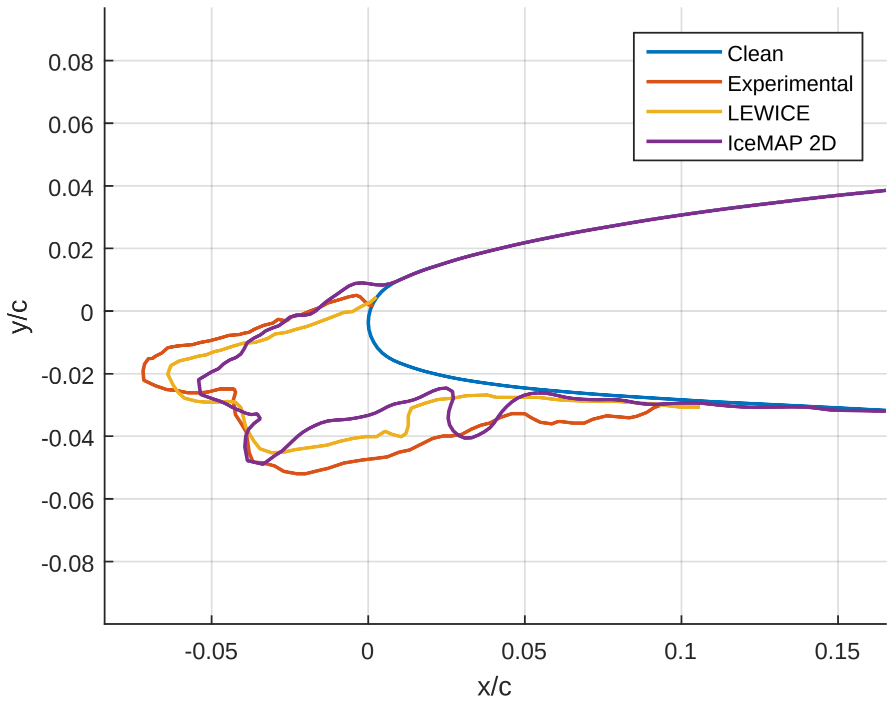

Figure 4.28: Run: 072701. GLC305, $V_\infty = 90\ m/s$, $T_\infty = 263.2\ K$, AOA = 6°, LWC = $0.43\ g/m^3$, MVD = $20\ \mu m$, t = $45\ min$.

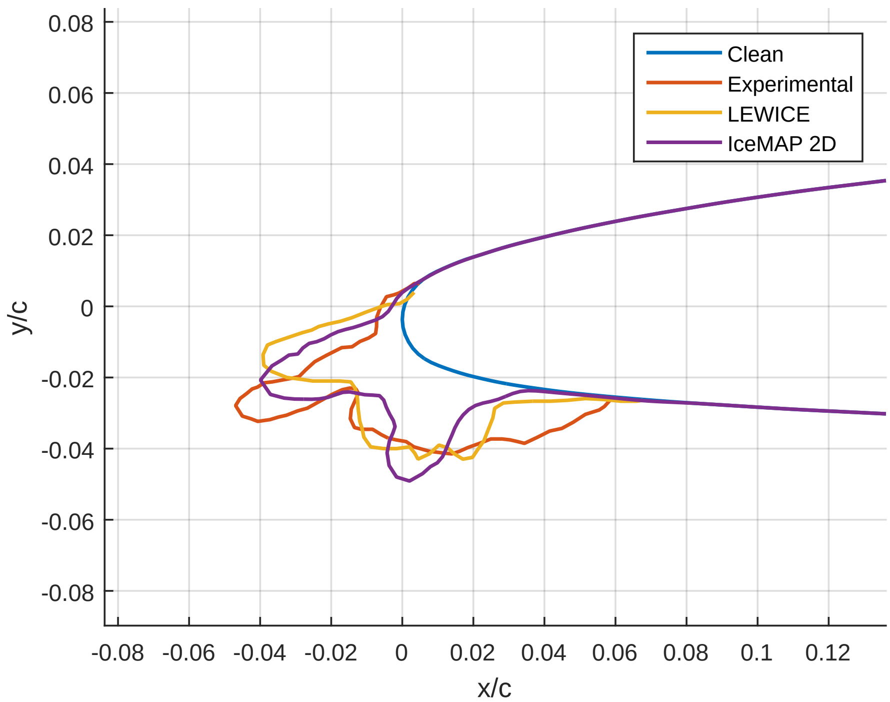

Figure 4.29: Run: 072703. GLC305, $V_\infty = 90\ m/s$, $T_\infty = 263.2\ K$, AOA = 6°, LWC = $0.6\ g/m^3$, MVD = $15\ \mu m$, t = $22.5\ min$.

The following ice shapes have been obtained for an AgustaWestland airfoil[3]. The results of IceMAP 2D has been compared with wind tunnel data for the following conditions:

	Run AW5
Airfoil	AW
chord $[m]$	-
Figure	4.30
AOA $[°]$	-2.5
$\mathbf{V}_\infty$ $[m/s]$	92.6
$\mathbf{T}_\infty$ $[K]$	270.15
LWC $[g/m^3]$	0.63
MVD $[\mu m]$	25
t $[min]$	15

In run AW5, figure 4.30, ice accretion on a production helicopter airfoil developed by AgustaWestland is simulated. The temperature is the highest among those tested, being equal to -3 $°C$, and total temperature is above freezing. As can be seen, the fact that the total temperature is above freezing is not sufficient to guarantee that no ice will grow. In this conditions water evaporation will cool the surface, eventually falling to zero and hence ice may accrete. A similar effect is simulated by IceMAP 2D, as ice grow over large areas of the airfoil, although the thickness is generally limited. A larger accretion is visible on the lower surface, which is simulated correctly by IceMAP 2D although in a slightly different position. Additional localized accretion are visible in the experimental ice shape on the upper surface, while the in the analytical shape the ice covers a larger area of the airfoil and only has a limited thickness. The difference may be explained by the simplification of the freezing model. Observations revealed that the flow of water over surface is largely impacted individual surface roughness element, such as those caused by freezing of small amount of water. In the model considered instead the surface roughness does not directly impact the film flow, but influences the heat transfer coefficient and consequently the rate of water freezing. As a result the ice forming is distributed over a wide surface area rather than concentrated in a small area where water initially froze. This effect though can not be easily modelled, as it would require a more microscopic modelling of the icing surface to take into account the individual roughness elements.

[3]The shape and chord of the airfoil are not reported because they are property of AgustaWestland and can not be disclosed.

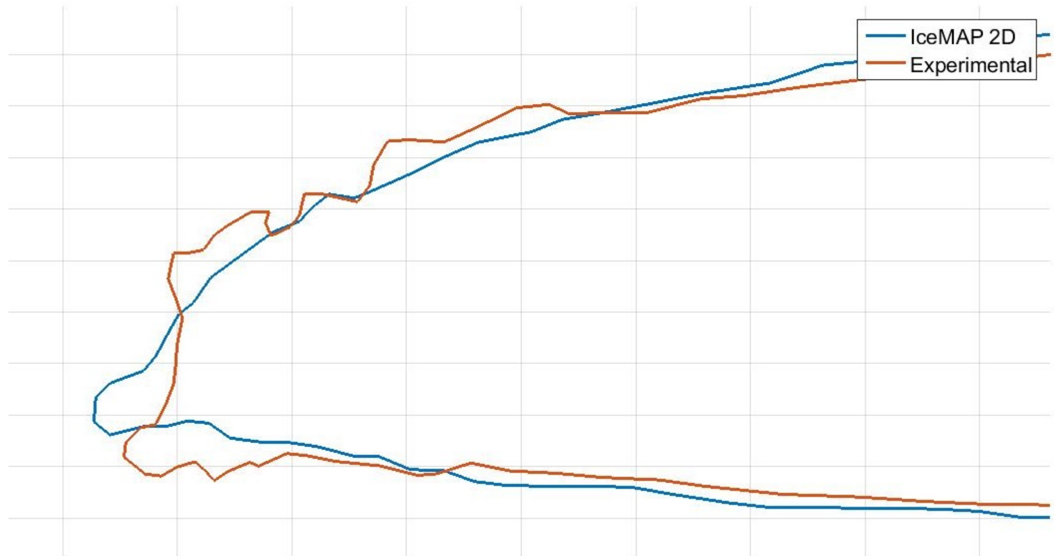

Figure 4.30: Run: AW5. AW airfoil, V_∞ = 92.6 m/s, T_∞ = 270.15 K, AOA = -2.5°, LWC = 0.63 g/m^3, MVD = 25 μm, t = 15 min.

Chapter 5

Computation of aerodynamic coefficients

IceMAP 2D also output the aerodynamic coefficients acting on the surface, which is a key performance indicator. As has been discussed, ice accretion leads to mass increase and performance degradation, which are usually measured using the coefficient of lift and drag. These are computed by default in IceMAP 2D for the final ice shape, but the user may also utilize Fluent to compute the coefficient at a different time step; this is done because of the different mesh is used to compute the aerodynamic coefficients and the ice accretion. The result obtained analytically in Fluent have been validated with experimental data[10] for iced airfoil from the Icing Research Tunnel. In the test cases conducted an iced NACA0012 airfoil with 0.53 m chord was used.

5.1 Rime conditions

The ice shape is first obtained for rime condition and at a fixed angle of attack. The coefficient of drag is then measured at different angles of attack and compared with experimental data, obtained following a similar procedure. The external conditions for rime ice growth are as follows:

- Velocity 58.06 m/s.
- Static temperature 248.8 K.
- Angle of attack 4°.
- Liquid water content 1 g/m^3.
- Droplet diameter 12 μm.
- Spray time 5 min.

The final ice shape, computed in IceMAP 2D and experimental, is visible in 5.1. In this case IceMAP 2D was used with a coarser time step compared to the value that would be obtained using the procedure indicated in section 4.1, thus the ice shape may be different using a smaller time step. Still, the differences with the experimental ice shape are not large, being limited to the area on top of the ice growth.

AOA °	cd IRT	cd Fluent
-3	0.01268	0.01211
0	0.01172	0.01006
4	0.01077	0.01075
8	0.01610	0.01540
11	0.03148	0.02201

Table 5.1: Coefficient of drag at different angles for rime ice shape.

When the ice shape has been obtained, the coefficient of drag of the airfoil is measured at different angle of attack, so that an indication of the variability of drag coefficients and the effects on the flow over the airfoil can be derived. Table 5.1 include the coefficient of drag measured at IRT and computed in Fluent

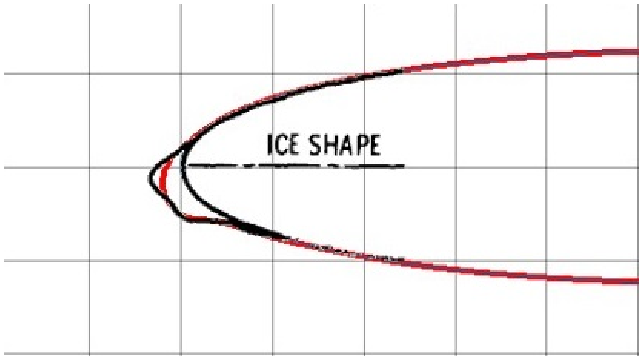

Figure 5.1: Final ice shape obtained for rime ice, Fluent and IRT.

The coefficient of drag for the iced and clean airfoil are also plotted in figure 5.2. The increase in drag is large for all conditions; for example, at zero angle of attack the drag raised to twice its corresponding clean value. Additionally, the increase can be extremely fast, as the ice formed in five minutes.

The coefficient of drag computed in Fluent is comparable with experimental data for small angle of attack, but it is smaller at higher angle. In the wind tunnel, for high angle of attack, flow separation was observed, which lead to a substantial increase in drag; on the contrary, in Fluent the flow remained attached at all conditions. This may be caused by the difference in the ice shape visible on the upper surface; indeed, the transition between the iced surface and the airfoil appears to be smoother than in the experimental conditions. This may have a large impact, especially at high angle of attack, because the flow separation is caused by the irregularities in the ice formation.

5.2 Glaze conditions

A second test has been conducted at higher temperature, resulting in a different type of ice forming. For glaze ice accretion the ambient conditions are:

- Velocity 58.06 m/s.

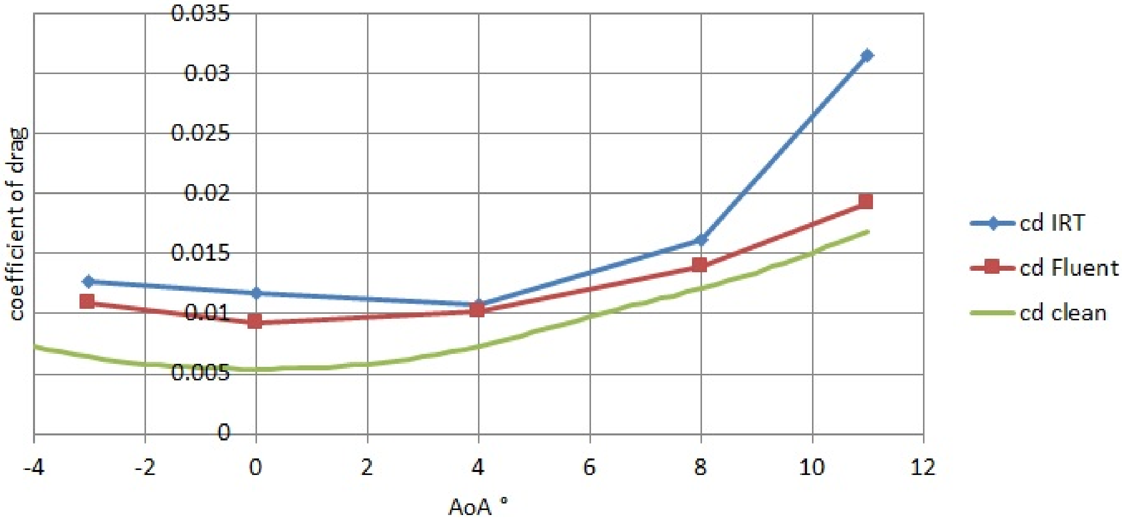

Figure 5.2: Plot of coefficient of drag vs AoA for rime ice, Fluent and IRT.

- Static temperature 266.8 K.
- Angle of attack 4°.
- Liquid water content 2.1 g/m^3.
- Droplet diameter 20 μm.
- Spray time 5 min.

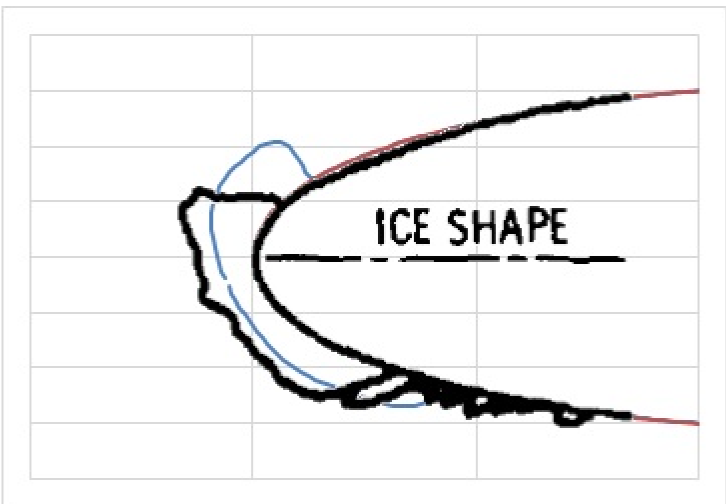

Figure 5.3: Ice shape obtained for glaze condition, IceMAP 2D and IRT.

Figure 5.3 shows the ice shape after the 5 minutes icing computed by IceMAP 2D and used to compute the aerodynamic coefficient along with experimental accretion. In this case the shape is different from the previous case, because runback water has created

AOA °	cd IRT	cd Fluent
-3	0.02683	0.01325
0	0.02199	0.01374
4	0.02767	0.02244
5.5	0.03580	0.03006
8	0.07647	0.06605

Table 5.2: Coefficient of drag at different angles for glaze ice shape.

additional localized ice thickness on the lower side of the airfoil. Additionally, the distribution of ice has created a less streamlined surface. Therefore, the increase in coefficient of drag is also subject to a large increase compared to a clean NACA 0012. This is shown in table 5.2, which contains the coefficient of drag measured at IRT and computed in Fluent, and in figure 5.4.

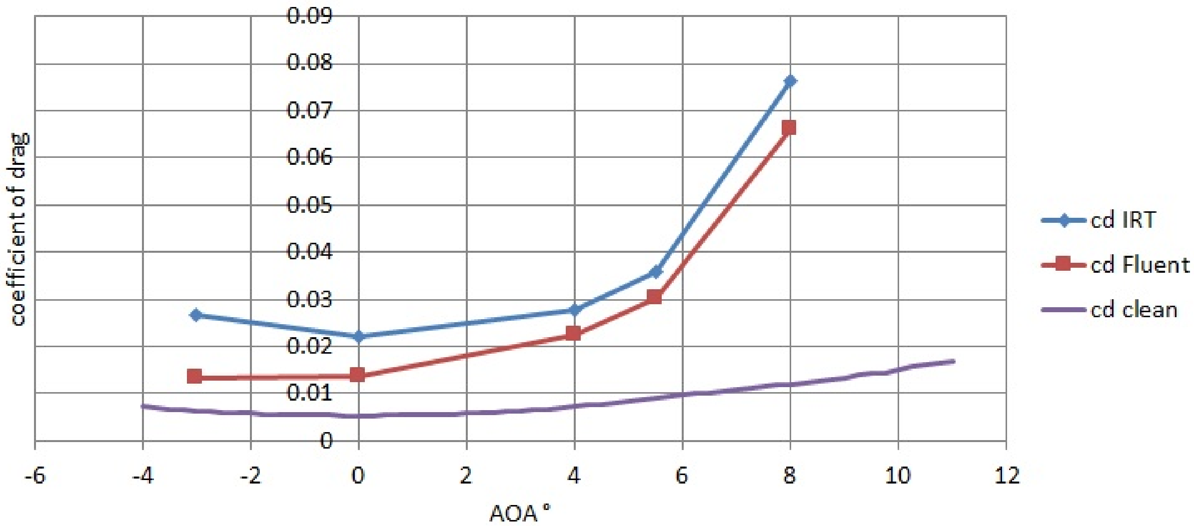

Figure 5.4: Plot of coefficient of drag vs AoA for glaze ice, Fluent and IRT.

Fluent under predicts the coefficient of drag at all angles; this can be explained by the difference in the ice shape, visible in figure 5.3, and by the smoother surface obtained in Fluent. This may be mitigated using a smaller mesh size, especially near the leading edge, so that even smaller feature typical of glaze ice can be modelled. Still, the results computed in Fluent are similar to the experimental value, and have general validity.

In this condition the coefficient of drag is more than doubled at zero angle of attack, and the difference becomes even larger at increasing angle of attack. Indeed, in the IRT tests the flow over the entire upper surface separated at an angle of attack as low as 6 degrees, while for the clean airfoil stall begins above 10 degrees. A similar condition is also apparent in Fluent, as the coefficient of drag has a similar trend. In figure 5.6 the velocity flow field over the upper surface of the airfoil, computed in Fluent, is visualized using vectors; the airfoil is set at 5.5 degrees, and the flow separation is already affecting a large portion of the airfoil. This has also effect on the numerical value of the coefficient of

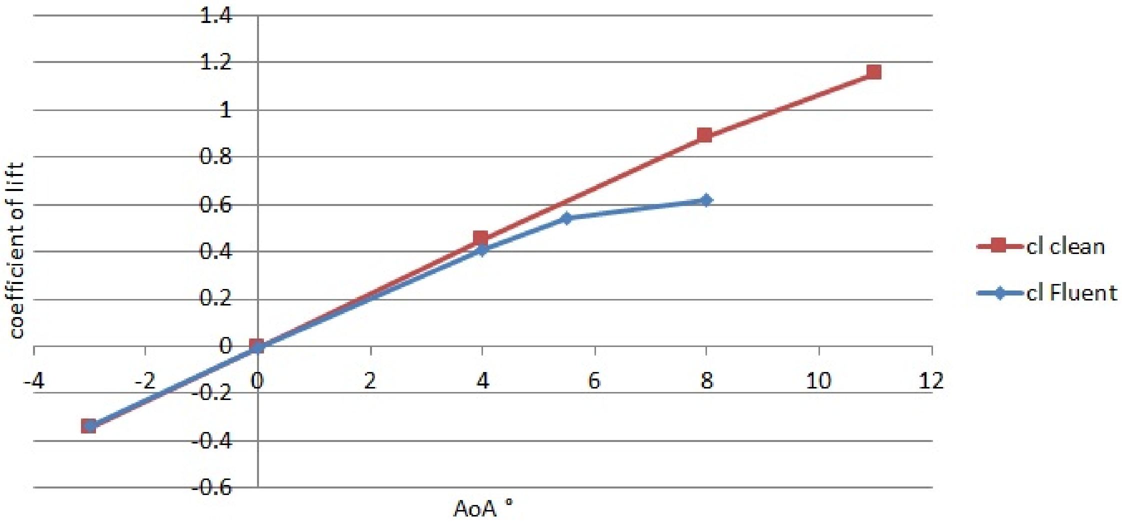

Figure 5.5: Coefficient of lift for a clean and iced NACA 0012 airfoil.

drag: at 5.5 degrees, for example, Fluent computes a value that is more than three times larger than the corresponding clean value and can be explained by the flow separation over the suction side.

Additionally, in Fluent also the coefficient of lift has been computed for the iced airfoil at different angle of attack. Also the lift characteristics of the airfoil are compromised by the ice accretion, as can be seen in figure 5.5, even at low angle of attack. This further highlight the issues outlined in the introduction, 1, and caused by the rapid accretion of ice on lifting surfaces. In this glaze condition, the drag more than doubled at all angle of attack, while at the same time the lifting characteristics worsened. For icing on helicopter blade this problem would be further exacerbated by the variations in the angle of attack to which the blade is subject; indeed, for the advancing blade the angle of attack may reach 10 degrees, which will result in the premature stall of the airfoil.

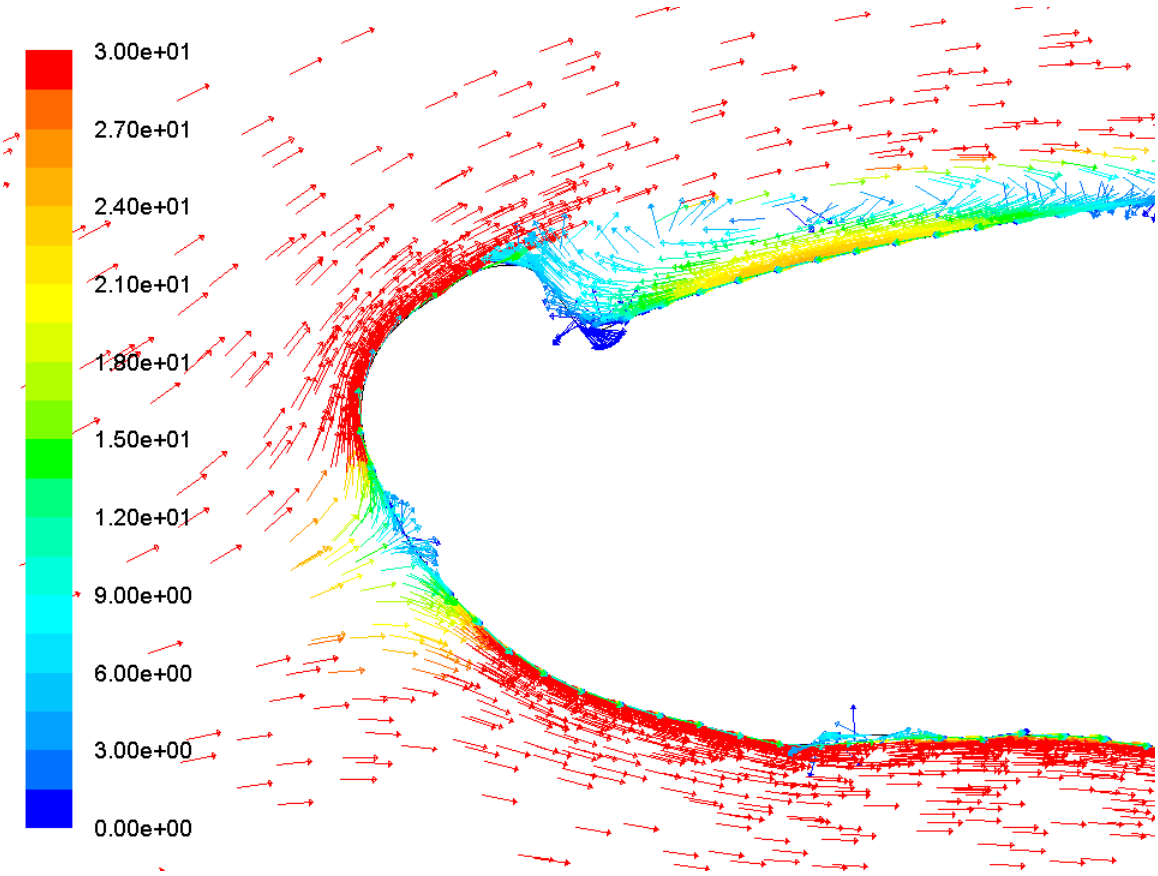

Figure 5.6: Vectors of velocity on the upper surface of the iced airfoil. Recirculation of flow over a large area at 5.5 degrees on a glaze ice accretion.

Chapter 6

Conclusions

A tool, IceMAP 2D, to simulate ice accretion has been successfully developed and integrated in ANSYS Workbench; also the ice accretion module has been completely developed and is embedded in Fluent. A minimal number of inputs are required to perform the simulation while the rest of the process is automatically executed. The final output includes the iced geometry and the aerodynamic coefficients for the iced airfoil.

IceMAP 2D has proved to be capable of simulating ice accretion for a wide variety of icing conditions of interest. The tool has not been subject to failures and computation time have been limited to less than 10 minutes per time step on a laptop. Therefore, a sensible number of icing conditions have been tested to verify the accuracy of the simulation, including particularly demanding conditions, like long accretion time, high angle of attack and high temperature. The ice shapes obtained are overall comparable, not only for rime conditions but also in glaze conditions. Specifically, maximum thickness, presence of horns and their direction are computed correctly in the cases tested. The usage of a CFD software to simulate the flow field and the icing model employed has thus resulted in a good agreement with experimental ice shapes.

A somewhat larger variability has been observed in the computation of the aerodynamic coefficients, which is generally limited at high angles of attack. Because in this conditions flow separation is a significant part of the drag increase, small differences in the computed ice shape can lead to large variations in the aerodynamic coefficients. The number of test cases for which the coefficient of drag is available is limited, and therefore also the coefficient of drag have been compared only in some cases. Additional tests, along with a refinement of the mesh could help better understand if the differences observed are caused by difference in ice shape.

Chapter 7

Future development

Although IceMAP 2D has been successfully used to simulate ice accretion, a number of improvements could be done, to either improve the results or include additional features.

As has been observed in the mesh chapter, 3.2.1, the mesh size has an influence on the computed ice accretion; indeed, using a mesh too coarse will result in the elimination of ice feature, while using a mesh too fine will result in numerical difficulties. Therefore, a complete study of the variability of ice shape with respect to mesh size should be conducted, in order to provide better guidance in the choice of the mesh size.

An additional factor that affects the ice growth is the surface roughness and consequently the heat transfer coefficient; in the model considered a single value of surface roughness was employed, but it does not represents the actual local roughness. In Fluent it is possible to define a variable surface roughness for the surface of interest, and this feature may be used to impose a local value of roughness computed using the icing condition at a given surface location. The use of a different turbulence model to compute the heat transfer coefficient and to obtain the flow solution leads in an increase in the overall computational time; using a $k\omega - SST$ turbulence model for all the simulation will cut the computation time, but testing is required to ensure that the heat transfer coefficient is still accurate. The variability observed in 3.3 may be eliminated by a proper modification of the turbulence model parameters available in Fluent. This, though, should not result in the worsening of the boundary layer solution.

In glaze condition the water film has a significant impact on the ice shape, as it result in large localized accretion (horns). The flow of the film is mainly governed by air shear, which in the current model is not considered. The inclusion may improve the ice shape when the presence of horns is particularly large, as in this case the simple flow model used may not provide an accurate modelling.

The inclusion of a more complex fluid flow model is also required in a three dimensional extension of IceMAP 2D; in this conditions additional forces, like centrifugal forces for rotor blades, acting on the water film must be considered because they significantly impact the flow direction and consequently the freezing location of runback water. If these forces are neglected the capability of simulating ice accretion on more complex geometries would be severely impeded. Fluent, in this respect, offer great flexibility, as also rotating object can be properly simulated, thus the ice accretion module would not require substantial work. Additionally, the forces acting on the water film can be computed directly by Fluent in the solution process, thus ensuring that the modelling of forces, mass and energy fluxes is as accurate as possible.

An additional feature that may be implemented is the simulation of anti icing systems. This should provide the capability to ensure that the anti icing system installed or designed is capable of maintaining the surface clean from ice. The system provides a heat flux to the surface, which must be accounted for in the thermodynamic balance. The solution yields the freezing and the surface temperature, which are the required parameters to ensure that the surface remains clean from ice.

Finally, the model may be extended to larger size (SLD) by considering the effects of particle deformation, breakup and splashing which are significant in this range of size; this would result in a more realistic collection efficiency and impinging mass on the airfoil. Therefore, the smaller droplets resulting from breakup or splashing are simulated, thus considering that they may flow past the surface or impact on the surface at a different location.

Appendix A

IceMAP 2D structure

A.1 List of input

It is first required to define the name of the folder where the file generated in the solution process, by ANSYS Workbench and IceMAP 2D, are saved. The inputs required by IceMAP 2D for the icing simulation can be broadly divided in external condition (icing and freestream), geometry characteristic, mesh characteristic and mesh quality controls.

Ambient conditions required are:

- Freestream velocity.
- Freestream static temperature.
- Freestream static pressure.
- Angle of attack.
- Liquid water content.
- Mean volumetric diameter.
- Number of time steps.
- Accretion time per time step.
- x-position of water injection in the domain for the particle tracking module m. Y-coordinates are estimated using geometric information of the airfoil size and angle of attack.

Geometric informations required are:

- Chord length.
- Thickness to chord ratio. This is to be set only if the airfoil is NACA 4 digit symmetric airfoil, as in this case the airfoil coordinate file is automatically generated. For other airfoil this parameter is not required, as the the geometry is defined by an external file.

- Path to the file with body coordinates. If the thickness to chord ratio is not set then the path of the file with the airfoil coordinates must be provided; the coordinates must be dimensional. The file should be composed of 5 columns, containing respectively group index (equal for all the points), point index, x coordinate, y coordinate and z coordinate (that should be set to 0).

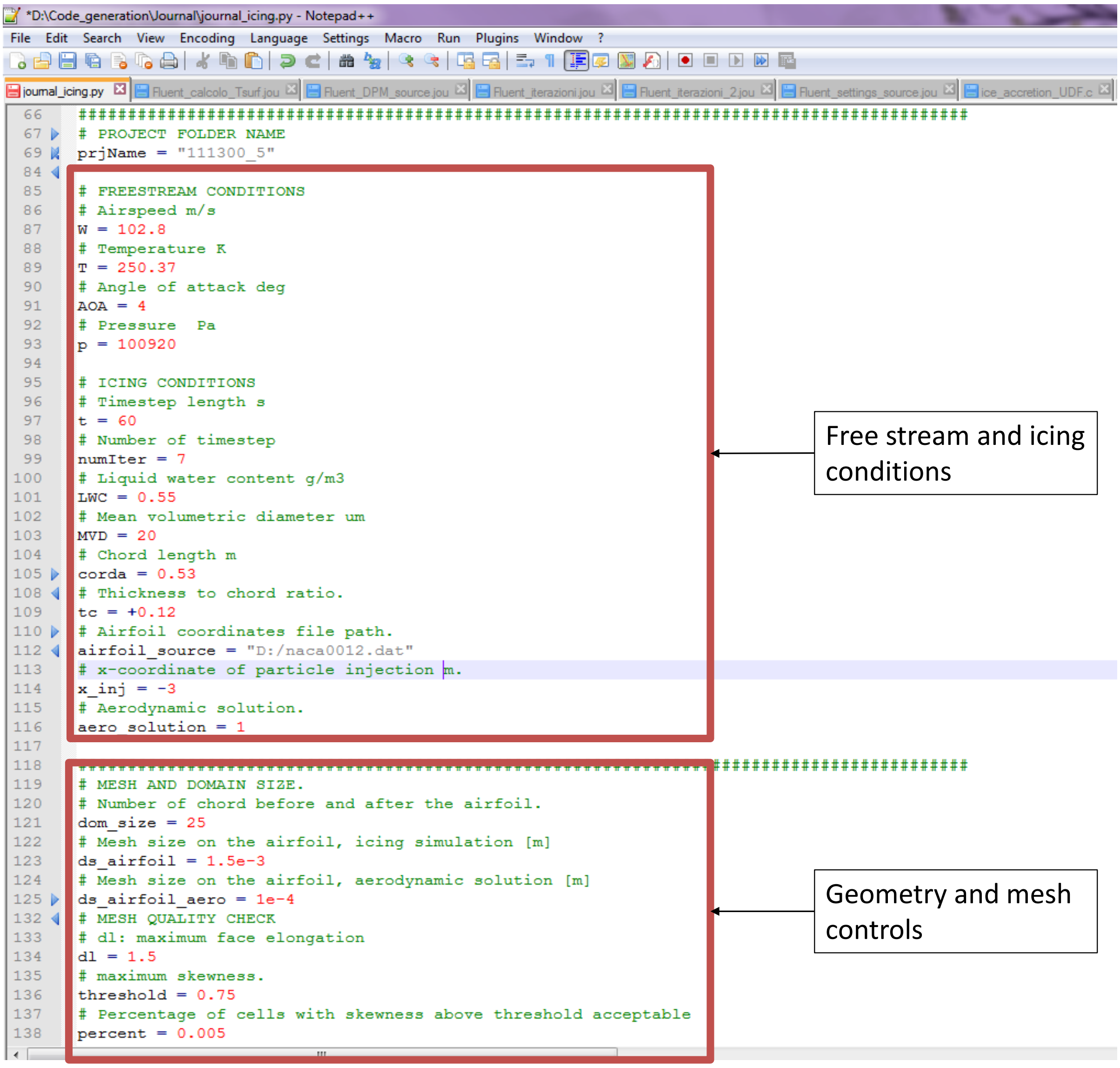

Figure A.1: User inputs required.

Mesh characteristic required are:

- Domain size in number of chord before and after the leading edge of the airfoil.
- Mesh size for the airfoil.
- Mesh size for the airfoil, for the final computation of aerodynamic coefficients.

Finally the controls used to check the mesh quality after each time step must be specified:

- Maximum acceptable elongation of segments on the airfoil.
- Threshold skewness.
- Maximum percentage of cell with skewness above the threshold value acceptable.

These parameters are set directly in the script, as shown in figure A.1.

A.2 Solution steps

IceMAP 2D is written in Python and is executed as a script file in ANSYS Workbench. IceMAP 2D is responsible for the modification of the script and journal files necessary according to the input supplied, the creation of the blocks in project schematic, launching the various application in a specified order and issuing commands through the scripts and journal, and checking the mesh quality.

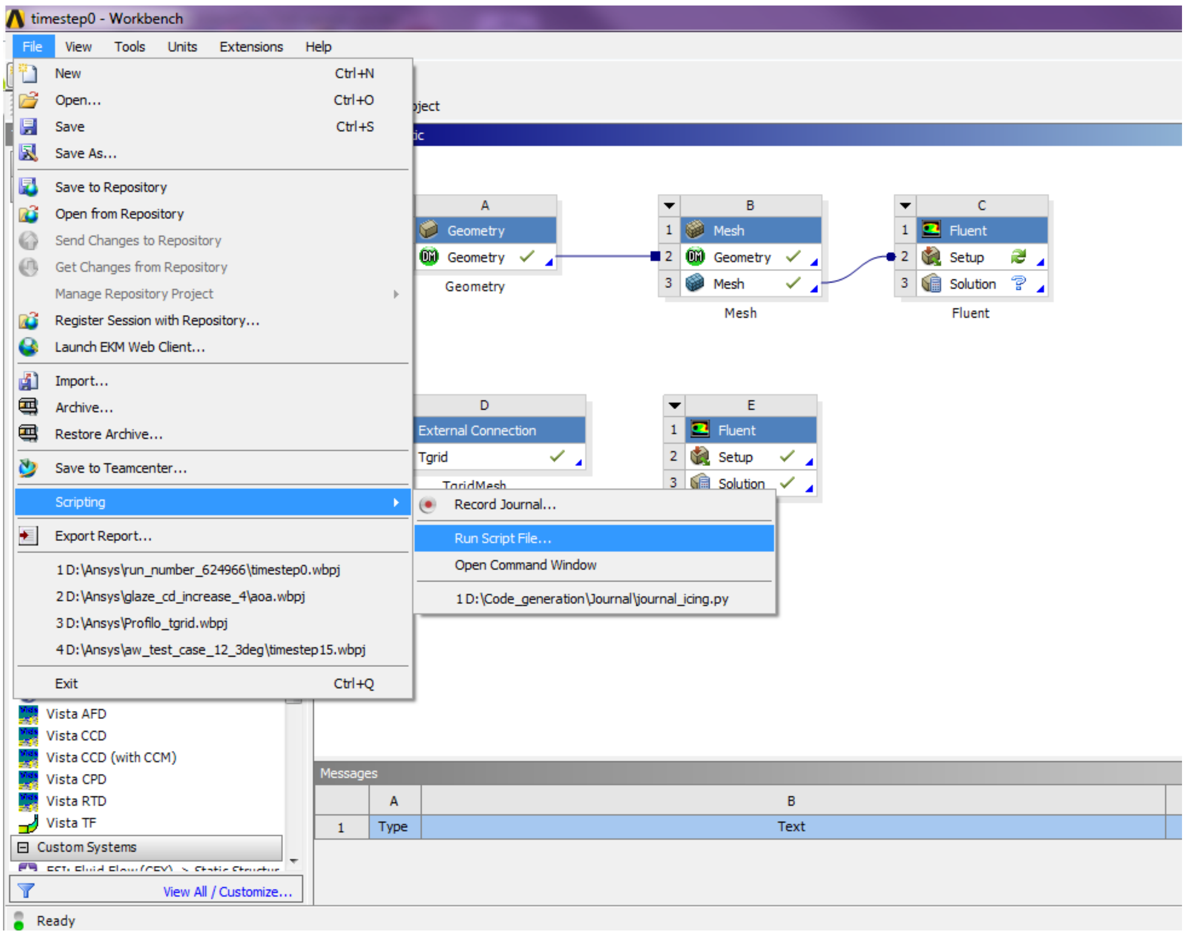

Figure A.2: Launching of the script in ANSYS Workbench. Also visible below the blocks that will be created.

In the script and journal additional controls on the solution process may be accessed if the predefined values do not provide satisfactory results. The scripts required for the creation of the mesh on the computational domain are:

- "script_geometry.js": generates the computational domain in ANSYS DesignModeler, using the supplied airfoil geometry and domain size.
- "script_mesh.js": generates, in ANSYS Meshing, the boundary discretization on the airfoil and on the far field used for the ice accretion simulation. The size of the mesh is defined in the input parameters.
- "script_mesh_aero.js": generates, in ANSYS Meshing, the boundary discretization on the airfoil and on the far field used for the computation of the aerodynamic characteristics. The size of the mesh is defined in the input parameters.
- "tgrid_journal.jou": generates the volumetric mesh of the domain in Tgrid, using the boundary discretization supplied by ANSYS Meshing.

Tgrid is integrated in ANSYS Workbench using a configuration file, "tgrid.xml", which defines the properties of the block appearing in the project schematic. When the block is updated a script, "tgrid.py", is executed and launches Tgrid; finally in Tgrid the journal "tgrid_journal.jou" is executed.

The generated mesh is then imported in Fluent, where a number of journals are used in the process. These are:

- "Fluent_settings.jou": contains the settings required for the fluid flow simulation, including the free stream conditions supplied and the surface roughness, which is automatically computed in IceMAP 2D.
- "Fluent_compute_Tsurf.jou": the journal is used to compute the surface temperature on the airfoil before the first time step. It output a file with the temperature distribution over the airfoil, which is then read in Fluent and used for the actual icing simulation.
- "Fluent_iterations.jou": contains the instruction required to compute the heat transfer coefficient at every time step. Therefore the appropriate turbulence model and surface temperature is set before saving the heat transfer coefficient values at each surface location.
- "Fluent_iterations2.jou": solves the fluid flow with the $k\omega - SST$ turbulence model to compute the forces acting on liquid droplets and the flow variables on the surface.
- "Fluent_DPM.jou": contains the instructions required to launch the particle tracking, the ice accretion module and the update of the geometry.
- "Fluent_aero_coefficients.jou": solution of the fluid flow for the computation of the aerodynamic coefficients.

The user defined functions required in the ice accretion process are written in a C file, "ice_accretion_UDF.c", which is also supplied to Fluent and is responsible of:

- Initializing variables required in the simulation.
- Initializing particle position as defined in the inputs.
- Store particle data at impact, that is temperature and velocity of particles at impact and mass flow rate.
- Compute collection efficiency.
- Compute the energy and mass terms necessaries and solve the thermodynamic balance, in order to compute at each surface location the freezing fraction, icing mass, ice thickness and temperature on the iced surface.
- Compute the position of the iced surface.
- Write in external file the variables of interest.

The previous files are saved in the folder for the project, so that they may be used in case the user decides to continue a simulation manually. In this case the user is only required to launch in the proper order the scripts already present. Beside launching the previous files IceMAP 2D also control the quality of the mesh at each time step to decide whether the domain should be remeshed, and renames the output file of the user defined functions for later use.

A.3 List of output

At the end of each time step seven files are written, containing information from the thermodynamic balance and the iced geometry. These are:

- "b_data.txt"
- "m_data.txt"
- "q_data.txt"
- "t_data.txt"
- "D_mesh.txt"
- "face_pos.txt"
- "flow_data.dat"

IceMAP 2D also add an index representing the time step for which the file were written, thus for example "m_data2.txt" contains informations calculated at the second time step. In the files the information for each segment of the airfoil are listed. The face can be identified by a unique index, written in all of the file, beginning at stagnation point and increasing clockwise. Coupled with the face length, which is also output, can be used to define a curvilinear coordinates system on the airfoil

"b_data.txt" contains generic information on the ice accretion:

- Face index.
- Collection efficiency.
- Freezing fraction.
- Ice thickness.
- Number of particle impacts.
- Face length.

"m_data.txt" stores the mass fluxes terms computed for the mass balance:

- Face index.
- Mass flux of impinging water.
- Runback water entering the face.
- Mass flux of evaporating water.
- Mass flux of sublimating water.
- Mass flux of water freezing.
- Freezing fraction.
- Face length.

"q_data.txt" stores the energy fluxes terms computed for the energy balance:

- Face index.
- Energy flux due to convection.
- Energy flux due to aerodynamic heating.
- Energy flux due to evaporation.
- Energy flux due to sublimation.
- Energy flux due to the impact of particles.
- Energy flux due to internal energy of impinging water.
- Energy flux due to ruback water entering the face.
- Heat transfer coefficient.
- Freezing fraction.
- Face length.

"t_data.txt" stores informations on the surface temperature:

- Face index.
- Surface temperature before ice accretion.
- Air temperature on the surface.
- Temperature on the ice accretion.
- Face length.

"D_mesh.txt" stores informations on the nodes positions, used in the mesh modification in Fluent:

- Face index.
- x-coordinate of node after ice accretion.
- y-coordinate of node after ice accretion.

"face_pos.txt" stores informations on position of the face centroid, used to output a coordinate file of the geometry:

- Face index.
- x-coordinate of face centroid before ice accretion.
- y-coordinate of face centroid before ice accretion.
- x-coordinate of face after ice accretion.
- y-coordinate of face after ice accretion.
- Face length.

"flow_data.dat" stores informations on the calculated conditions at the edge of the boundary layer:

- Face index.
- Temperature at the edge of the boundary layer.
- Pressure at the edge of the boundary layer.
- Mach at the edge of the boundary layer.
- Velocity at the edge of the boundary layer.
- Face length.

When the aerodynamic coefficients on the iced airfoil have been computed an additional file is written, "Forces.dat", which contains the axial and normal forces computed in Fluent for the airfoil as well as the axial and normal coefficients. These are computed considering a chord length of 1 m, thus must be divided by the chord length before being used. Additionally, the computed forces and coefficients are divided in the contribute due to pressure and viscosity.

A.4 Postprocessing

A MATLAB script can also be used to visualize the information provided in the output files. The script require the path of the folder where the output files are located and the number of time steps that should be imported. Each column of the file is then plotted in a MATLAB figure. The abscissa of the figures is the adimensional surface length, starting from stagnation; surface length is considered positive on the upper airfoil surface, while is considered negative on the lower surface. The ice shape at different time steps is instead plotted in dimensional coordinates, as in figure A.3

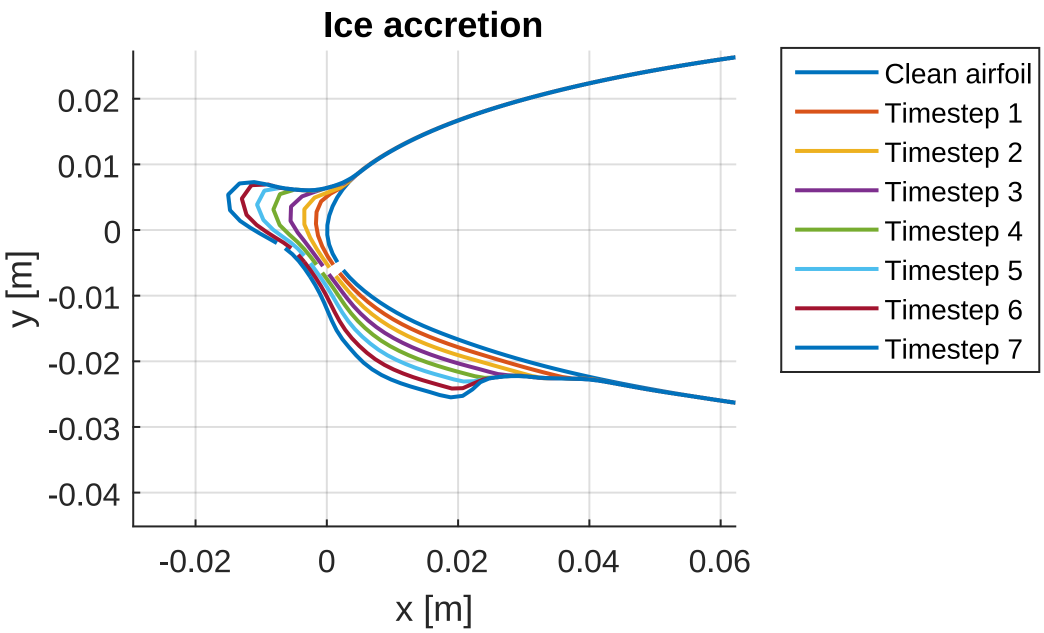

Figure A.3: Ice shape at different time steps for run 5528. Total accretion time 7 minutes, time step of 1 minutes.

The variables are labelled in order to indicate the time step at which they were computed. The mass (figure A.4) and energy (figure A.5) fluxes are adimensionalized with respect to the local surface area, so that the local size of the element does not influence the result; therefore the fluxes computed with different meshes may be compared directly without further computation.

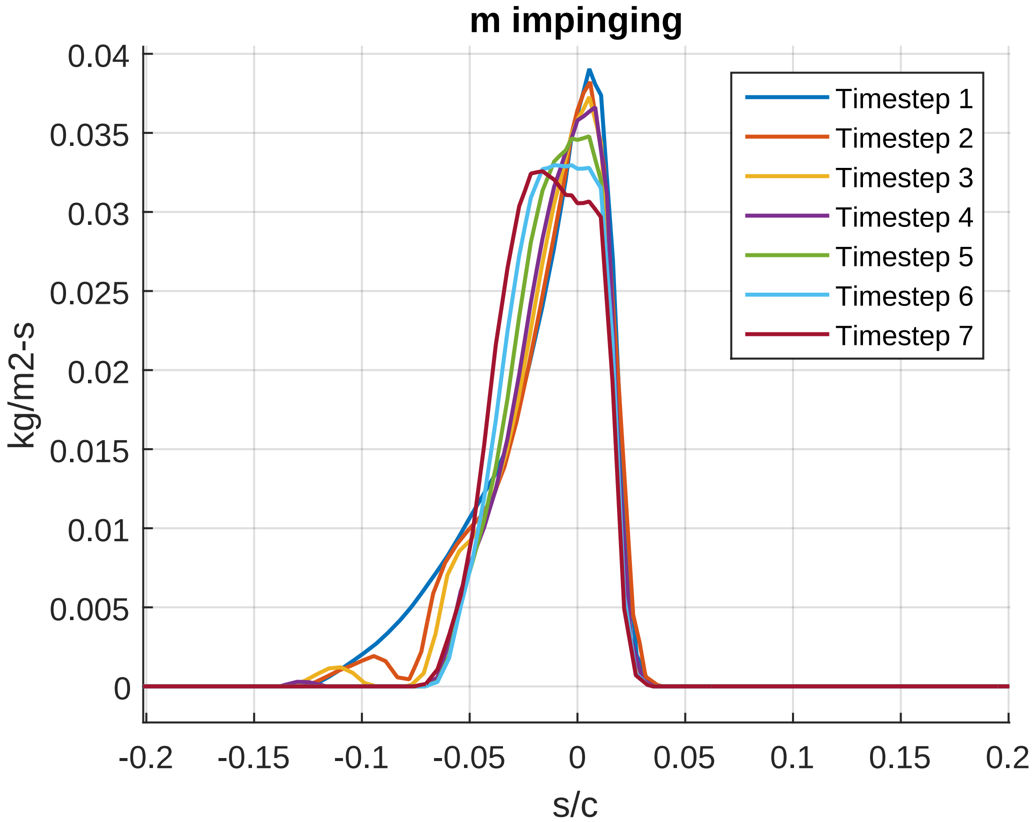

Figure A.4: Impinging mass flux at different time steps for run 5528. Total accretion time 7 minutes, time step of 1 minutes.

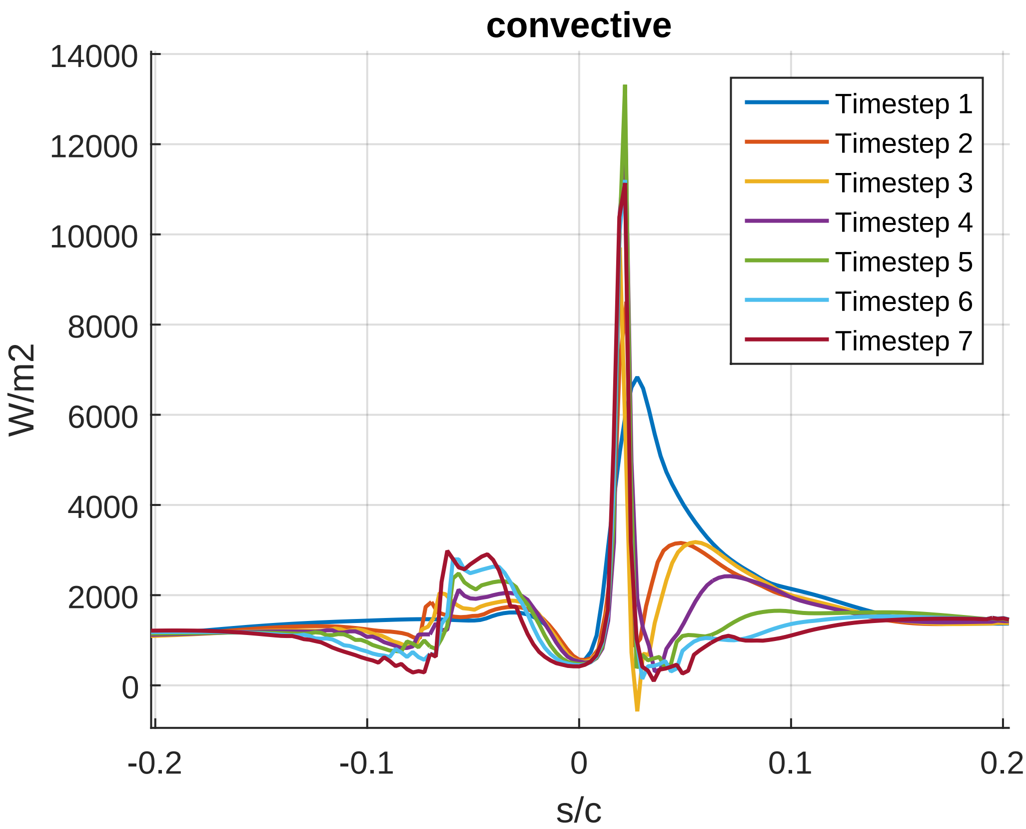

Figure A.5: Convective heat flux at different time steps for run 5528. Total accretion time 7 minutes, time step of 1 minutes.

Bibliography

[1] JT Cansdale and RW Gent. Ice accretion on aerofoils in two-dimensional compressible flow-a theoretical model. *Royal Aircraft Establishment Technical Report*, 82128, 1983.

[2] HW Coleman, BK Hodge, and RP Taylor. A re-evaluation of schlichting's surface roughness experiment. *Journal of Fluids Engineering*, 106(1):60–65, 1984.

[3] Ansys Fluent. 16.0 udf manual. *Ansys Inc*, 2015.

[4] RW Gent. Trajice 2, a combined water droplet and ice accretion prediction program for aerofoil, royal aerospace establishment(rae) technical rept. tr 90054, farnborough, hampshire, nov. 1990.

[5] Irving Langmuir, Katherine Blodgett, et al. Mathematical investigation of water droplet trajectories. 1946.

[6] L Makkonen. Heat transfer and icing on a roughened cylinder. Technical report, National Research Council of Canada,, 1984.

[7] Bernard L Messinger. Equilibrium temperature of an unheated icing surface as a function of air speed. *Journal of the Aeronautical Sciences (Institute of the Aeronautical Sciences)*, 20(1), 2012.

[8] SA Morsi and AJ Alexander. An investigation of particle trajectories in two-phase flow systems. *Journal of Fluid Mechanics*, 55(02):193–208, 1972.

[9] Tim G Myers and Chris P Thompson. Modeling the flow of water on aircraft in icing conditions. *AIAA journal*, 36(6):1010–1013, 1998.

[10] William Olsen, Robert Shaw, and James Newton. *Ice shapes and the resulting drag increase for a NACA 0012 airfoil.* National Aeronautics and Space Administration, 1984.

[11] Michael Papadakis, See-Cheuk Wong, Arief Rachman, Kuohsing E Hung, Giao T Vu, and Colin S Bidwell. Large and small droplet impingement data on airfoils and two simulated ice shapes. *__, Oct*, 2007.

[12] Philip E Poinsatte. *Heat transfer measurements from a NACA 0012 airfoil in flight and in the NASA Lewis Icing Research Tunnel*, volume 4278. National Aeronautics and Space Administration, Office of Management, Scientific and Technical Information Division, 1990.

[13] WE Ranz and WR Marshall. Evaporation from drops. *Chem. Eng. Prog*, 48(3):141–146, 1952.

[14] Gary A Ruff and Brian M Berkowitz. Users manual for the nasa lewis ice accretion prediction code (lewice). 1990.

[15] Hermann Schlichting. Experimental investigation of the problem of surface roughness. 1937.

[16] J Shin, B Berkowitz, H Chen, and T Cebeci. Prediction of ice shapes and their effect on airfoil performance. *NASA Technical Memorandum*, 103701, 1991.

[17] Jaiwon Shin and Thomas H Bond. *Experimental and computational ice shapes and resulting drag increase for a NACA 0012 airfoil.* National Aeronautics and Space Administration, 1992.

[18] William B Wright. *User Manual for the NASA Glenn Ice Accretion Code LEWICE.* National Aeronautics and Space Administration, Glenn Research Center, 2002.

[19] William B Wright, RW Gent, and Didier Guffond. Dra/nasa/onera collaboration on icing research, part 2. Technical report, 1997.

[20] William B Wright and Adam Rutkowski. *Validation results for LEWICE 2.0*, volume 208690. National Aeronautics and Space Administration, Lewis Research Center, 1999.